Multi-Band Bandpass Filters and Filtering Power Dividers Based on Dual-Mode Resonators

（デュアルモード共振器を用いたマルチバンド帯域通過フィルタ
とフィルタリングパワーディバイダに関する研究）

文 品

埼玉大学大学院理工学研究科（博士後期課程）

理工学専攻（主指導教員　馬　哲旺）

Saitama University
埼玉大学

2019 年 9 月

This dissertation is dedicated

TO MY PARENTS AND MY SUPERVISOR

**For their inspirations and encouragements
that make this dissertation a reality!**

Abstract

Multi-band microwave components are expected to be used in modern high-integration wireless communication systems, which can support multi-services simultaneously without adding additional receive or transmit links. For this reason, multi-band microwave components are attracting great attention and becoming research hotspot in microwave passive components domain. Particularly, in the development of multi-band bandpass filters (BPFs) and filtering power dividers (FPDs), how to realize high selectivity, small circuit size, low loss, wide stopband, and flexible control of the channel frequencies and bandwidths are challenging problems. Moreover, balanced-to-unbalanced (BTU) filtering power divider is also one of the key passive components in RF/microwave front-ends for connecting the balanced ports and single-ended port to achieve conversion between balanced and unbalanced signals with common-mode noise suppression. This dissertation is intended to propose new types of multi-mode resonators (MMRs) and develop dual-band and tri-band BPFs, dual-band FPDs, and BTU filtering power dividers with small circuit size, independent control of channel frequencies and bandwidths, and other excellent frequency characteristics.

Firstly, a novel type of stub-loaded stepped-impedance resonator (SL-SIR) is proposed. With different schematics of the loaded stubs, the SL-SIR has flexibly controllable dual-modes or tri-modes to construct dual-band or tri-band BPFs. Detailed mode analysis of the resonator is conducted, and parametric variations of the modes are investigated. Next, dual-band and tri-band BPFs are proposed and designed using the dual-mode or tri-mode SL-SIRs. Multiple geometrical parameters in both the external feeding structure and the internal couplings between neighboring resonators are employed to make the individual control of the two or three passbands possible. Furthermore, separately changeable multiple coupling paths between the resonators and the coupling paths between the source and load are devised to create multiple transmission zeros, which not only enhance significantly the selectivity of the passbands, but also widen greatly the stopband of the BPFs. A small H-shaped composite resonator is also proposed, and its even-mode and odd-mode are used to configure a miniaturized dual-band BPF

with a flexible center frequency ratio. Three transmission zeros are produced by introducing a mixed electric and magnetic coupling between the resonators, which improves significantly the selectivity and out-band rejection performance. All the designed dual-band and tri-band BPFs are fabricated, and their measured frequency responses agree well with the theoretically predicted ones.

Secondly, a novel compact dual-band filtering power divider (DB-FPD) is developed which can reduce significantly the circuit size of a RF/microwave front-end. The proposed DB-FPD consists of a small U-shaped Wilkinson power divider, two pairs of dual-resonance resonators (DRRs), and a pair of spur-lines. With the simultaneous use and appropriate design of the coupled feedlines, mixed electric and magnetic couplings between the DRRs, and spur-lines with different lengths, multiple TZs are produced which result in two passbands with desired power division, high frequency selectivity, good isolation, and an ultrawide stopband. A prototype DB-FPD is designed, fabricated and measured. The measured responses agree well with the design simulations, exhibiting a stopband up to 13.8 GHz ($6f_0$) with 20-dB rejection level. This is the widest stopband of DB-FPDs reported thus far.

Finally, two novel balanced to unbalanced filtering power dividers with variable bandwidth are proposed based on stub-loaded dual-mode resonators (SL-DMRs). Two SL-DMRs are used to replace the 90° horizontal transmission lines to realize filtering responses. With the even- and odd-mode analysis method and traditional transmission line theory, closed-form analytical equations and detail design procedures are derived. Moreover, a pair of parallel coupled-lines are used to feed the SL-DMRs, which not only realize variable bandwidth but also improve the stopband performance. Three transmission zeros (TZs) locate on both sides of the passband, which improve the selectivity of the passband. To verify the analytical theory and design method prediction, two prototypes are designed, fabricated, and measured. The measured responses agree well with the design simulations, exhibiting a good frequency selectivity, isolation, and common-mode suppression.

Acknowledgements

I owe my greatest gratitude to my supervisor Professor Zhewang Ma for allowing me to conduct this research on multi-band BPFs and filtering power dividers under his supervision. Professor Zhewang Ma always gives me patient guidance, persistent encouragement, and valuable advices throughout my study, despite his busy agenda. His extraordinary research motivation and technical insight have a crucial impact on my research career. Moreover, his effective work and rigorous academic attitude have established a role model for me. At the same time, I also would like to express my warm gratitude to my vice-supervisors, Dr. Masataka Ohira and Dr. Yuichi Kimura, for their invaluable lectures and kind advices for my research.

I sincerely thank Professor Haiwen Liu, who gave me the support of international conference fee and the platform of circuit measurement, and thank Professor Xuehui Guan, Professor Xiaolong Wang, and Dr. Baoping Ren, for their concerns, encouragement, and helpful discussions on my research.

Special acknowledgements go to Mr. An Song, Ms. Tianyu You, Mr, Fan Liu, Mr. Yi Song, Mr, Yifan Wang, Mr. Hao Xu, Mr. Zhengbiao Wang, Mr. Cheng Han, and Mr. Hongfeng Yu, and all the people in my life for their kind help and great encouragement.

Finally, I deeply recognize that without the supports of all members of my family, I would never find the courage to overcome all of the difficulties encountered during my study career, and I would never have completed this dissertation. My thanks go to my parents and my girlfriend for their unconditional love and support. I also want to say thank you to my brother and his family for their happiness.

Table of Contents

Chapter 1

Introduction

1.1 Motivation and Objectives

Filters and power dividers are plays important roles in many modern RF/microwave wireless communication systems. With the rapid development of electronic and information technologies, wireless communications are facing huge challenges, ilke higher integration, higher performance, small size, lighter weight, and lower cost. Multifunction and small size are most important targets for small intelligent terminals to realize low power consumption, portable, and multi-services.

Among them, multi-band microwave components are widely used in modern high-integration wireless communication systems, which can support multi-services simultaneously without adding additional receive or transmit links. In Fig. 1-1(a), multiple receive links are in parallel to meet the multi-service requirement of the modern wireless communications. Obviously, this approach will bring more insertion loss, large circuit size and high system cost. In Fig. 1-1(b), more efficient approach is proposed based on dual-/multi-band components with compact size and low loss. Therefore, dual-band or multi-band microwave components have been attracting great attentions and becoming research hotspot at microwave passive components domain. How to realize high-
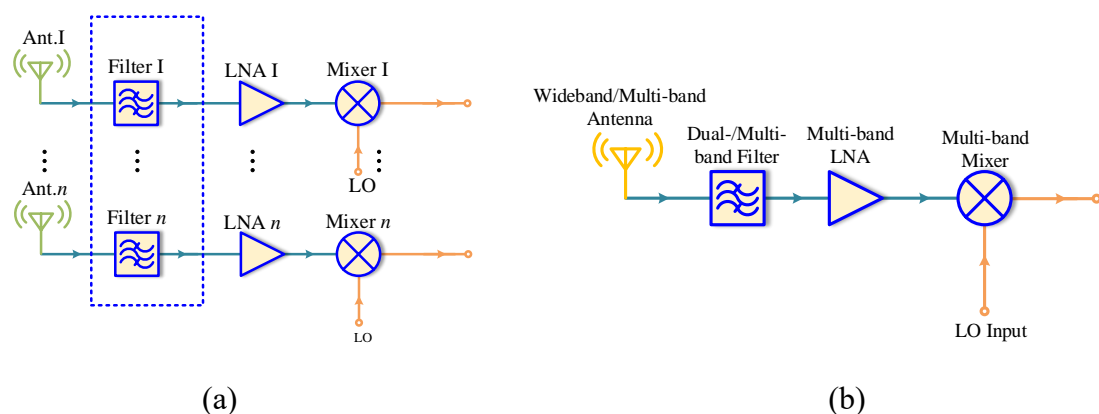
Fig. 1-1: The block of RF front-end systems. (a) Combining multiple single-band receive

links. (b) Dual-/multi-band receive front-end.

selectivity, small circuit size, low-loss, wide stopband, and controllability of frequencies and bandwidths are the difficult problems in current research.

Moreover, within the RF/microwave community, power dividers also have served a prominent role for years. The main function of a power divider is to split a given input signal into two or more signals as needed by the circuit. In receive system, a typical application for a power divider is to split a signal to feed multiple low noise amplifiers, and then have the signals from the amplifiers recombine into a high power output signal. With the developing of phase array Rx/Tx systems, power dividers plays important role. In this system a signal is either fed through an equal split power divider featuring a specific number of output ports, or a series of equal split power dividers. The split signals are then fed through phase shifters and then to an array of transmitting antennas. The phase difference between each signal being transmitted allows for electronic beam scanning, allowing the transmitted beam to be focused in different directions depending upon the phase difference, as shown in Fig. 1-2.
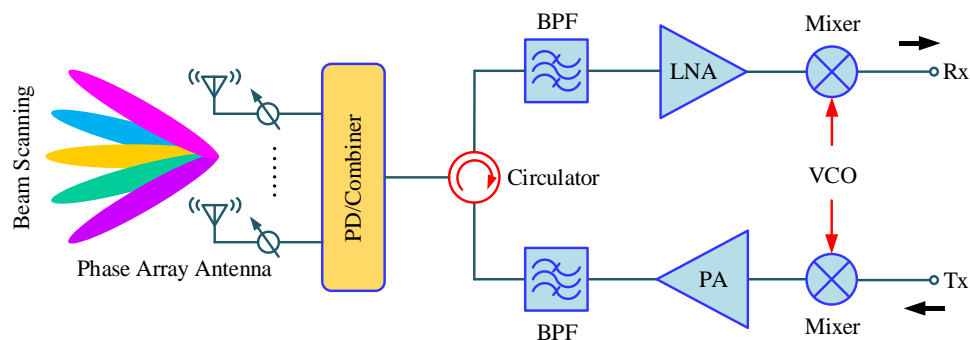
Fig. 1-2: The typical phased array transceiver architecture.

Recently, for further improving the integration of system, composite function components are attracted great attentions, such as filtering antennas [1–3], filtering baluns [4–5], filtering power dividers [6–10], and so on. Although, many previous works are reported about filtering power dividers, there are still many works worth to do, such as multi-band performance, high-selectivity, small size, wide stopband suppression, and so on.

For enhancing the immunity to environmental noises, balanced-to-unbalanced (BTU) circuits are widely utilized to connect the balanced port and single-ended ports with common-mode noise suppression, in modern wireless communication systems. To meet

the requirements of conversion between balanced signal and unbalanced signal, high immunity to environment, and integrate multifunction design, many attentions have been focused on the BTU and balun microwave components.
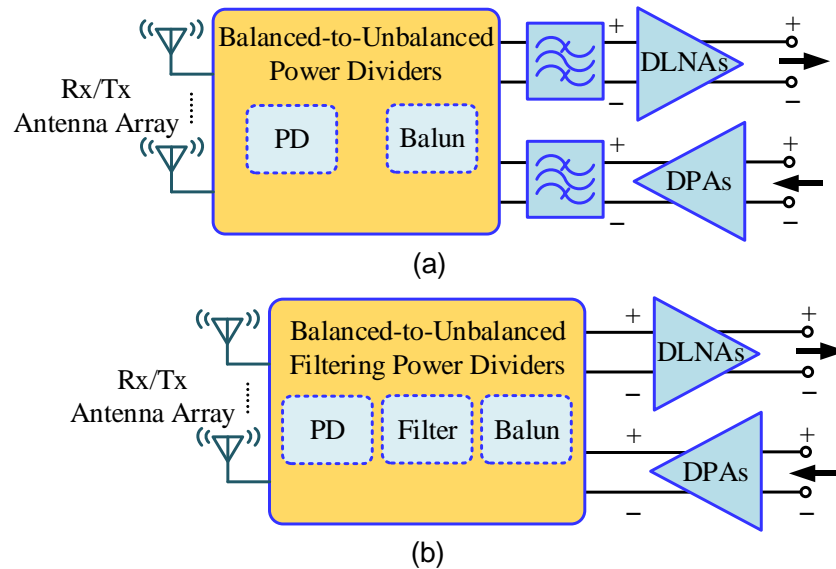
Fig. 1-3: The block of differential RF front-end systems. (a) Integrated BTU power divider without filtering. (b) Integrated BTU filtering power divider.

For BTU power divider (BTU PD), there are integration balun and power divider in one component to combine single-end signals from receiving antenna array (Rx antenna array) into differential signals for differential low noise amplifiers (DLNAs), or vice versa, as shown in Fig. 1-3(a). For further improving the integration of RF/microwave receive front-end, the BTU filtering power divider (BTU FPD) is researched to replace the BTU PD in Fig. 1-3(b). In the past researches, most of works are focus on how to design wideband BTU FPDs more or less, and only limited works have been done on the designs of variable bandwidth, or narrowband with multi-mode resonator (MMR).

The objective of this doctoral research is to investigate the resonance characteristics of two type of multi-mode resonators (MMRs) (Stub-Loaded Resonator, SLR and Dual-Resonance Resonator, DRR) systematically. For demonstration, a series of compact multi-band bandpass filters are realized by using the proposed two type MMRs, respectively. Moreover, the two type of MMRs were also used to design a dual-band filtering power divider and two BTU FPDs with bandwidth variable. Moreover, in those designs, multiple signal paths, mixed electric and magnetic coupling and source and

loaded coupling are introduced to improve the controllable of bandwidths and selectivity of passbands.

1.2 Literature Review on Multi-Band Filters

(a)

(b)
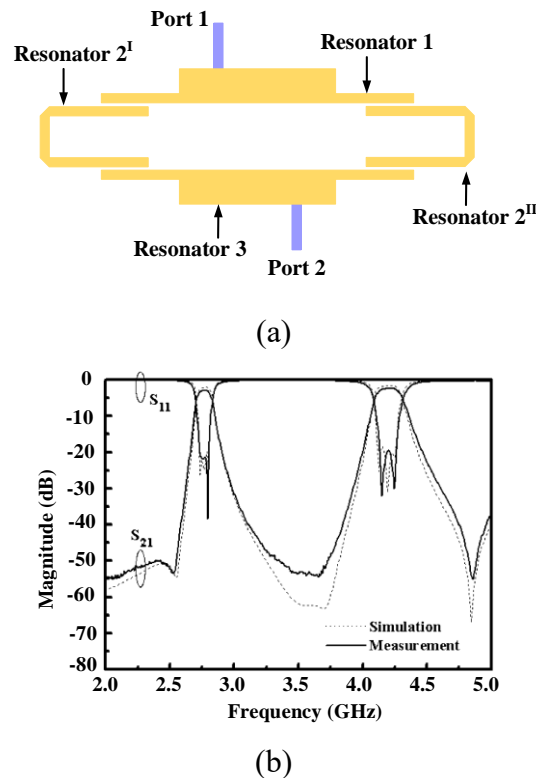
Fig. 1-4: (a) Layout of the Chebyshev dual-band BPF. (b) Measured and simulated results of the Chebyshev dual-band BPF.

Multi-band bandpass filters (BPFs) with compact size, low insertion loss, and high integration are great demand in modern multifunctional wireless communication systems, in above section 1.1. In the field of advanced multi-band wireless systems, filters with two- through seven-band operation for RF/microwave devices have become indispensable. They key ingredient in a BPF's design is the resonator. Up to now, many approaches have been used to design multi-band BPF, such as combine different BPFs with common feeding structure [11], [12], frequency transformation techniques [13], [14], and so on. One of the attractive and effective approaches is to use a MMR, such as a stepped impedance resonator (SIR) [15-18], stub-loaded resonator (SLR) [20-24], ring resonator [25-27], and other MRRs [28-30].

A widely used MMR that has become synonymous with multiband planar circuits is

the stepped impedance resonator (SIR), first introduced by Makimoto and Yamashita in the 1980s [15]. The resonator was introduced to control the spurious resonance frequencies while the fundamental frequency was fixed. So, it also used to design multi-band BPFs. In [16], a half-wavelength SIR was designed with impedance ratio larger than 1 to obtain two resonance frequencies at 2.8 GHz and 4.2 GHz, respectively. It was also shown that the electrical length ratio of the high and low impedance segments provided an additional degree of design freedom by which the resonance frequency could be fine-tuned. Twin uniform impedance resonators (UIRs) were designed for the two passbands and coupled to the SIRs, which showed improvement in the passband bandwidth due to the dual modes. The filter design layout and the responses are shown in Fig. 1-4.

(a)

(b)
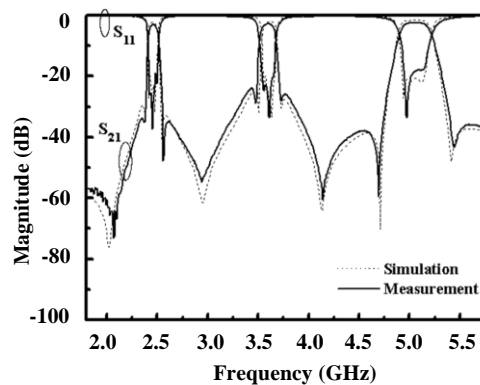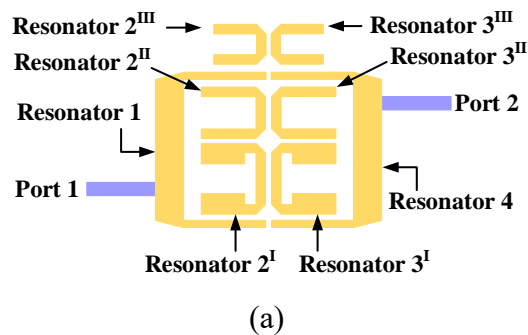
Fig. 1-5: (a) The layout of the quasi-elliptic triple-band BPF. (b) The measured and simulated results of the quasi-elliptic triple-band BPF.

A variant has been realized where, apart from the SIRs with impedance ratio larger than and the UIR, two more SIRs were designed with impedance ratio less than 1. A quasi-elliptic filter with a triple-band response is realized with compact folded stepped-

impedance resonators and U-shaped UIRs as the building block. The layout and S-parameters are shown in Fig. 1-5.

For improving the controllability of resonance frequency, a pair of stub-loaded shorted SIRs were cascaded to obtain a quad-band BPF in [17], as shown in Fig. 1-6(a). The proposed quad-band BPF consist of two order stub-loaded SIRs with mixed electric and magnetic coupling, and the four passbands are centered at 1.19, 3.33, 5.87, and 8.39 GHz with 3-dB FBW of 20%, 13.6%, 7.6%, and 15.4%, respectively. The size was compact, with overall dimensions of $0.169\lambda_g \times 0.127\lambda_g$. The guide wavelength corresponds to a center frequency of the first passband. Six TZs located at 1.57, 1.93, 4.48, 5.19, 7.03, and 7.45 GHz are measured among passbands, which lead to up to 30-dB band-to-band isolation in Fig. 1-6(b).

(a)

(b)

Fig. 1-6: (a) The layout of the quad-band BPF. (b) The measured and simulated results of the quad-band BPF.

It is known that the SIR should be introduced additional stubs to improve the controllability of the resonance frequencies in multi-band design. Therefore, the initial

application of UIR loaded with a stub was to achieve a higher number of passband modes [19]. Several stub-loading schemes have been proposed that integrated various resonator topologies. In 2008, an open-circuited and short-circuited stubs-loaded resonator was proposed and used to realize a tri-band BPF in Fig. 1-7 [20]. The first and third passband frequencies of the proposed tri-band BPF can be flexibly controlled by the lengths of the short-circuited and open-circuited, respectively, whereas the frequency of the second passband is fixed, as shown in Fig. 1-7(b) and (c).

(a)

(b)

(c)
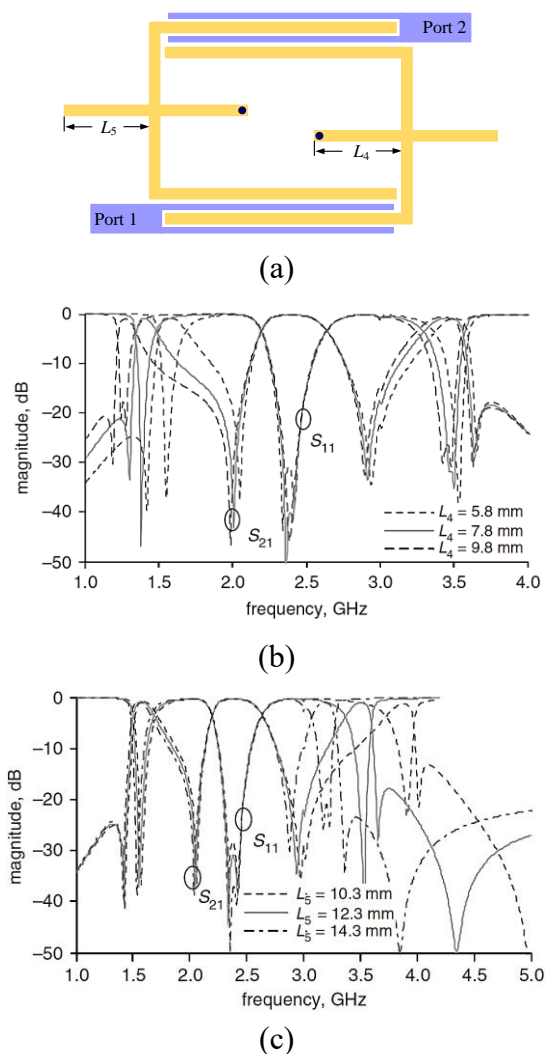
Fig. 1-7: (a) The layout of the tri-band BPF. (b) Simulated frequency responses of tri-band filter under different short-circuited stub length L_4. (c) Simulated frequency responses of tri-band filter under different open-circuited stub length L_5.

Based on the stub-loaded resonator (SLR) proposed in [20], a new class of double-stub-loaded UIRs came to be popularly known as cross resonators [21]. The contribution

of various sections of a cross-shaped resonator to the resonance characteristics is as follows. The half-wavelength UIR results in the second passband. The short stub creates the first passband, whereas the open stub results in the third passband. A pseudo-interdigital coupling topology between resonators was used to realize the compact size of the filter and create inherent transmission zeros in Fig. 1-8. The three passbands were centered at 2.4, 3.5, and 5.24 GHz, with all having a 3% FBW.

| (a) | (b) |
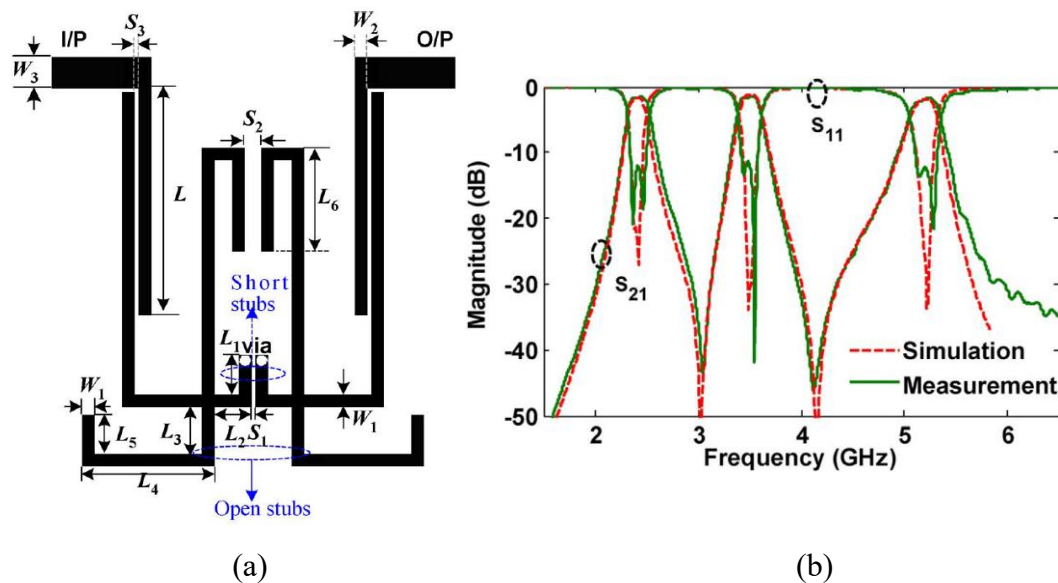
Fig. 1-8: (a) The layout of the tri-band filter using cascaded resonators. (b) Simulated and measured results of the tri-band filter using cascaded resonators.

In order to improve the design freedom and resonance mode, a square ring-loaded resonator (SRLR) was introduced in [22], where the first two odd modes and the first even-mode were utilized to design a triple band BPF. With the same topology of SRLR, a quad-mode performance was excited in [23]. This modified resonator can be considered a variant of the SLR, where more design freedom was achieved by adjusting the width of the ring that loads the UIR. A dual-band BPF, with passbands centered at 2.4 and 5.2 GHz, was designed and the layout and corresponding results of the dual-band BPF are illustrated in Fig. 1-9. For enhanced the controllability of four modes, the frequency dependence of the phase velocity for coupled meander-line–type slow-wave structures was used to realize a ring-loaded resonator in [24]. The modified SRLR was used to design a quad-band high superconducting BPF with center frequencies are 2.44, 3.55, 5.18, and 5.79 GHz, with corresponding 3-dB FBWs of 4.96%, 5.07%, 2.32%, and 3.63%,

respectively, in Fig. 1-10. Nevertheless, their design freedom degree is still need improve for quad-band BPF design. The bandwidths of the four passbands of the quad-band BPF cannot independent controllable.

(a)   (b)
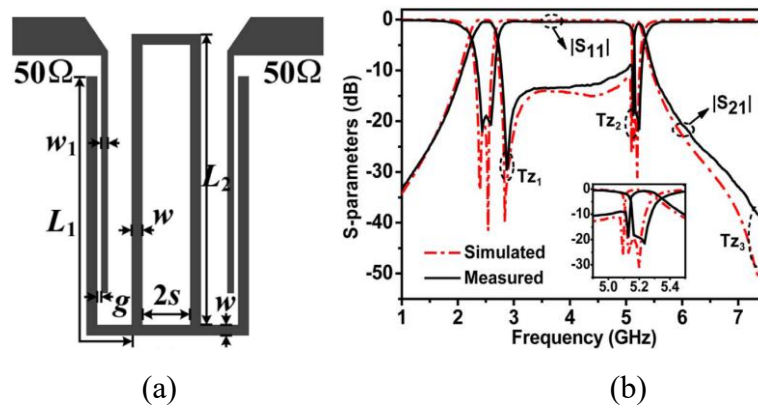
Fig. 1-9: (a) The layout of the designed dual-band BPF. (b) Simulated and measured frequency responses of the designed dual-band BPF.

(a)

(b)
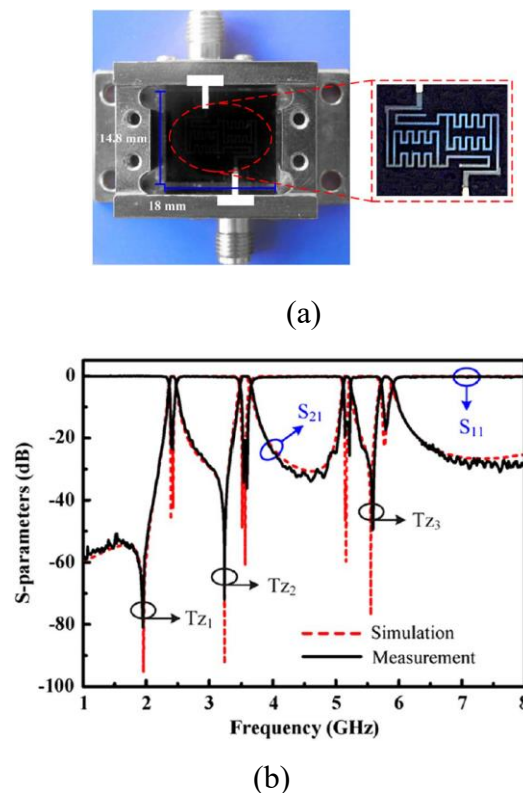
Fig. 1-10: (a) Photograph of the fabricated HTS quad-band filter with metal cover opened. (b) Simulated and measured frequency responses of the fabricated quad-band HTS filter.

Therefore, the independent controllable of the bandwidth and frequency of each passband is still a big challenge in the design of multi-band BPF. In this dissertation, we

focus on exploring a modified multi-mode resonators to improve the controllability of the resonance modes, and proposed novel method to realize bandwidth controllable and high selectivity performances.

1.3 Literature Review on Filtering Power Dividers

In wireless communication system, power divider have been widely used in splitting and input signal into two output signals and maintaining a good impedance matching at all ports. Recently, adding a frequency filtering feature to a power divider has been of a great interest in the field of circuit theories and designs, and relevant works can be found extensively in the literature [31-44]. Up to now, many efforts have been made on exploring the approach to synthesize and designing power divider with filtering response. One class of FPDs are obtained by modifying conventional Wilkinson power divider. For example, an UWB power divider on single-layer microstrip-line is proposed, analyzed and designed [31]. As shown in Fig. 1-11(a), this divider is constructed by introducing a pair of stepped-impedance open-circuited stubs and parallel coupled lines in two output ports, so that the sharp roll-off skirt can be achieved to better regulate the UWB performance. The simulated and measured results are shown in Fig. 1-11(b).

<div align="center">(a)   (b)</div>
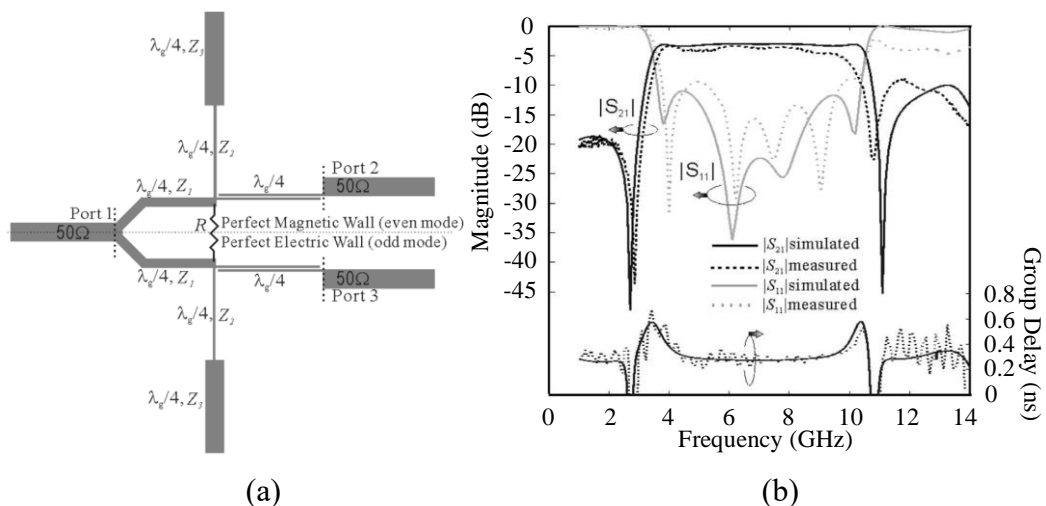
Fig. 1-12: (a) Schematic layout of proposed divider. (b) Predicted and measured S_{21} and S_{11} magnitudes as well as group delay of the proposed power divider.

In [33], a bandpass and lowpass filters are employed to substitute two quarter-wavelength lines in a conventional Wilkinson power divider for having a filtering feature,

as shown in Fig. 1-12. The proposed divider is fabricated on a 1.524 mm Rogers RO4003C substrate with a dielectric constant of 3.55 and a loss tangent of 0.0027. The passband filter realized a good frequency selectivity with measured passband return loss is >13 dB, and the insertion loss of each path is 3.68 dB with ±0.2 dB of imbalance. A pair of lowpass filters are used to formed a wide stopband characteristic with rejection level is >10 dB up to 22.2 f_0, where f_0 is the operating center frequency of the proposed power divider.

(a)

(b)

(c)
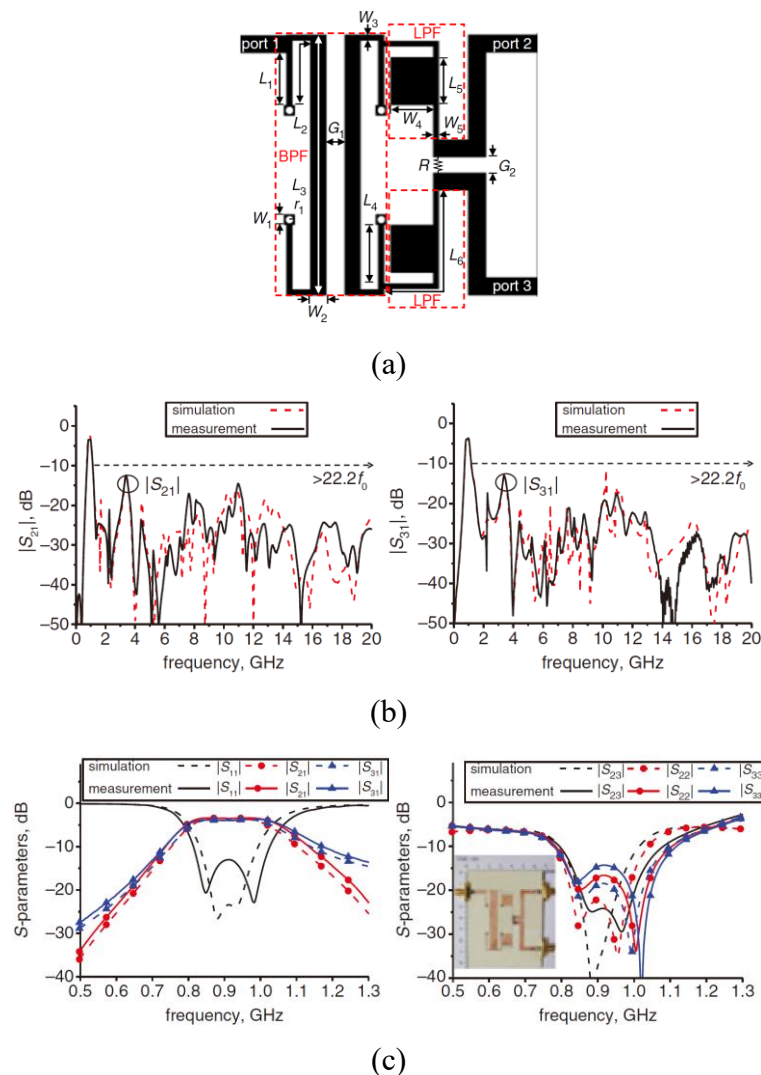
Fig. 1-12: (a) Schematic layout of proposed divider. (b) Wideband simulated and measured frequency responses of the proposed divider. (c) Narrowband simulated and measured frequency responses of the proposed divider.

By exploring embedding transversal signal-interference sections in a Wilkinson power divider, a wideband FPD is designed and realized in [34], as shown in Fig. 1-13(a).

Due to the employment of transversal signal-interference sections, this new Wilkinson divider possesses additional transmission zeros (TZs) and transmission poles (TPs) compared with the conventional one. This property leads to a 90% bandwidth (15-dB return loss) and sharp selectivity. In addition, by replacing the single isolation resistor with series resistor-inductor capacitor network, the isolation bandwidth is increased to about 200%.

(a)

(b)
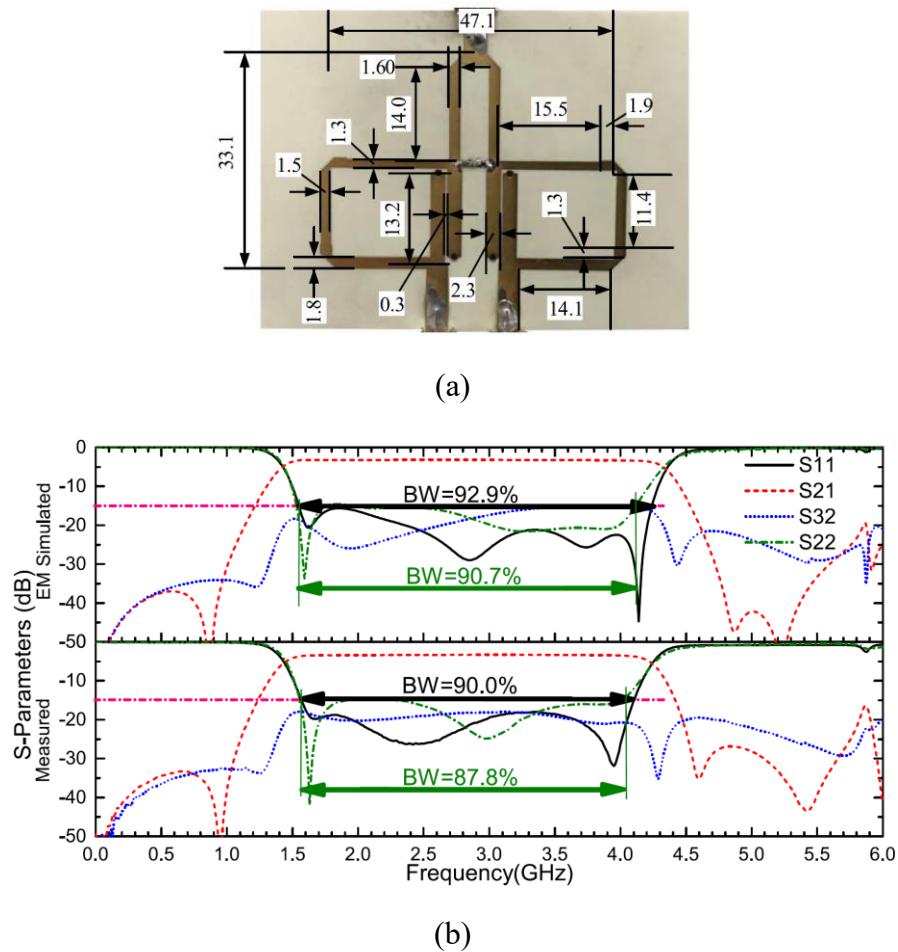
Fig. 1-13: (a) Photograph of the fabricated prototype of proposed wideband divider. (b) EM-simulated (top) and measured (bottom) S-parameters of the fabricated prototype.

Most of the previously reported works tried to achieve high frequency selectivity [32], [35] and harmonic suppression [36], [37] performances in a single-band or a wideband, yet there are a few papers on dual-band FPDs (DB-FPDs) [38]–[41]. In [39], by introducing a proper coupling topology between the quarter-wavelength (λ/4) short-ended microstrip line and two multi-mode resonators, the dual-band FPD is constructed,

as shown in Fig. 1-14(a). In this design, a pair of multi-mode resonators is readily introduced and properly coupled with a λ/4 short-ended microstrip line to realize dual-band filtering performance. Moreover, two 3λ/4 open stubs are loaded on the output coupled lines so as to further improve frequency selectivity and achieve wide stopband. The measured center frequencies of the two passbands are equal to 1.57 and 2.89 GHz with 3-dB FBWs of 22.3% and 7.6%, respectively, as shown in Fig. 1-14(b) and (c).

(a)

(b)

(c)
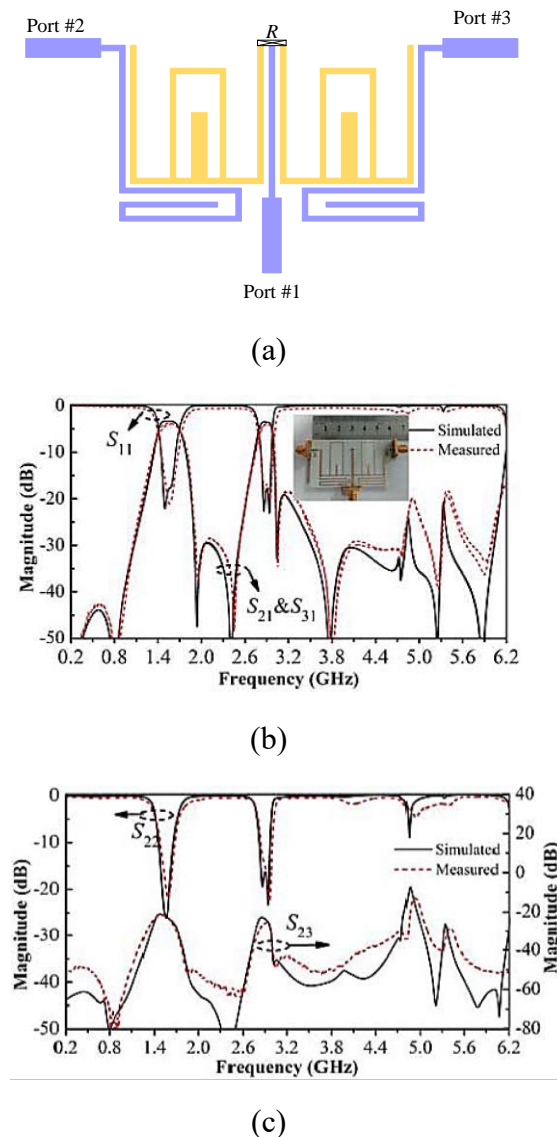
Fig. 1-14: (a) Layout of the proposed dual-band filtering power divider (FPD). (b) Measured and simulated magnitude of S_{11}, S_{21}, and S_{31} of the dual-band FPD. (c) Measured and simulated magnitude of S_{22} and S_{23} of the dual-band FPD.

These DB-FPDs exhibited good frequency selectivity and power division. However, their harmonic suppression property needs to be improved. In this dissertation, we

propose a novel DB-FPD with ultrawide stopband and good frequency selectivity. Two pairs of dual- resonance resonators (DRRs) are embedded into the output arms of Wilkinson power divider (WPD) to achieve a dual-band high frequency selectivity with multiple independently controllable resonance frequencies. Adopting a combined use of appropriately designed DRRs and a pair of spur-lines, a wide stopband up to $6f_0$ with 20 dB rejection level is realized. Moreover, compare with the previous works about DB-FPD, the proposed design method of DB-FPD is more simplify. This is the widest stopband of DB-FPDs reported thus far.

1.4 Literature Review on Balanced-to-Unbalanced Filtering Power Dividers

Balanced-to-unbalanced (BTU) circuits are widely utilized to connect the balanced port and single-ended ports with common-mode noise suppression, in modern wireless communication systems. To meet the requirements of conversion between balanced signal and unbalanced signal, high immunity to environment, and integrate multifunction design, many attentions have been focused on the BTU and balun microwave components, such as balun filters [44–46], BTU diplexers [47–49], and BTU power dividers (PDs) [50–64].

For BTU PD, there are integration balun and power divider in one component to combine single-end signals from receiving antenna array (Rx antenna array) into differential signals for differential low noise amplifiers (DLNAs), or vice versa. Over the past several years, BTU PDs have been studied based on square ring network [50-57]. In [50], shorted-ended four-wire coupled-line and T-shaped structure were used to design a BTU PD with operating bandwidth of 25% for the first time. The differential-mode power inputted from the balanced Port 1 is transmitted to two single-ended output Ports 2 and 3 with equal power division in Fig. 1-15. The common-mode power is reflected by Port 1 and no common-mode noise is transmitted to the two output ports. The two single-ended outputs are also isolated by using a lumped resistor. A four-wire coupled line and T-shaped structures are utilized for miniaturization.
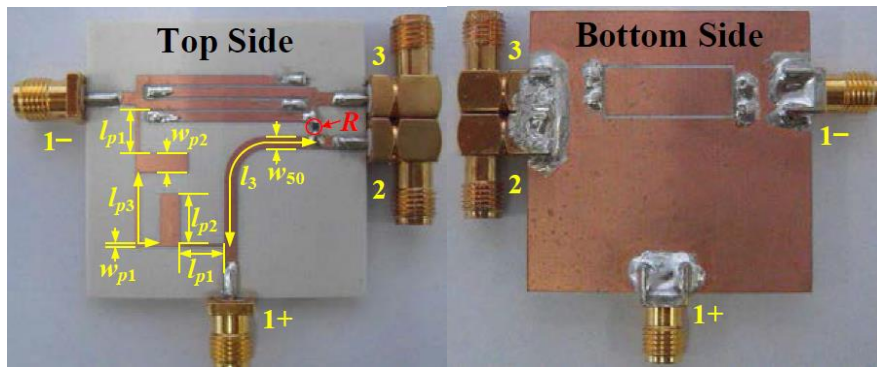
Fig. 1-15: Photo of the balanced-to-single-ended power divider prototype.

In order to enhance the operating bandwidth, three pairs of cascaded coupled-lines replaces the shorted-ended four-wire coupled-line, T-shaped structure and other transmission lines. Thus, the operating bandwidths are broadened to 37.2% [51] and 30% [54]. Moreover, those designs also realize a miniaturized circuit size. In [56], a wideband multilayer BTUB power divider integrating the functions of balun and power divider is proposed used to further enhance the bandwidth of BTU PD, whose physical structure is shown in Fig. 1-16. Despite the power division response with the bandwidth of 63% was achieved, the multilayer structure is difficult to fabricate.
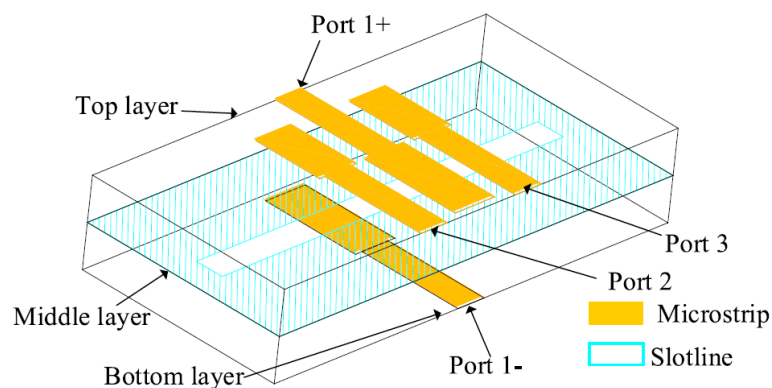
Fig. 1-16: Basic physical structure of the wideband BTUB power divider.

A wideband BTU FD using symmetrical transmission lines was presented in [57], and the bandwidth can be raised to 89.1%. All of the above mentioned previous works payed attention to BTU PDs design, which still need to connect filters in system applications. Therefore, BTU filtering power divider (FPD) with higher integration had been proposed based on branch-lines with several open-stubs [58], as shown in Fig. 1-

17(a), which is used to implement lower insertion loss and smaller circuit size. Power dividing, frequency selectivity, isolation between output ports, and common-mode suppression can be realized at the same time. The BTU FPD is fabricated on an RO4003C substrate with a dielectric constant of 3.38, a thickness of 0.813 mm, and a loss tangent of 0.0027. The simulated and measured results are shown in Fig. 1-17(b) with a DM fractional bandwidth of 7.7%, and CM suppression better than 20 dB from 1.75 to 3 GHz.

(a)

(b)

(c)
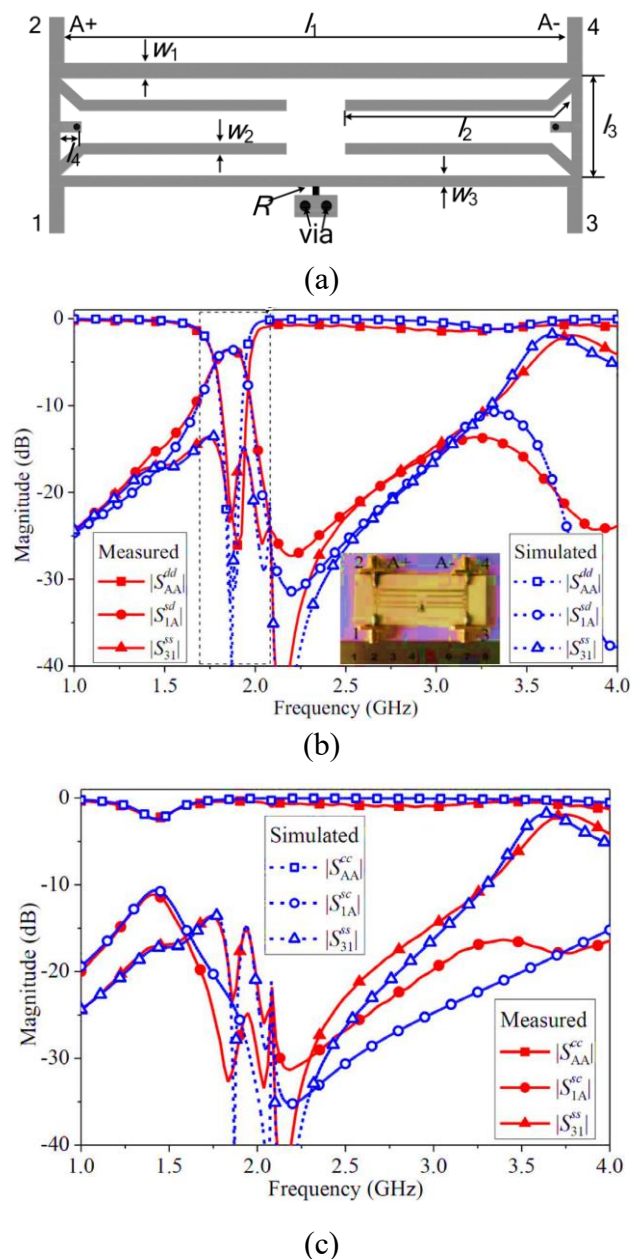
Fig. 1-17: (a) Layout of BTU FPD. (b) Photograph and differential mode simulated and measured responses. (c) Common mode simulated and measured responses.

A pair of coupled-lines is utilized to realize filtering response with wideband performance [59]. Moreover, open/shorted coupled-lines and half-wavelength open stubs were applied to introduce two transmission zeros near the passband, which enhance the selectivity of the proposed BTU FPD, while the in-band isolation also need to further improve. In [60], a novel wideband balanced-to-unbalanced filtering unequal power divider with wide stopband and isolation is proposed as shown in Fig.1-18(a). The wideband filtering response with high frequency selectivity can be realized easily using the modified two-port coupled lines with short- and open-circuit stubs, thus generating two transmission zeros near the passband. Additionally, the isolation between the unbalanced ports is better than 20 dB, illustrated in Fig. 1-18(b).

(a)

(b)
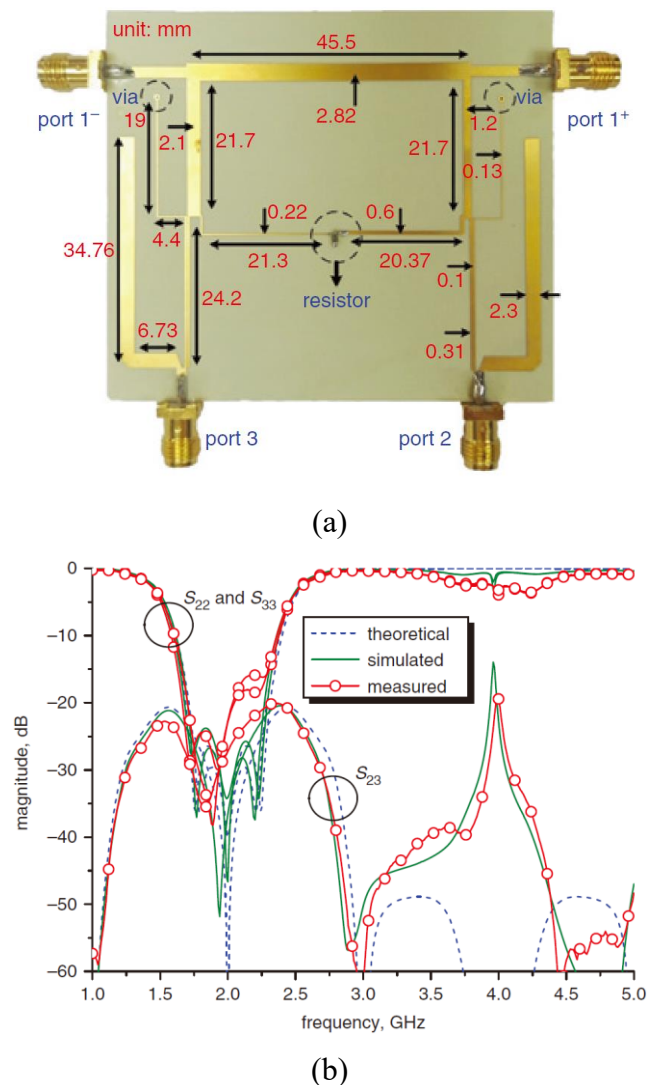
Fig. 1-18: (a) Photograph of fabricated wideband BTU FPD. (b) Theoretical, simulated, and measured results of single-ended ports responses.

For widening the frequency range of common mode (CM) suppression, a hybrid microstrip/slotline structure was used to design a filtering BTU PD (BTU FPD) with wider differential mode (DM) matching bandwidth and wider CM suppression bandwidth [62]. Despite this structure can achieve a better CM suppression, it is relatively difficult and expensive to process. Note that all the aforementioned works focus on how to design wideband BTU PDs more or less, and only limited works have been done on the design of variable bandwidth [58-65].

1.5 Organization of Chapters

The main contents of the dissertation are organized into six chapters and are described briefly as follows.

In Chapter 1, the background, current status, motivation, and objectives of the research are described.

In Chapter 2, the basic design theory of microwave filters, analysis method of microwave networks, fundamental principles of microwave Wilkinson power dividers, and basic concepts of microwave differential networks are briefly summarized.

In Chapter 3, at first, a novel type of stub-loaded stepped-impedance resonator (SL-SIR) is proposed. With different schematics of the loaded stubs, the SL-SIR has flexibly controllable dual-modes or tri-modes to construct dual-band or tri-band BPFs. Detailed mode analysis of the resonator is conducted, and parametric variations of the modes are investigated. Next, dual-band and tri-band BPFs are proposed and designed using the dual-mode or tri-mode SL-SIRs. Multiple geometrical parameters in both the external feeding structure and the internal couplings between neighboring resonators are employed to make the individual control of the two or three passbands possible. Furthermore, separately changeable multiple coupling paths between the resonators and the coupling paths between the source and load are devised to create multiple transmission zeros, which not only enhance significantly the selectivity of the passbands, but also widen greatly the stopband of the BPFs. A small H-shaped composite resonator is also proposed, and its even-mode and odd-mode are used to configure a miniaturized dual-band BPF with a flexible center frequency ratio. Three transmission zeros are produced by introducing a mixed electric and magnetic coupling between the resonators, which

improves significantly the selectivity and out-band rejection performance. All the designed dual-band and tri-band BPFs are fabricated, and their measured frequency responses agree well with the theoretically predicted ones.

In Chapter 4, a novel compact dual-band filtering power divider (DB-FPD) is developed which can reduce significantly the circuit size of a RF/microwave front-end. The proposed DB-FPD consists of a small U-shaped Wilkinson power divider, two pairs of dual-resonance resonators (DRRs), and a pair of spur-lines. With the simultaneous use and appropriate design of the coupled feedlines, mixed electric and magnetic couplings between the DRRs, and spur-lines with different lengths, multiple TZs are produced which result in two passbands with desired power division, high frequency selectivity, good isolation, and an ultrawide stopband. A prototype DB-FPD is designed, fabricated and measured. The measured responses agree well with the design simulations, exhibiting a stopband up to 13.8 GHz (6f0) with 20-dB rejection level. This is the widest stopband of DB-FPDs reported thus far.

In Chapter 5, two novel balanced to unbalanced filtering power dividers with variable bandwidth are proposed based on stub-loaded dual-mode resonators (SL-DMRs). Two SL-DMRs are used to replace the 90° horizontal transmission lines to realize filtering responses. With the even- and odd-mode analysis method and traditional transmission line theory, closed-form analytical equations and detail design procedures are derived. Moreover, a pair of parallel coupled-lines are used to feed the SL-DMRs, which not only realize variable bandwidth but also improve the stopband performance. Three transmission zeros (TZs) locate on both sides of the passband, which improve the selectivity of the passband. To verify the analytical theory and design method prediction, two prototypes are designed, fabricated, and measured. The measured responses agree well with the design simulations, exhibiting a good frequency selectivity, isolation, and common-mode suppression.

In Chapter 6, the main research works and obtained results of this dissertation are summarized, and a brief discussion on prospective future works is also provided.

References

[1] Z. H. Jiang, and D. H. Werner, "A compact, wideband circularly polarized co-designed filtering antenna and its application for wearable devices with low SAR," *IEEE Trans. Antennas Propag.*, vol. 63, no. 9, pp. 3808–3818, Sep. 2015

[2] H. –W. Deng, T. Xu, and F. Liu, "Broadband pattern-reconfigurable filtering microstrip antenna with quasi-Yagi structure," *IEEE Antennas Wireless Propag. Lett.*, vol. 17, no. 7, pp. 1127–1131, Jul. 2018.

[3] P. F. Hu, Y. M. Pan, X. Y. Zhang, and B. J. Hu, "A compact quasi-isotropic dielectric resonator antenna with filtering response," *IEEE Trans. Antennas Propag.*, vol. 67, no. 2, pp. 1294–1299, Feb. 2019.

[4] F. Haung, J. Wang, L. Zhu, "A new approach to design a microstrip dual-mode balun bandpass filter," *IEEE Microw. Wireless Compon. Lett.*, vol. 26, no. 4, pp. 252–254, Apr. 2016.

[5] J. –M. Yan, H. –Y. Zhou, and L. –Z. Cao, "A novel filtering balun and improvement of its isolation performances," *IEEE Microw. Wireless Compon. Lett.*, vol. 27, no. 12, pp. 1056–1058, Dec. 2017.

[6] X. D. Wang, J. P. Wang, G. Zhang, J. -S. Hong, and W. Wu, "Dual-wideband filtering power divider with good isolation and high selectivity," *IEEE Microw. Wireless Compon. Lett.*, vol. 27, no. 12, pp. 1071–1073, Dec. 2017.

[7] X. Wang, J. Wang, and G. Zhang, "Design of wideband filtering power divider with high selectivity and good isolation," *Electron. Lett.*, vol. 52, no. 16, pp. 1389–1391, Aug. 2017.

[8] S. –J. Sun, T. Su, K. Deng, B. Wu, and C. –H. Hong, "Shorted-ended stepped-impedance dual-resonance resonator and its application to bandpass filters," *IEEE Trans. Microw. Theory Techn.*, vol. 61, no. 9, pp. 3209–3215, Sep. 2013.

[9] K. Xu, J. Shi, L. and Lin, J. –X. Chen, "A balanced-to-unbalanced microstrip power divider with filtering function," *IEEE Trans. Microw. Theory Techn.*, vol. 63, no. 8, pp. 2561–2569, Aug. 2015.

[10] X. Gao, W. Feng, W. Che, and Q. Xue, "Wideband balanced-to-unbalanced filtering power dividers based on coupled lines," *IEEE Trans. Microw. Theory Techn.*, vol. 65, no. 1, pp. 86–95, Jan. 2017.

[11] L. C. Tsai, and C. W. Hsue, "Dual band bandpass filters using equal-length coupled-serial-shunted lines and Z-transform technique," *IEEE Trans. Microw. Theory Techn.*, vol. 52, no. 4, pp. 1111-1117, Apr. 2004.

[12] C. –Y. Chen, and C. –Y. Hsu, "A simple and effective method for microstrip dual-band filters design," *IEEE Microw. Wireless Compon. Lett.*, vol. 16, no. 5, pp. 246–248, May 2017.

[13] X. Guan, Z. Ma, P. Cai, Y. Kobayashi, T. Anada, and G. Hagiwara, "Synthesis of dual-band bandpass filters using successive frequency transformations and circuit conversions," *IEEE Microw. Wireless Compon. Lett.*, vol. 16, no. 3, pp. 110–112, Mar. 2006.

[14] A. Garcia-Lamperez and M. Salazar-Palma, "Single-band to multiband frequency transformation for multiband filters," *IEEE Trans. Microw. Theory Techn.*, vol. 59, no. 12, pp. 3048-3058, Dec. 2011.

[15] M. Makimoto and S. Yamashita, *Microwave Resonators and Filters for Wireless Communication*, Berlin, Germany: Springer-Verlag, 2003.

[16] C.-F. Chen, T.-Y. Huang, and R.-B. Wu, "Design of dual- and triple passband filters using alternately cascaded multiband resonators," *IEEE Trans. Microwave Theory Tech.*, vol. 54, no. 9, pp. 3550–3557, Sep. 2006.

[17] J. Xu, W. Wu, and C. Miao, "Compact microstrip dual-/tri-/quad-band bandpass filter using open stubs loaded shorted stepped-impedance resonator," *IEEE Trans. Microwave Theory Tech.*, vol. 61, no. 9, pp. 3187–3199, Sep. 2013.

[18] X.-B. Wei, P. Wang, P. Gao, Z.-Q. Xu, J.-X. Liao, L. Jin, and Y. Shi, "Compact tri-band band pass filter using open stub loaded tri-section λ/4 stepped impedance resonator," *IEEE Microwave Wireless Compon. Lett.*, vol. 24, no. 8, pp. 512–514, Aug. 2014.

[19] J. –S. Hong, *Microstrip Filters for RF Microwave Applications*. Hoboken, NJ: Wiley, 2011.

[20] F. –C. Chen, Q. –X. Chu, and Z. –H. Tu, "Tri-band bandpass filter using stub loaded resonators," *Electron. Lett.*, vol.44, no. 12, pp. 747-749, Jun. 2008.

[21] Q. X. Chu, F. C. Chen, Z. H. Tu, and H. Wang, "A novel crossed shaped resonator and its application to bandpass filters," *IEEE Trans. Microwave Theory Tech.*, vol. 57, no. 7, pp. 1753–1759, Jul. 2009.

[22] J. –Z. Chen, N. Wang, Y. He, and C.–H. Liang, "Fourth-order triband bandpass filter using square ring loaded resonators," *Electron. Lett.*, vol. 47, no. 15, pp. 858–859, Jul. 2011.

[23] H. Liu, B. Ren, X. Guan, J. Lei, and S. Li, "Compact dual-band bandpass filter using quadruple-mode square ring loaded resonator (SRLR)," *IEEE Microwave Wireless Compon. Lett.*, vol. 23, pp. 181–183, Apr. 2013.

[24] H. Liu, B. Ren, X. Guan, P. Wen, and Y. Wang, "Quad band high temperature superconducting bandpass filter using quadrature mode square ring loaded resonator," *IEEE Trans. Microwave Theory Tech.*, vol. 62, no. 12, pp. 2931–2941, Dec. 2014.

[25] C. –Y. Hsu, C. –Y. Chen, H. –R. Chuang, "A miniaturized dual-band bandpass filter using embedded resonators," *IEEE Microwave Wireless Compon. Lett.*, vol. 21, no. 12, pp. 658–660, Dec. 2011.

[26] L. Wang and B.-R. Guan, "Compact and high selectivity tri-band BPF using nested DDGSRs," *Electron. Lett.*, vol. 48, no. 7, pp. 378–379, Mar. 2012.

[27] R. –H. Geschke, B. Jokanovic and P. Meyer, "Filter parameter extraction for triple band composite split-ring resonators and filters," *IEEE Trans. Microwave Theory Tech.*, vol. 59, no. 6, pp. 1500–1508, Jun. 2011.

[28] L. Ren and H. Huang, "Dual-band bandpass filter based on dual plane microstrip/inter-digital DGS slots structure," *Electron. Lett.*, vol. 45, no. 21, pp. 1077–1079, 2009.

[29] C. –H. Tseng and H. –Y. Shao, "A new dual-band microstrip bandpass filter using net-type resonators," *IEEE Microwave Wireless Compon. Lett.*, vol. 20, no. 4, pp. 196–198, Apr. 2010.

[30] L.-Y. Ren, "Quad-band bandpass filter based on dual plane microstrip/DGS slot structure," *Electron. Lett.*, vol. 46, no. 10, pp. 691–692, May 2010.

[31] S. W. Wong, and L. Zhu, "Ultra-wideband power divider with good in-band splitting and isolation performances," *IEEE Microwave Wireless Compon. Lett.*, vol. 18, no. 8, pp. 518–520, Apr. 2010.

[32] G. Zhang, X. D. Wang, J. -S. Hong, and J. Q. Yang, "A high- performance dual-mode filtering power divider with simple layout," *IEEE Microw. Wireless Compon. Lett.*, vol. 28, no. 2, pp. 120–122, Feb. 2018.

[33] W. –M. Chau, K. –W. Hsu, and W. –H. Tu, "Wide-stopband Wilkinson power divider with bandpass response," *Electron. Lett.*, vol. 50, no. 1, pp. 39–40, Jan. 2014.

[34] L. Jiao, Y. Wu, Y. Liu, Q. Xue, and Z. Ghassemlooy, "Wideband filtering power divider with embedded transversal signal-interference sections," *IEEE Microw. Wireless Compon. Lett.*, vol. 27, no. 12, pp. 1068–1070, Dec. 2017.

[35] X. Wang, J. Wang, and G. Zhang, "Design of wideband filtering power divider with high selectivity and good isolation," *Electron. Lett.*, vol. 52, no. 16, pp. 1389–1391, Aug. 2017.

[36] Y. Wang, X. Y. Zhang, F. –X. Liu, and J. –C. Lee, "A compact bandpass Wilkinson power divider with ultra-wide band harmonic suppression," *IEEE Microw. Wireless Compon. Lett.*, vol. 27, no. 10, pp. 888–890, Oct. 2017.

[37] X. Y. Zhang, K. X. Wang, and B. J. Hu, "Compact filtering power divider with enhanced second-harmonic suppression," *IEEE Microw. Wireless Compon. Lett.*, vol. 23, no. 9, pp. 483–485, Sep. 2013.

[38] Y. C. Li, Q. Xue, and X. Y. Zhang, "Single- and dual-band power dividers integrated with bandpass filters," *IEEE Trans. Microw. Theory Techn.*, vol. 61, no. 1, pp. 69–76, Jan. 2013.

[39] G. Zhang, J. P. Wang, L. Zhu, and W. Wu, "Dual-band filtering power divider with high selectivity and good isolation," *IEEE Microw. Wireless Compon. Lett.*, vol. 26, no. 10, pp. 774–776, Oct. 2016.

[40] Y. L. Wu, Z. Zhuang, G. Y. Yan, Y. A. Liu, and Z. Ghassemlooy, "Generalized dual-band unequal filtering power divider with independently controllable bandwidth," *IEEE Trans. Microw. Theory Techn.*, vol. 65, no. 10, pp. 3838–3848, Oct. 2017.

[41] X. D. Wang, J. P. Wang, G. Zhang, J. -S. Hong, and W. Wu, "Dual-wideband filtering power divider with good isolation and high selectivity," *IEEE Microw. Wireless Compon. Lett.*, vol. 27, no. 12, pp. 1071–1073, Dec. 2017.

[42] Y. L. Wu, Z. Zhuang, G. Y. Yan, Y. A. Liu, and Z. Ghassemlooy, "Generalized dual-band unequal filtering power divider with independently controllable bandwidth," *IEEE Trans. Microw. Theory Techn.*, vol. 65, no. 10, pp. 3838–3848, Oct. 2017.

[43] X. D. Wang, J. P. Wang, G. Zhang, J. -S. Hong, and W. Wu, "Dual-wideband filtering power divider with good isolation and high selectivity," *IEEE Microw. Wireless Compon. Lett.*, vol. 27, no. 12, pp. 1071–1073, Dec. 2017.

[44] S. –J. Sun, T. Su, K. Deng, B. Wu, and C. –H. Hong, "Shorted-ended stepped-impedance dual-resonance resonator and its application to bandpass filters," *IEEE Trans. Microw. Theory Techn.*, vol. 61, no. 9, pp. 3209–3215, Sep. 2013.

[45] J. Wang, F. Huang, L. Zhu, C. Cai, and W. Wu, "Study of a new planar-type balun topology for application in the design of balun bandpass filters," *IEEE Trans. Microw. Theory Techn.*, vol. 64, no. 9, pp. 2824–2832, Sep. 2016.

[46] J. –X. Chen, Y. Zhan, W. Qin, and Z.-H. Bao, "Design of high-performance filtering balun based on TE01-mode dielectric resonator," *IEEE Trans. Ind. Electron.*, vol. 64, no. 1, pp. 451–458, Jan. 2017.

[47] L. –P. Feng, and L. Zhu, "Compact wideband filtering balun using stacked composite resonators," *IEEE Access*, vol. 6, pp. 34651–34658, Jul. 2018.

[48] C. –H. Wu, C. –H. Wang, and C. H. Chen, "A novel balanced-to-unbalanced diplexer based on four-port balanced-to-balanced bandpass filter," *Proceedings of the 38th European Microwave Conference*, pp. 28–31, 2008.

[49] Q. Xue, J. Shi, and J. –X. Chen, "Unbalanced-to-balanced and balanced-to-unbalanced diplexer with high selectivity and common-mode suppression," *IEEE Trans. Microw. Theory Techn.*, vol. 59, no. 11, pp. 2848–2855, Nov. 2011.

[50] C. –M. Chen, S. –J. Chang, C. –F. Yang, and C. –Y. Chen, "A simple and effective method for designing frequency adjustable balun diplexer with high common-mode suppression," *IEEE Microw. Wireless Compon. Lett.*, vol. 25, no. 7, pp. 433–435, Jul. 2015.

[51] L. S. Wu, Y. X. Guo, L. F. Qiu, and J. F. Mao, "A new balanced-to-single-ended (BTSE) power divider," in *Proc. IEEE Int. Wireless Symp.*, 2014, pp. 1–4.

[52] W. Zhang, Y. Wu, Y. Liu, F. M. Ghannouchi, and A. Hasan, "A wideband balanced-to-unbalanced coupled-line power divider," *IEEE Microw. Wireless Compon. Lett.*, vol. 26, no. 6, pp. 410–412, Jun. 2016.

[53] A. N. Yadav, and R. Bhattacharjee, "Balanced to unbalanced power divider with arbitrary power ratio," *IEEE Microw. Wireless Compon. Lett.*, vol. 26, no. 11, pp. 885–887, Nov. 2016.

[54] Y. Wu, Z. Zhuang, L. Jiao and Y. Liu, "A novel balanced-to-unbalanced complex impedance-transforming in-phase power divider," *IEEE Access*, vol. 5, pp. 16205–16213, Sep. 2017.

[55] J. Shi, J. Lu, K. Xu, and J. –X. Chen, "A coupled-line balanced-to-single-ended out-of-phase power divider with enhanced bandwidth," *IEEE Trans. Microw. Theory Techn.*, vol. 65, no. 2, pp. 459–466, Feb. 2017.

[56] W. Zhang, X. Shen, Y. Wu, Y. Liu, A. Hasan, F. M. Ghannouchi, and Y. Zhao, "Planar miniaturized balanced-to-single-ended power divider based on composite left- and right-handed transmission lines," *IEEE Microw. Wireless Compon. Lett.*, vol. 27, no. 3, pp. 242–244, Mar. 2017.

[57] X. Ren, and K. D. Xu, "Multilayer balanced-to-unbalanced power divider with wideband transmission characteristic and common-mode suppression," *IEEE Trans. Compon., Pakag., Manuf. Technol.,* vol. 9, no. 1, pp. 72–79, Jan. 2019.

[58] W. Feng, M. Hong, M. Xun, and W. Che, "A novel wideband balanced-to-unbalanced power divider using symmetrical transmission lines," *IEEE Microw. Wireless Compon. Lett.*, vol. 27, no. 4, pp. 338–340, Apr. 2017.

[59] K. Xu, J. Shi, L. and Lin, J. –X. Chen, "A balanced-to-unbalanced microstrip power divider with filtering function," *IEEE Trans. Microw. Theory Techn.*, vol. 63, no. 8, pp. 2561–2569, Aug. 2015.

[60] X. Gao, W. Feng, W. Che, and Q. Xue, "Wideband balanced-to-unbalanced filtering power dividers based on coupled lines," *IEEE Trans. Microw. Theory Techn.*, vol. 65, no. 1, pp. 86–95, Jan. 2017.

[61] Z. Zhuang, Y. Wu, L. Jiao, W. Wang, and Y. Liu, "Wideband balanced-to-unbalanced filtering unequal power divider with wide stopband and isolation," *Electron. Lett.*, vol. 53, no. 13, pp. 892–894, Jun. 2017.

[62] M. Luo, X. –H. Tang, D. Lu, Y. –H. Zhang, and X. –M. Yu, "Balanced-to-unbalanced filtering power divider with compact size and high common-mode suppression," *Electron. Lett.*, vol. 54, no. 8, pp. 509–511, Apr. 2018.

[63] L. Li, W. Cheng, L. –S. Wu, J. –F. Mao, M. Tang and X. –W. Gu, "A wideband filtering balanced-to-unbalanced out-of-phase power divider," *IEEE Microw. Wireless Compon. Lett.*, vol. 28, no. 10, pp. 870–873, Oct. 2018.

[64] L. Jiao, Y. Wu, Z. Zhuang, Y. Liu, and A. A. Kishk, "Planar balanced-to-unbalanced In-phase power divider with wideband filtering response and ultra-wideband common-mode rejection," *IEEE Trans. Circuits Syst. I, Reg. Papers,* vol. 65, no. 6, pp. 1875–1886, Jun. 2018.

[65] F. Huang, J. Wang, J. Hong, and W. Wu, "A new balanced-to-unbalanced filtering power divider with dual controllable passbands and enhanced in-band common-mode suppression," *IEEE Trans. Microw. Theory Techn.*, vol. 67, no. 2, pp. 695–703, Feb. 2019.

Chapter 2

Fundamental Design Theory of Filters and Power Dividers

2.1 Overview

This chapter introduces basic concepts and theories that form the foundation for designing RF/microwave passive components, including bandpass filters, filtering power dividers, and balanced-to-unbalanced filtering power dividers. The topics will cover the basic concepts of microwave filters, coupled resonators, coupled-lines, microwave networks analysis, basic properties and theory of power divider, and mixed-mode S-parameter of differential circuits. Those topics are summarized from open literatures to guide the design of subsequent chapters [1-5].

2.2 Basic Concepts and Coupled-Line Filters

2.2.1 General Definitions of Filters

Most of the microwave filters can be represented by a two-port network. The transfer function S_{21} is a mathematical description of network response characteristics. On many occasions, an amplitude-squared transfer function for a lossless passive filter network is defined as [1]

$$\left|S_{21}\left(j\Omega\right)\right|^2 = \frac{1}{1+\varepsilon^2 F_n^2\left(\Omega\right)} \tag{2.1}$$

where ε is a ripple constant, $F_n(\Omega)$ represents a filtering or characteristic function, and Ω is frequency variable. For our discussion here, it is convenient to let Ω represent a radian frequency variable of a lowpass prototype filter that has a cutoff frequency at $\Omega_c = 1$ (rad/s).

For a given transfer function of (2.1), the insertion loss response L_A and the return loss response L_R of the filter can be defined as follows:

$$L_A(\Omega) = 10\log\frac{1}{\left|S_{21}(j\Omega)\right|^2} \tag{2.2}$$

$$L_R(\Omega) = 10\log\left[1 - \left|S_{21}(j\Omega)\right|^2\right] \tag{2.3}$$

2.2.2 Coupled Resonators

In microstrip filter design, the important step is to establish the relationship between the value of every required coupling coefficient and the physical structure of coupled resonators in order to find the physical dimensions of the filter for fabrication. Fig. 2-1 depicts the general model of two coupled resonators where resonators 1 and 2 can be different in structure and have different resonant frequencies. In general, the coupling coefficient may be defined on the basis of a ratio of coupled to stored energy as

$$k = \frac{\iiint \varepsilon \boldsymbol{E}_1 \cdot \boldsymbol{E}_2 \, dv}{\sqrt{\iiint \varepsilon \left|\boldsymbol{E}_1\right|^2 dv \times \iiint \varepsilon \left|\boldsymbol{E}_2\right|^2 dv}} + \frac{\iiint \varepsilon \boldsymbol{H}_1 \cdot \boldsymbol{H}_2 \, dv}{\sqrt{\iiint \varepsilon \left|\boldsymbol{H}_1\right|^2 dv \times \iiint \varepsilon \left|\boldsymbol{H}_2\right|^2 dv}} \tag{2.4}$$

where $\boldsymbol{E}$ and $\boldsymbol{H}$ represent the electric and magnetic field vectors, respectively.

We can use the more traditional notation k instead of M for the coupling coefficient. Note that all fields are determined at resonance and the volume integrals are over entire effecting regions with permittivity of ε and permeability of μ. The first term on the right-hand side represents the electric coupling, while the second term represents the magnetic coupling. It should be remarked that the interaction of the coupled resonators is mathematically described by the dot operation of their space vector fields, which allows the coupling to have either positive or negative sign. A positive sign would imply that the coupling enhances the stored energy of uncoupled resonators, whereas a negative sign would indicate a reduction. Therefore, the electric and magnetic couplings could either have the same effect if they have the same sign, or have the opposite effect if their signs are opposite. Obviously, the direct evaluation of coupling coefficient from (2.4) requires the knowledge of the field distributions and performance of the space integrals. This is not an easy task unless analytical solutions of the fields exist.
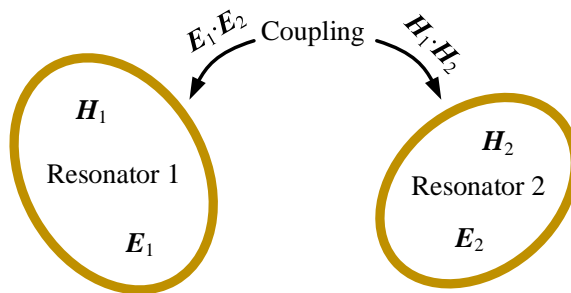
Fig. 2-1: Coupling model of resonator 1 and 2 can be different in structure and have different resonant frequencies.

Moreover, it may be much easier by using full-wave EM simulation or experiment to find some characteristic frequencies that are associated with the coupling of coupled RF/microwave resonators. The coupling coefficient can then be determined against the physical structure of coupled resonators if the relationship between the coupling coefficient and the characteristic frequencies is established. In what follows, we derive the formulation of such relationships.

In general, the coupling between two resonators with the same resonant frequency have three situations such as electric coupling, magnetic coupling and mixed coupling. In filter design, the mixed coupling case are widely used to produce transmission zeros to improve the selectivity of the filter. Therefore, we will introduce the mixed couplings in this section, and the electric coupling and magnetic coupling are described in detail in [1]. For coupled-resonator structures, with both the electric and magnetic couplings, a network representation is given in Fig. 2-2. Notice that the Y parameters are the parameters of a two-port network located on the left side of reference plane T_1-T'_1 and the right side of reference plane T_2-T'_2, while the Z parameters are the parameters of the other two-port network located on the right side of reference plane T_1-T'_1 and the left side of reference plane T_2-T'_2. The Y and Z parameters are defined by

$$\begin{aligned} Y_{11} = Y_{22} &= j\omega C \\ Y_{12} = Y_{21} &= j\omega C'_m \end{aligned} \tag{2.5}$$

$$\begin{aligned} Z_{11} = Z_{22} &= j\omega L \\ Z_{12} = Z_{21} &= j\omega L'_m \end{aligned} \tag{2.6}$$

where C, L, C'_m, and L'_m are the self-capacitance, the self-inductance, the mutual

capacitance, and the mutual inductance of an associated equivalent lumped-element circuit shown in Fig. 2-2. One can also identify an impedance inverter $K = \omega L'_m$ and an admittance inverter $J = \omega C'_m$, which represent the magnetic coupling and the electric coupling, respectively.
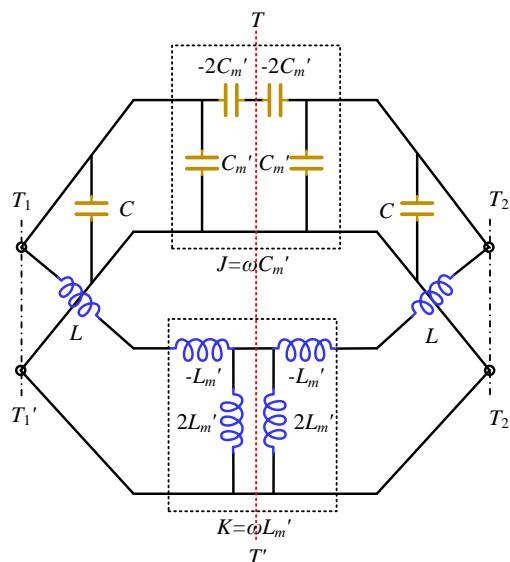
Fig. 2-2: Equivalent circuit of the mixed coupling.

By inserting an electric wall and a magnetic wall, respectively, into the symmetry plane of the equivalent circuit in Fig. 2-2, we obtain

$$f_e = \frac{1}{2\pi\sqrt{\left(L - L'_m\right)\left(C - C'_m\right)}} \tag{2.7}$$

$$f_m = \frac{1}{2\pi\sqrt{\left(L + L'_m\right)\left(C + C'_m\right)}} \tag{2.8}$$

From the (2.7) and (2.8), it can be seen that both the magnetic and electric couplings have the same effect on the resonant frequency shifting. And the mixed coupling coefficient k_x can be found to be

$$k_X = \frac{f_e^2 - f_m^2}{f_e^2 + f_m^2} = \frac{CL'_m + LC'_m}{LC + L'_m C'_m} \tag{2.9}$$

2.2.3 Coupled Transmission Lines

In section 2.2.2, the design of coupling resonator filter has been introduced,

especially the relationship between coupling coefficient and the physical structure. In this section, we will descript one of the classical physical structure: coupled transmission line, which also called coupled line. When two unshielded transmission lines (as shown in Fig. 2-3) are placed in close proximity to each other, a fraction of the power present on the main line is coupled to the secondary line.
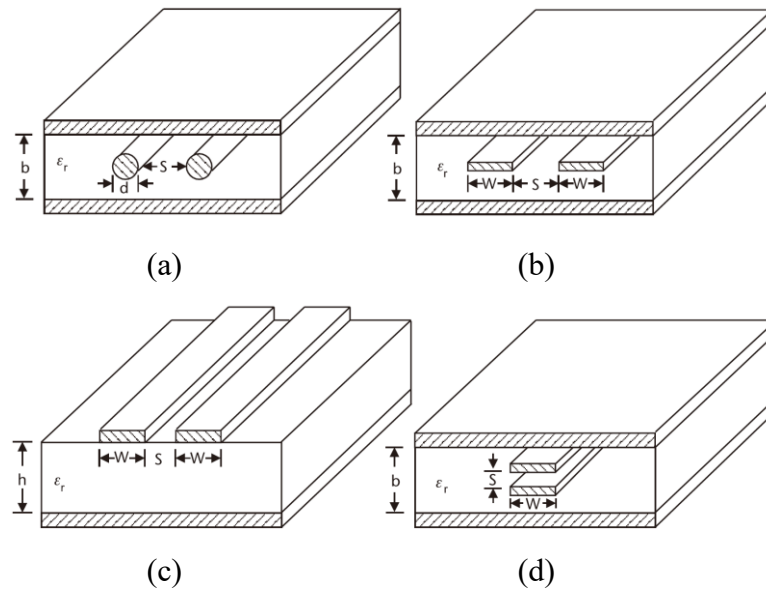
Fig. 2-3: Coupled transmission lines: (a) coaxial lines, (b) Striplines, (c) microstrip lines, and (d) broadside striplines.

Coupled-line structures are available for all forms and types of transmission lines/ dielectric guides and waveguides. Striplines, microstrip lines, coplanar waveguides, image guides, and insular and inverted strip guides are the most popular planar forms. In the part, we will introduces the coupling mechanism with the microstrip coupled lines as an example, and the other forms are described in [2].

The symmetric coupled-line structures, as shown in Fig. 2-3(c), support two modes: even and odd. The interaction between these modes induces the coupling between the two transmission lines, and the properties of the symmetric coupled structures may be described in terms of a suitable linear combination of these modes. The field distributions for the even and odd modes on coupled microstrip lines are shown in Fig. 2-4. In even-mode excitation, both microstrip conductors are at same potential while the odd mode delineates equal but of opposite polarity potentials with respect to the ground. The even

and odd modes have different characteristic impedances, and their values become equal when the separation between the conductors is very large (lines are uncoupled). The even-mode characteristic impedance (Z_{0e}) is the impedance from one line to the ground when both lines are driven in-phase from equal sources of equal impedances and voltages. The odd-mode characteristic impedance (Z_{0o}) is defined as the impedance from one line to the ground when both lines are driven out of phase from equal sources of equal impedances and voltages.
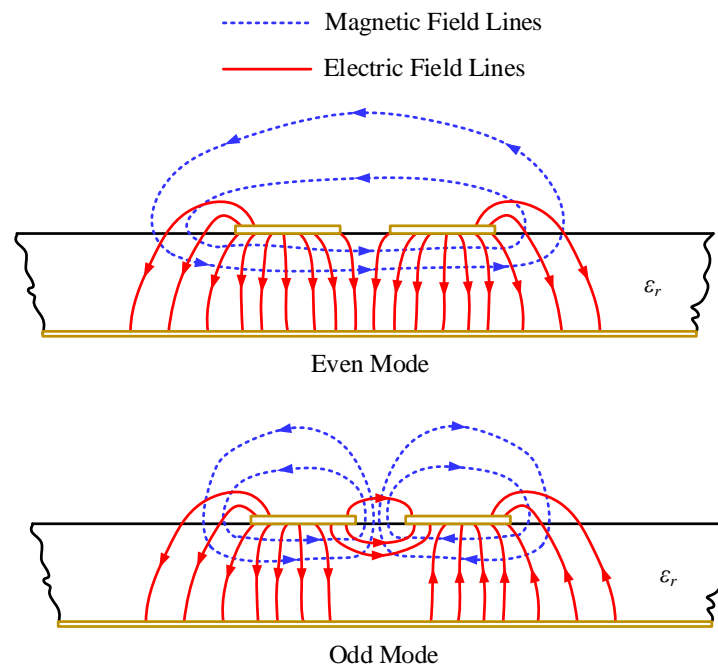
Fig. 2-4: Even- and odd-mode field configurations in coupled microstrip lines.

The velocities of propagation of the even and odd modes are equal when the lines are embedded in a homogeneous dielectric medium (e.g., stripline). For transmission lines such as coupled microstrip lines, however, the dielectric medium is not homogeneous, and a part of the field extends into the air above the substrate, resulting in different propagation velocities for the two modes. Consequently, the effective dielectric constants (and the phase velocities) are different for the two modes. This nonsynchronous feature deteriorates the performance of circuits using these types of coupled lines. The voltage coupling coefficient of a coupling structure is generally expressed in terms of the even- and odd-mode characteristic impedances, effective dielectric constants, and coupled

structure line length. For a quarter-wave coupled section in a homogeneous dielectric medium, the coupling coefficient k is given by

$$k = \frac{Z_{0e} - Z_{0o}}{Z_{0e} + Z_{0o}} \qquad (2.10)$$

2.3 Microwave Network Analysis

Microwave network are essential building elements in many areas of RF/microwave engineering. Such networks are used to select/reject or separate/combine signals at different frequencies in a host of RF/microwave system and equipment. Microwave network theory was originally developed in the service of radar system and component development at the MIT Radiation Lab in the 1940s. In this section, the various microwave networks concepts and theory will be described for guiding the filters, power dividers or other passive devices design.

2.3.1 Equivalent Voltages and Currents

For low-frequency networks, one can define (and measure) unique voltages and currents at various locations in the circuit. Unfortunately, at microwave frequencies the measurement of voltage or current is difficult (or impossible), unless a clearly defined terminal pair is available. It is possible to define unique (actual) quantities only for transmission lines carrying power in the TEM mode. Examples of transmission lines supporting the TEM mode of propagation are a coaxial line, stripline, microstrip line, and so forth. Many other commonly used transmission lines such as hollow waveguides, dielectric guides, and fin lines do not support the TEM mode of propagation. Therefore, one resorts to the concept of equivalent voltages and currents, and this can be applied to both TEM- and non-TEM-mode transmission lines. Relationships involving equivalent voltages or currents lead to unique physical quantities such as reflection and transmission coefficients, normalized input impedance, and the like. Equivalent voltages and currents can be defined on a normalized or unnormalized basis. Because the representative matrix of a network may define a relationship between normalized or between unnormalized quantities, it is essential to understand their meaning.

(a)

(b)
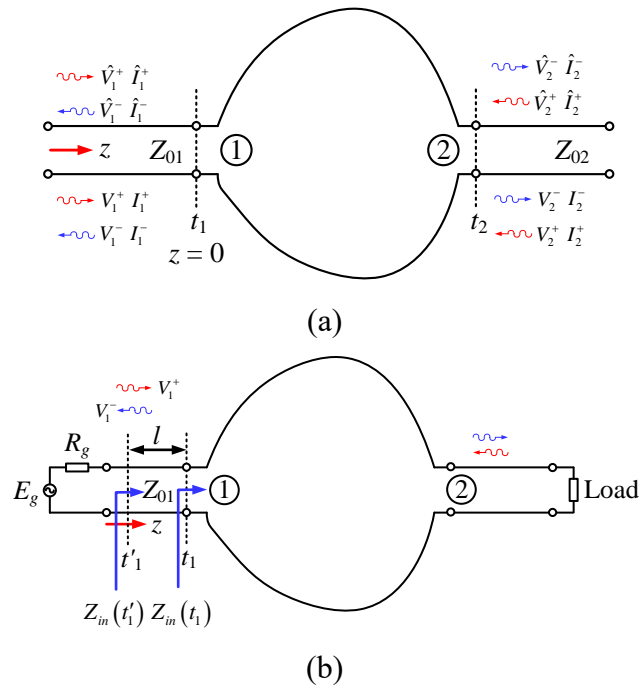
Fig. 2-5: (a) Normalized and unnormalized voltage and current waves on transmission lines of a two-port network. (b) A two-port network connected to a source and load.

Normalized Voltage and Currents: Fig. 2-5(a) shows a two-port network. The power flows into and out of the network by means of transmission lines connected to the network. Each transmission line may carry a wave propagating toward the network defined as the incident wave or away from the network defined as the reflected wave. If power is incident in the transmission line connected to port 1, the mode in which the power flows is a characteristic of the type of transmission line. Associated with a mode are unique electromagnetic fields. The transverse components of electric and magnetic fields (transverse to the direction of propagation) have a unique phase associated with them, which is the same for both fields. Further, the z-variation of the incident electromagnetic wave (assuming that the power flow is in the positive z-direction) can be described by a simple factor $e^{-j\beta_1 z}$, where β_1 is a unique quantity and denotes the phase constant of the wave in the transmission line of port 1.

To determine the normalized voltage and current waves, we assume that the incident voltage and current waves have the same phase as that of the transverse electric and magnetic field components of the incident electromagnetic wave. Further, the *z*-variation

of voltage and current waves is also given by the same factor as that for the field components ($e^{-j\beta 1z}$). Mathematically, the normalized incident voltage and current waves in the transmission line of port 1 can then be expressed as

$$\hat{V}_1^+(z) = \hat{V}_{10}^+ e^{-j\beta_1 z} = \left|\hat{V}_{10}^+\right| e^{j\psi_{i1}} e^{-j\beta_1 z} \tag{2.11}$$

$$\hat{I}_1^+(z) = \hat{I}_{10}^+ e^{-j\beta_1 z} = \left|\hat{I}_{10}^+\right| e^{j\psi_{i1}} e^{-j\beta_1 z} \tag{2.12}$$

When the characteristic impedance of a transmission line is real, the voltage and current waves can be expressed in terms of the incident and reflected power. At microwave frequencies, the characteristic impedances of practical transmission lines are generally real. To compute the values of $\left|\hat{V}_{10}^+\right|$ and $\left|\hat{I}_{10}^+\right|$, we force the condition that the average power flow is given by

$$\left|\hat{V}_{10}^+\right|\left|\hat{I}_{10}^+\right| = P_1^+ \tag{2.13}$$

To determine $\left|\hat{V}_{10}^+\right|$ and $\left|\hat{I}_{10}^+\right|$, we need to have another relation between them. To define normalized quantities, we choose

$$\frac{\left|\hat{V}_{10}^+\right|}{\left|\hat{I}_{10}^+\right|} = 1 \tag{2.14}$$

From (2.13) and (2.14), we can obtain

$$\left|\hat{V}_{10}^+\right| = \left|\hat{I}_{10}^+\right| = \sqrt{P_1^+} \tag{2.15}$$

Substituting the values of $\left|\hat{V}_{10}^+\right|$ and $\left|\hat{I}_{10}^+\right|$ from (2.15) in (2.11) and (2.12), we obtain

$$\hat{V}_1^+(z) = \hat{I}_1^+(z) = \sqrt{P_1^+} e^{j\psi_{i1}} e^{-j\beta_1 z} \tag{2.16}$$

With the same method, we can compute the reflected waves, which can be expressed as

$$\hat{V}_1^-(z) = \hat{I}_1^-(z) = \sqrt{P_1^-} e^{j\psi_{i1}} e^{j\beta_1 z} \tag{2.17}$$

Therefore, the total normalized voltage in the transmission line of port 1 is given by

$$\hat{V}_1(z) = \hat{V}_1^+(z) + \hat{V}_1^-(z)$$
$$= \left|\hat{V}_{10}^+\right| e^{j\psi_{i1}} e^{-j\beta_1 z} + \left|\hat{V}_{10}^-\right| e^{j\psi_{i1}} e^{j\beta_1 z} \qquad (2.18)$$
$$= \sqrt{P_1^+} e^{j\psi_{i1}} e^{-j\beta_1 z} + \sqrt{P_1^-} e^{j\psi_{i1}} e^{j\beta_1 z}$$

Moreover, the total current at any value of is z given by

$$\hat{I}_1(z) = \hat{I}_1^+(z) - \hat{I}_1^-(z)$$
$$= \left|\hat{I}_{10}^+\right| e^{j\psi_{i1}} e^{-j\beta_1 z} - \left|\hat{I}_{10}^-\right| e^{j\psi_{i1}} e^{j\beta_1 z} \qquad (2.19)$$
$$= \sqrt{P_1^+} e^{j\psi_{i1}} e^{-j\beta_1 z} - \sqrt{P_1^-} e^{j\psi_{i1}} e^{j\beta_1 z}$$

Reflection Coefficient and Input Impedance: Referring to Fig. 2-5(b), and substituting values of $\hat{V}_1^-(z)$ and $\hat{V}_1^+(z)$ from (2.16) and (2.17), the voltage reflection coefficient Γ_1 in the transmission line of port 1 is defined as

$$\Gamma_1 = \frac{\hat{V}_1^-(z)}{\hat{V}_1^+(z)} = \frac{V_1^-(z)}{V_1^+(z)}$$
$$= \frac{\left|\hat{V}_{10}^-\right| e^{j\psi_{1r} + j\beta_1 z}}{\left|\hat{V}_{10}^+\right| e^{j\psi_{1r} - j\beta_1 z}} = \sqrt{\frac{P_1^-}{P_1^+}} e^{j(\psi_{1r} - \psi_{1i})} e^{2j\beta_1 z} \qquad (2.20)$$

The reflection coefficient is a unique quantity, and the square of its modulus gives the fraction of the incident power that is reflected back from (2.20). The ratio of the reflected-to-incident power is commonly referred to as return loss. The return loss (in decibels), which is a positive quantity, is given by

$$RL(\text{dB}) = -10\lg\left|\Gamma_1(z)\right|^2 = -20\lg\left|\Gamma_1(z)\right| \qquad (2.21)$$

More often, it is the practice to use the ratio of total voltage and current, which can be termed as input impedance. The ratio of total normalized voltage to current is defined as the normalized input impedance and is given by

$$\hat{Z}_{in}(z) = \frac{\hat{V}_1(z)}{\hat{I}_1(z)} = \frac{\hat{V}_1^+(z) + \hat{V}_1^-(z)}{\hat{V}_1^+(z) - \hat{V}_1^-(z)} = \frac{1 + \Gamma_1(z)}{1 - \Gamma_1(z)} \qquad (2.22)$$

Similarly, the unnormalized input impedance Z_{in} is given by

$$Z_{in}(z) = Z_{01}\frac{1 + \Gamma_1(z)}{1 - \Gamma_1(z)} \qquad (2.23)$$

In Fig. 2-5(b), if $Z_{in}(t_1)$ denotes the loaded impedance Z_L, the input impedance Z_{in} at distance l away can be expressed as

$$Z_{in} = Z_{01} \frac{Z_L + jZ_{01} \tan \beta_1 l}{Z_{01} + jZ_L \tan \beta_1 l} \tag{2.24}$$

2.3.2 Impedance and Admittance Matrices
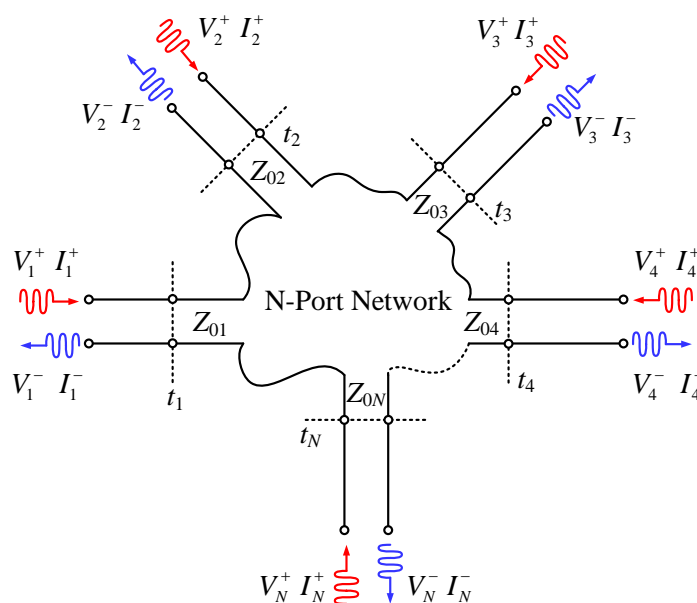
Fig. 2-6: An arbitrary N-port microwave network.

In the previous section, the equivalent voltages and currents and input impedance have been defined and analyzed. For microwave circuit's analysis, we will introduces the impedance and admittance matrices of N-port network, as depicted in Fig. 2-6. In the impedance matrix representation, the voltage at each port is related to the currents at the different ports as follows

$$\begin{aligned}
V_1 &= Z_{11}I_1 + Z_{12}I_2 + \cdots + Z_{1N}I_N \\
V_2 &= Z_{21}I_1 + Z_{22}I_2 + \cdots + Z_{2N}I_N \\
&\vdots \quad \vdots \quad \vdots \quad \quad \vdots \quad \vdots \quad \quad \quad \vdots \quad \vdots \\
V_N &= Z_{N1}I_1 + Z_{N2}I_2 + \cdots + Z_{NN}I_N
\end{aligned} \tag{2.25}$$

In matrix notation, this set of equations can be expressed as

$$[V] = [Z][I] \tag{2.26}$$

where

$$[V] = \begin{bmatrix} V_1 \\ \vdots \\ V_N \end{bmatrix} \quad (2.27)$$

$$[I] = \begin{bmatrix} I_1 \\ \vdots \\ I_N \end{bmatrix} \quad (2.28)$$

and

$$[Z] = \begin{bmatrix} Z_{11} & Z_{12} & \cdots & Z_{1N} \\ Z_{21} & Z_{22} & \cdots & Z_{2N} \\ \vdots & \vdots & \vdots & \vdots \\ Z_{N1} & Z_{N2} & \cdots & Z_{NN} \end{bmatrix} \quad (2.29)$$

In the admittance matrix representation, the current at each port of the network as shown in Fig. 2-6 is related to the voltages at the different ports as follows

$$[I] = [Y][V] \quad (2.30)$$

where $[V]$ and $[I]$ are column vectors as defined by (2.27) and (2.28), respectively, and

$$[Y] = \begin{bmatrix} Y_{11} & Y_{12} & \cdots & Y_{1N} \\ Y_{21} & Y_{22} & \cdots & Y_{2N} \\ \vdots & \vdots & \vdots & \vdots \\ Y_{N1} & Y_{N2} & \cdots & Y_{NN} \end{bmatrix} \quad (2.31)$$

2.3.3 The Scattering Matrix

As we all known that it is difficult to measure the voltages and currents at microwave frequencies directly. Thus, equivalent voltages and currents, and the related impedance and admittance matrices, become somewhat of an abstraction when dealing with high-frequency networks. A representation more in accord with direct measurements, and with the ideas of incident, reflected, and transmitted waves, is given by the scattering matrix. In this representation, the normalized reflected voltage at each port of the network as shown in Fig. 2-6 is related to the normalized incident voltages at the ports of the network as follows

$$\hat{V}_1^- = \hat{S}_{11}\hat{V}_1^+ + \hat{S}_{12}\hat{V}_2^+ + \cdots + \hat{S}_{1N}\hat{V}_N^+$$
$$\hat{V}_2^- = \hat{S}_{21}\hat{V}_1^+ + \hat{S}_{22}\hat{V}_2^+ + \cdots + \hat{S}_{2N}\hat{V}_N^+$$
$$\vdots \qquad \vdots \; \vdots \qquad \vdots \; \vdots \qquad \qquad \vdots \; \vdots$$
$$\hat{V}_N^- = \hat{S}_{N1}\hat{V}_1^+ + \hat{S}_{N2}\hat{V}_2^+ + \cdots + \hat{S}_{NN}\hat{V}_N^+$$

(2.32)

In matrix notation, the above set of equations can be expressed as

$$\left[\hat{\boldsymbol{V}}^-\right] = \left[\hat{\boldsymbol{S}}\right]\left[\hat{\boldsymbol{V}}^+\right]$$

(2.33)

where

$$\left[\hat{\boldsymbol{V}}^-\right] = \begin{bmatrix} \hat{V}_1^- \\ \vdots \\ \hat{V}_N^- \end{bmatrix}$$

(2.34)

$$\left[\hat{\boldsymbol{V}}^+\right] = \begin{bmatrix} \hat{V}_1^+ \\ \vdots \\ \hat{V}_N^+ \end{bmatrix}$$

(2.35)

and

$$\left[\hat{\boldsymbol{S}}\right] = \begin{bmatrix} \hat{S}_{11} & \hat{S}_{12} & \cdots & \hat{S}_{1N} \\ \hat{S}_{21} & \hat{S}_{22} & \cdots & \hat{S}_{2N} \\ \vdots & \vdots & \vdots & \vdots \\ \hat{S}_{N1} & \hat{S}_{N2} & \cdots & \hat{S}_{NN} \end{bmatrix}$$

(2.36)

The scattering parameter $\hat{S}_{mn}$ is therefore given by

$$\hat{S}_{mn} = \frac{\hat{V}_m^-}{\hat{V}_n^+}\Bigg|_{\hat{V}_p^+ = 0 \text{ where } p=1,\ldots,N; p \neq n}$$

(2.37)

2.3.4 The Transmission Matrix

The *Z*, *Y*, and *S* parameter representations can be used to characterize a microwave network with an arbitrary number of ports, but in practice many microwave networks consist of a cascade connection of two or more two-port networks. In this case it is convenient to define a 2 × 2 transmission (or ABCD) matrix, for each two-port network. We will see that the ABCD matrix of the cascade connection of two or more two-port

networks can be easily found by multiplying the ABCD matrices of the individual two-ports.

The ABCD matrix is defined for a two-port network in terms of the total voltages and currents as shown in Fig. 2-7(a) and the following:

$$V_1 = AV_2 + BI_2$$
$$I_1 = CV_2 + DI_2$$

(2.38)

or in matric form as

$$\begin{bmatrix} V_1 \\ I_1 \end{bmatrix} = \begin{bmatrix} A & B \\ C & D \end{bmatrix} \begin{bmatrix} V_2 \\ I_2 \end{bmatrix}$$

(2.39)

(a)

(b)
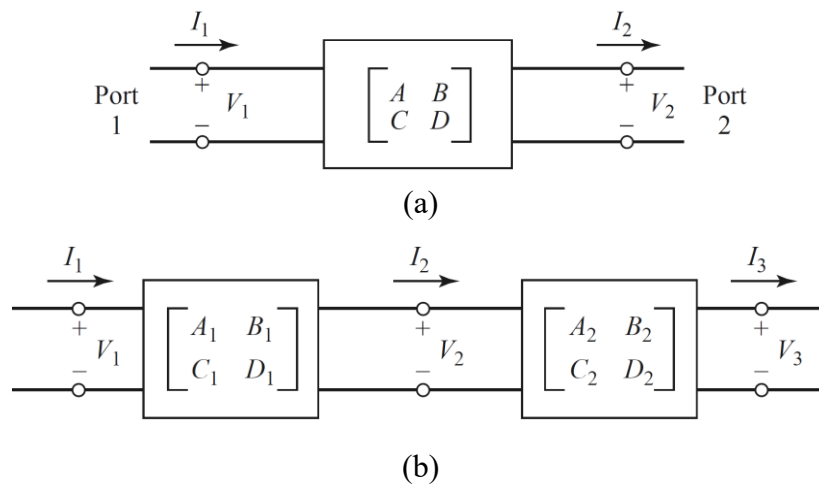
Fig. 2-7: (a) A two-port network; (b) a cascade connection of tow-port networks.

It is important to note from Fig. 2-7(a) that a change in the sign convention of I_2 has been made from our previous definitions, which had I_2 as the current flowing into port 2. The convention that I_2 flows out of port 2 will be used when dealing with ABCD matrices so that in a cascade network I_2 will be the same current that flows into the adjacent network, as shown in Fig. 2-7(b). Then the left-hand side of (2.39) represents the voltage and current at port 1 of the network, while the column on the right-hand side of (2.39) represents the voltage and current at port 2.

In the cascade connection of two two-port networks shown in Fig. 2-7(b) we have that

$$\begin{bmatrix} V_1 \\ I_1 \end{bmatrix} = \begin{bmatrix} A_1 & B_1 \\ C_1 & D_1 \end{bmatrix} \begin{bmatrix} V_2 \\ I_2 \end{bmatrix}$$
$$\begin{bmatrix} V_2 \\ I_2 \end{bmatrix} = \begin{bmatrix} A_2 & B_2 \\ C_2 & D_2 \end{bmatrix} \begin{bmatrix} V_3 \\ I_3 \end{bmatrix}$$

(2.40)

Simplify the (2.40), the follow equation can be obtain

$$\begin{bmatrix} V_1 \\ I_1 \end{bmatrix} = \begin{bmatrix} A_1 & B_1 \\ C_1 & D_1 \end{bmatrix} \begin{bmatrix} A_2 & B_2 \\ C_2 & D_2 \end{bmatrix} \begin{bmatrix} V_3 \\ I_3 \end{bmatrix}$$

(2.41)

(2.41) shows that the ABCD matrix of the cascade connection of the two networks is equal to the product of the ABCD matrices representing the individual two-ports. Note that the order of multiplication of the matrix must be the same as the order in which the networks are arranged since matrix multiplication is not, in general, commutative. Some number of two-port networks and their ABCD matrices had been list in [3].

2.4 Basic Properties and Theory of Power Dividers

Power divider is three-port passive microwave component used to power division or power combining, as illustrated in Fig. 2-8. In Fig. 2-8, an input signal is divided into two output signals of lesser power, while a power combiner accepts two or more input signals and combines them at an output port. Power dividers usually provide in-phase output signals with an equal power division ratio (3 dB), but unequal power division ratios are also possible. In the next part, we will introduce the three-port network and Wilkinson power divider.
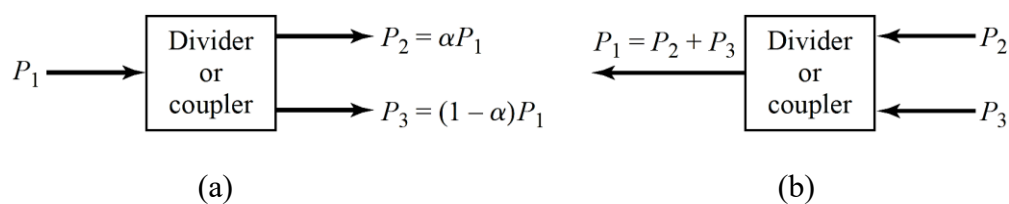

Fig. 2-8: Power division and combing. (a) Power division. (b) Power combining.

2.4.1 Three-Port Network

The simplest type of power divider is a T-junction, which is a three-port network with two inputs and one output. The scattering matrix of an arbitrary three-port network

has nine independent elements

$$[S] = \begin{bmatrix} S_{11} & S_{12} & S_{13} \\ S_{21} & S_{22} & S_{23} \\ S_{31} & S_{32} & S_{33} \end{bmatrix} \tag{2.42}$$

If the device is passive and contains no anisotropic materials, then it must be reciprocal and its scattering matrix will be symmetric ($S_{ij} = S_{ji}$). Usually, to avoid power loss, we would like to have a junction that is lossless and matched at all ports. We can easily show, however, that it is impossible to construct such a three-port lossless reciprocal network that is matched at all ports. If all ports are matched, then $S_{ii} = 0$, and if the network is reciprocal, the scattering matrix of (2.42) reduces to

$$[S] = \begin{bmatrix} 0 & S_{12} & S_{13} \\ S_{21} & 0 & S_{23} \\ S_{31} & S_{32} & 0 \end{bmatrix} \tag{2.43}$$

If the network is also lossless, then energy conservation requires that the scattering matrix satisfy the unitary properties of (4.39), which leads to the following conditions

$$|S_{12}|^2 + |S_{13}|^2 = 1 \tag{2.44a}$$

$$|S_{12}|^2 + |S_{23}|^2 = 1 \tag{2.44b}$$

$$|S_{13}|^2 + |S_{23}|^2 = 1 \tag{2.44c}$$

$$S_{13}^* S_{23} = 0 \tag{2.44d}$$

$$S_{23}^* S_{12} = 0 \tag{2.44e}$$

$$S_{12}^* S_{13} = 0 \tag{2.44f}$$

Equations (2.44d)–(2.44f) show that at least two of the three parameters (S_{12}, S_{13}, S_{23}) must be zero. However, this condition will always be inconsistent with one of equations (2.44a)–(2.44c), implying that a three-port network cannot be simultaneously lossless, reciprocal, and matched at all ports. If any one of these three conditions is relaxed, then a physically realizable device is possible.

If the three-port network is nonreciprocal, then $S_{ij} \neq S_{ji}$, and the conditions of input matching at all ports and energy conservation can be satisfied. The scattering matrix of a matched three-port network has the following form

$$[S] = \begin{bmatrix} 0 & S_{12} & S_{13} \\ S_{21} & 0 & S_{23} \\ S_{31} & S_{32} & 0 \end{bmatrix} \qquad (2.45)$$

If the network is lossless, [S] must be unitary, which implies the following conditions

$$S_{31}^* S_{32} = 0 \qquad (2.46a)$$

$$S_{21}^* S_{23} = 0 \qquad (2.46b)$$

$$S_{12}^* S_{13} = 0 \qquad (2.46c)$$

$$|S_{12}|^2 + |S_{13}|^2 = 1 \qquad (2.46d)$$

$$|S_{21}|^2 + |S_{23}|^2 = 1 \qquad (2.46e)$$

$$|S_{31}|^2 + |S_{32}|^2 = 1 \qquad (2.46f)$$

2.4.2 The Wilkinson Power Divider

Wilkinson power divider have good isolation between two outputs and better matched at all ports are widely researched, which is proposed by Ernest J. Wilkinson in 1959. Wilkinson power divider is a lossy, reciprocal and matched three-port network, which also called resistive divider. The Wilkinson power divider can be made with arbitrary power division, but we will first consider the equal-split (3 dB) case. This divider is often made in microstrip line or stripline form, as depicted in Fig. 2-9(a), and the corresponding transmission line circuit is given in Fig. 2-9(b). We will analyze this circuit by reducing it to two simpler circuits driven by symmetric and antisymmetric sources at the output ports. This even- and odd-mode analysis technique will also be useful for other networks that we will study in later sections [3][4].
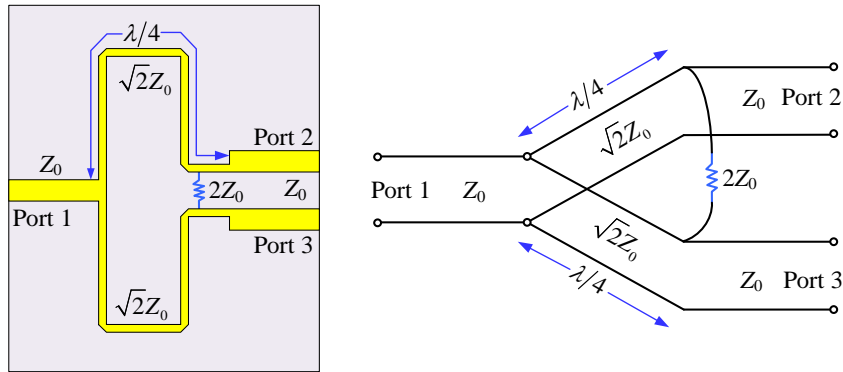
Fig. 2-9: The Wilkinson power divider. (a) An equal-split Wilkinson power divider in microstrip line form. (b) Equivalent transmission line circuit.

Even- and Odd-Mode Analysis: For simplicity, all of impedances can be normalized by the characteristic impedance Z_0, and redraw the circuit of Fig. 2-9(b) with voltage generators at the output ports as shown in Fig. 2-10. Now define two separate modes of excitation for the circuit of Fig. 2-10: the even mode, where $V_{g2} = V_{g3} = 2V_0$, and the odd mode, where $V_{g2} = -V_{g3} = 2V_0$. Superposition of these two modes effectively produces an excitation of $V_{g2} = 4V_0$ and $V_{g3} = 0$, from which we can find the scattering parameters of the network.
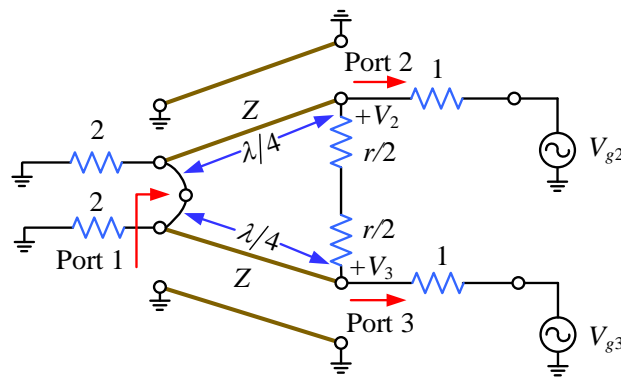
Fig. 2-10: The Wilkinson power divider circuit in normalized and symmetric form.

(a)

(b)
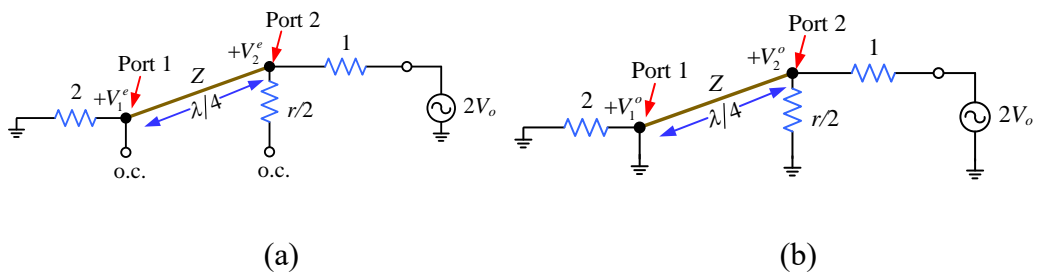
Fig. 2-11: Bisection of the WPD (a) Even-mode excitation. (b) Odd-mode excitation

Even-Mode Analysis: Under the even-mode excitation, $V_{g2} = V_{g3} = 2V_0$, so $V_2^e = V_3^e$, and therefore no current flows through the $r/2$ resistors or the short circuit between the inputs of the two transmission lines at port 1.The even-mode equivalent circuit is illustrated in Fig.2-11(a). Then, looking into port 2, we see an input impedance

$$Z_{in}^e = \frac{Z^2}{2} \tag{2.47}$$

Odd-Mode Analysis: Under the odd-mode excitation, $V_{g2} = -V_{g3} = 2V_0$, so $V_2^o = -V_3^o$, and there is voltage null along the middle of the circuit in Fig. 2-10. Therefore, the odd-mode equivalent circuit is depicted in Fig. 2-11(b). Looking into port 2, we see an impedance of $r/2$ since the parallel-connected transmission line is $\lambda/4$ long and shorted at port 1, and so looks like an open circuit at port 2. Under the odd-mode excitation, all power is delivered to the $r/2$ resistors, with none going to port 1. Therefore, the input impedance can be derived as

$$Z_{in}^e = \frac{Z^2}{2} = \frac{\left(\sqrt{2}\right)^2}{2} = 1 \tag{2.48}$$

Finally, the total circuit model of the Wilkinson power divider can be establish and their scattering parameters can be obtained according the three-port network, which introduced in the above section.

$$
\begin{aligned}
S_{11} &= 0 \\
S_{22} &= S_{33} = 0 \\
S_{12} &= S_{21} = \frac{V_1^e + V_1^o}{V_2^e + V_2^o} = -j/\sqrt{2} \\
S_{13} &= S_{31} = -j/\sqrt{2} \\
S_{23} &= S_{32} = 0
\end{aligned}
\tag{2.49}
$$

2.5 Differential Circuit and Mixed-Mode S-Parameters

Differential circuits act as an important role in modern communication system [4][5]. Analog signals processed by a communication system are degraded by two different types of noises, namely, the environmental noise and device electronic noise. The differential circuits can help reject the common-mode noise (the environmental noise and device

electronic noise). In a differential circuit, signals with equal magnitude and opposite phase relative to reference ground potential are transmitted and processed across a matched two-conductor system. In ideal differential circuit, the ground or DC supply path is not the path for the signal currents or the signal ground return currents to travel to the signal source. The reference ground terminal is ideally at a constant mid-potential level between the voltage potential associated with the differential input signal. A two-port differential network with four terminals is illustrated in Fig. 2-12. It shows that the differential signal can be transmitted by this differential networks perfectly, and all the common-mode (CM) signals introduced through the ground reference nodes are eliminated. Therefore, the ideal differential or balanced system have a good suppression of CM noise compare with the traditional single-ended system. In this section, we will introduce the definition of the nixed-mode and mixed-mode scattering parameters of the differential circuit.
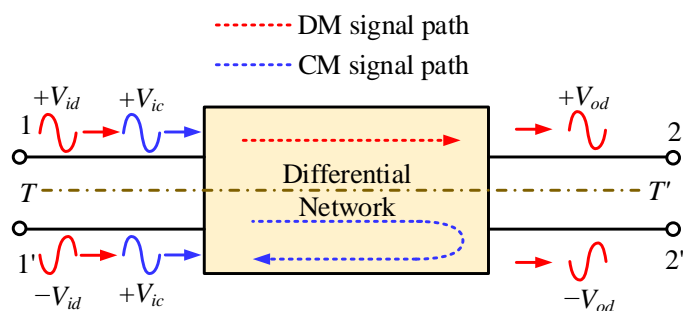
Fig. 2-12: A two-port differential network with four terminals.

2.5.1 Mixed-Mode Scattering Parameter

According to the single-ended S-parameters theory, as an example of four-port network in Fig. 2-12, the expanding the single-ended $[\boldsymbol{S}]$ matrix into standard input/output algebraic relations results in

$$\begin{aligned}
b_1 &= S_{11}a_1 + S_{12}a_2 + S_{13}a_3 + S_{14}a_4 \\
b_2 &= S_{21}a_1 + S_{22}a_2 + S_{23}a_3 + S_{24}a_4 \\
b_3 &= S_{31}a_1 + S_{32}a_2 + S_{33}a_3 + S_{34}a_4 \\
b_4 &= S_{41}a_1 + S_{42}a_2 + S_{43}a_3 + S_{44}a_4
\end{aligned} \tag{2.50}$$

The individual S-parameter matric elements are calculated numerically in a simulator or measured by test equipment under the following conditions

$$S_{xy} = \left. \frac{b_x}{a_y} \right|_{a(x \neq y)=0} \tag{2.51}$$

In (2.51), all the a power-wave sources are turned off except a_y and then the b_x power wave is characterized. In S_{11} measurement, the a_1 power wave source is applied and the b_1 reflection from the circuit is measured as below

$$S_{11} = \left. \frac{b_1}{a_1} \right|_{a_2, a_3, \dots = 0} \tag{2.52}$$

Therefore, the same relationships can be applied to normalized mixed-mode power waves to develop the mixed-mode S-parameters

$$
\begin{aligned}
b_{d1} &= S_{dd11}a_{d1} + S_{dd12}a_{d2} + S_{dc11}a_{c1} + S_{dc12}a_{c2} \\
b_{d2} &= S_{dd21}a_{d1} + S_{dd22}a_{d2} + S_{dc21}a_{c1} + S_{dc22}a_{c2} \\
b_{c1} &= S_{cd11}a_{d1} + S_{cd12}a_{d2} + S_{cc11}a_{c1} + S_{cc12}a_{c2} \\
b_{c2} &= S_{cd21}a_{d1} + S_{cd22}a_{d2} + S_{cc21}a_{c1} + S_{cc22}a_{c2}
\end{aligned}
\tag{2.53}
$$

2.5.2 Standard S-Parameter and Mixed-Mode S-Parameter Transformation

In the design of differential, the standard S-parameter matrix cannot used to design directly. Therefore, it should be transfer to mixed-mode S-parameter matrix form. The ideal standard matrix (S_{std}) of the four ports reciprocal network exhibited in Fig. 2-12, can be defined as

$$
S_{std} = \begin{bmatrix}
S_{11} & S_{13} & S_{12} & S_{14} \\
S_{31} & S_{33} & S_{32} & S_{34} \\
S_{21} & S_{23} & S_{22} & S_{24} \\
S_{41} & S_{43} & S_{42} & S_{44}
\end{bmatrix}
\tag{2.54}
$$

The mixed-mode scattering matrix (S_{mm}) of the proposed balanced-to-unbalanced filtering power divider can be derived from the standard matrix (S_{std}) using the matrix transformation as bellow [5]

$$S_{mm} = M S_{std} M^{-1} \tag{2.55a}$$

where

$$M = \frac{1}{\sqrt{2}} \begin{bmatrix} 1 & -1 & 0 & 0 \\ 1 & 1 & 0 & 0 \\ 0 & 0 & \sqrt{2} & 0 \\ 0 & 0 & 0 & \sqrt{2} \end{bmatrix} \tag{2.55b}$$

Combining (2.54) and (2.55), the mixed-mode scattering matrix (S_{mm}) can be derived as

$$S_{mm} = \begin{bmatrix} S_{dd11} & S_{ds13} & S_{dc11} & S_{ds14} \\ S_{sd31} & S_{ss33} & S_{sc31} & S_{ss34} \\ S_{cd11} & S_{cs13} & S_{cc11} & S_{cs14} \\ S_{sd41} & S_{ss43} & S_{sc41} & S_{ss44} \end{bmatrix} \tag{2.56}$$

$$S_{dd} = \frac{1}{2} \begin{bmatrix} S_{dd11} = \left(S_{A^{(+)}A^{(+)}} - S_{A^{(+)}3} - S_{3A^{(+)}} + S_{33} \right) & S_{dd12} = \left(S_{A^{(+)}A^{(-)}} - S_{A^{(+)}4} - S_{3A^{(-)}} + S_{34} \right) \\ S_{dd21} = \left(S_{A^{(-)}A^{(+)}} - S_{A^{(-)}3} - S_{4A^{(+)}} + S_{43} \right) & S_{dd22} = \left(S_{A^{(-)}A^{(-)}} - S_{A^{(-)}4} - S_{4A^{(-)}} + S_{44} \right) \end{bmatrix} \tag{2.57a}$$

$$S_{dc} = \frac{1}{2} \begin{bmatrix} S_{dc11} = \left(S_{A^{(+)}A^{(+)}} + S_{A^{(+)}3} - S_{3A^{(+)}} - S_{33} \right) & S_{dc12} = \left(S_{A^{(+)}A^{(-)}} + S_{A^{(+)}4} - S_{3A^{(-)}} - S_{34} \right) \\ S_{dc21} = \left(S_{A^{(-)}A^{(+)}} + S_{A^{(-)}3} - S_{4A^{(+)}} - S_{43} \right) & S_{dc22} = \left(S_{A^{(-)}A^{(-)}} + S_{A^{(-)}4} - S_{4A^{(-)}} - S_{44} \right) \end{bmatrix} \tag{2.57b}$$

$$S_{cd} = \frac{1}{2} \begin{bmatrix} S_{cd11} = \left(S_{A^{(+)}A^{(+)}} - S_{A^{(+)}3} + S_{3A^{(+)}} - S_{33} \right) & S_{cd12} = \left(S_{A^{(+)}A^{(-)}} - S_{A^{(+)}4} + S_{3A^{(-)}} - S_{34} \right) \\ S_{cd21} = \left(S_{A^{(-)}A^{(+)}} - S_{A^{(-)}3} + S_{4A^{(+)}} - S_{43} \right) & S_{cd22} = \left(S_{A^{(-)}A^{(-)}} - S_{A^{(-)}4} + S_{4A^{(-)}} - S_{44} \right) \end{bmatrix} \tag{2.57c}$$

$$S_{cc} = \frac{1}{2} \begin{bmatrix} S_{cc11} = \left(S_{A^{(+)}A^{(+)}} + S_{A^{(+)}3} + S_{3A^{(+)}} + S_{33} \right) & S_{cc12} = \left(S_{A^{(+)}A^{(-)}} + S_{A^{(+)}4} + S_{3A^{(-)}} + S_{34} \right) \\ S_{cc21} = \left(S_{A^{(-)}A^{(+)}} + S_{A^{(-)}3} + S_{4A^{(+)}} + S_{43} \right) & S_{cc22} = \left(S_{A^{(-)}A^{(-)}} + S_{A^{(-)}4} + S_{4A^{(-)}} + S_{44} \right) \end{bmatrix} \tag{2.57d}$$

2.6 Conclusion

In this chapter, we introduces the basic theory of the filter, power divider, and differential circuit, systematically, which includes the general definition of filter, design procedure of the filter with the lowpass prototype, microwave network, classical power divider analysis methods and mixed-mode S-parameters. All of the description of the basic theory are summarized from other published literatures, as list in reference section. By this summarization, readers can easy understand the mechanism of design works will be introduced in the next chapters.

References

[1] J. S. Hong, and M. J. Lancaster, *Microwave Filter for RF/Microwave Application*. New York, USA: Wiley, 2001.

[2] R. K. Mongia, I. J. Bahl, P. Bhartia, and J. Hong, *RF and Microwave Coupled-line Circuits (2nd)*. Boston, Landon, Artech House, 2007.

[3] D. M. Pozar, *Microwave Engineering (4th)*, New York, USA: Wiley, 2011.

[4] J. Reed, and G. J. Wheeler, "A method of analysis of symmetrical four-port networks," *IEEE Trans. Microw. Theory Techn.*, vol. MTT-4, pp. 246-252, Oct. 1956.

[5] W. R. Eisenstadt, B. Stengel, and B. M. Thompson, *Microwave Differential Circuit Design Using Mixed-Mode S-Parameters*. Boston, Landon, Artech House, 2006.

Chapter 3

Multi-Band Bandpass Filters Using Multi-Mode Resonators

3.1 Overview

From the above two chapters, it is known that the multi-band bandpass filter (BPFs) plays an important role in modern wireless communication systems for their compact size and multi-services, which results in low loss, high integration, and low cost. With the development of compact and intelligent wireless communication terminal devices, multiband RF/microwave components are attracting great attention of many researchers. In section 1.2, we introduced many multi-band BPF design approaches, where multiple mode resonator (MMR) is the most popular method to realize low insertion loss, wide bandwidth, and especially compact size.

In this Chapter, we will propose two type of MMR to design a serial of multiband BPFs. One is the stub-loaded stepped impedance resonator (SL-SIR), which has flexible resonant modes and controllable resonance frequencies. The other is a dual-resonance resonator (also called H-shaped resonator), which have two resonance modes and two potential transmission zeros. In this chapter, we will describe and analyze the resonance characteristics of the two type resonators, respectively.

3.2 Analysis of the Two-Types of Dual-Mode Resonators (DMRs)

3.2.1 Stub-Laded Dual-Mode Resonator (SL-DMR)

The stub-loaded stepped impedance resonator (SL-SIR) has the ability to control the first, second, and third resonant frequencies. Fig. 3-1(a) shows the transmission line model of the proposed SL-SIR, where Z_i ($i = 1, 2, t, s1, s2$) and θ_i ($i = 1, 2, t, s1, s2$) represent the characteristic impedance and electrical length, respectively. The SL-SIR has an open stub with Z_1 and θ_1 at its one end, and a short-circuited stub with Z_t and θ_t at the other end, together with a loaded structure indicated by Z_S. In this study, two cases of the

loaded structure are considered:

Case 1: the loaded structure is one open stub with (Z_{s1}, θ_{s1}), as shown by Fig. 3-1(b).

Case 2: the loaded structure consists of two shunt open stubs with (Z_{s1}, θ_{s1}) and (Z_{s2}, θ_{s2}), respectively, as shown in Fig. 3-1(c).
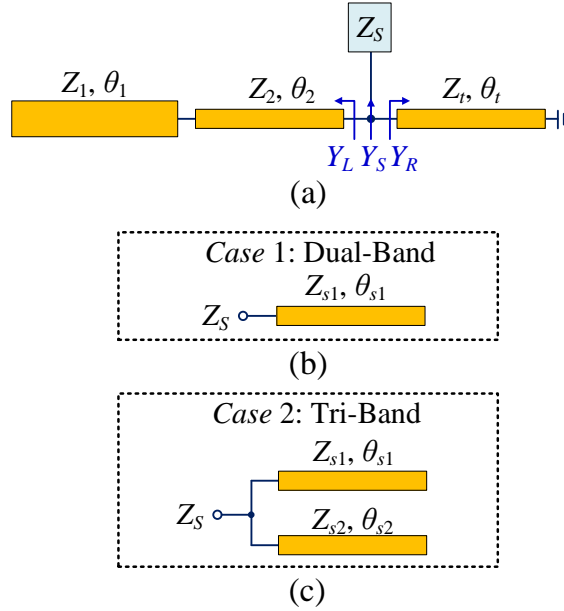
Fig. 3-1: (a) Transmission line model of the proposed stubs loaded stepped impedance resonator (SL-SIR); (b) Dual-band case; (c) Tri-band case.

The input admittance seen from the location of the stubs loaded is

$$Y_{in} = Y_L + Y_S + Y_R \tag{3.1}$$

where

$$Y_L = j \frac{Z_2 + Z_1 \cot \theta_1 \tan \theta_2}{Z_2 \left(Z_1 \cot \theta_1 - Z_2 \tan \theta_2 \right)} \tag{3.2}$$

$$Y_R = -j \frac{\cot \theta_t}{Z_t} \tag{3.3}$$

$$Y_S = \begin{cases} j \dfrac{\tan \theta_{s1}}{Z_{s1}}, & \text{(dual-band case)} \\[3mm] j \left(\dfrac{\tan \theta_{s1}}{Z_{s1}} + \dfrac{\tan \theta_{s2}}{Z_{s2}} \right), & \text{(tri-band case)} \end{cases} \tag{3.4}$$
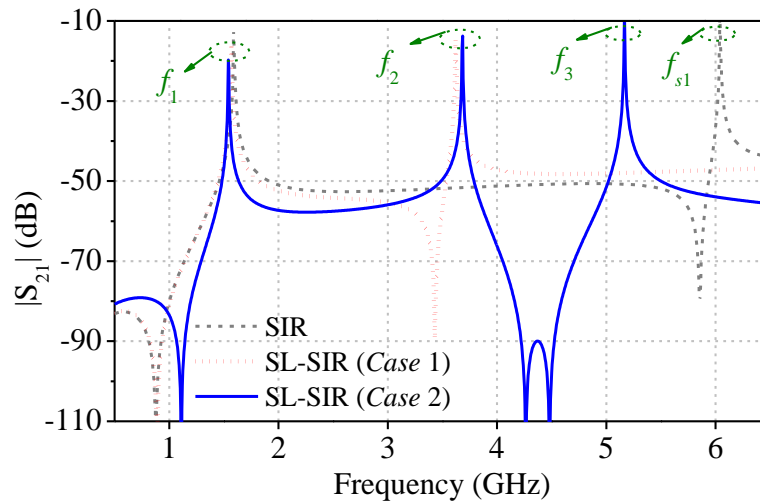
Fig. 3-2: Simulated $|S_{21}|$ of (a) Traditional SIR; (b) Case 1; (c) Case 2.

For simplicity, we assume that $Z_2 = Z_t = Z_{s1} = Z_{s2}$, and $R_z = Z_2/Z_1$. The resonant mode can be obtained by $Y_{in} = 0$. As shown in Fig. 3-1(b) and (c), at the different loaded cases, it will obtain single-resonance, dual-resonance (*Case* 1) and triple-resonance (*Case* 2) characteristics. The simulated response S_{21} of the proposed SL-SIR under week coupling is given in Fig. 3-2, from which, it is clearly seen that in case 1, the proposed SL-SIR behaves as a dual-mode resonator, while in case 2, it performs as a tri-mode resonator. This phenomenon can be easy verified in Fig. 3-3. For the tri-mode SL-SIR, which consists of one shorted-circuited stub and three open stubs, Fig. 3-3(a)-(c) provide the current distribution on the microstrip lines at resonance, f_1, f_2, and f_3, respectively. It is seen from Fig. 3-3(a) that the resonance at f_1 is occurred at path I as a $\lambda/4$ SIR, which includes lines with electrical lengths θ_1, θ_2, and θ_t. The resonance at f_2, as shown in Fig. 3-3(b), is happed at path II as a $\lambda/2$ SIR, which consists of lines with electrical lengths θ_1, θ_2, and θ_{s1}. The resonance at f_3, as shown in Fig. 3-3(c), involves all the four stubs. Therefore, with appropriate choosing of the line lengths of the stubs, it is easy to design these three resonances at desired frequencies.

Fig. 3-3: Surface current distribution of the proposed tri-mode SL-SIR (a) Current distribution at the first resonance (Path I); (b) Current distribution at the second resonance (Path II); (c) Current distribution at the third resonance (Path III).

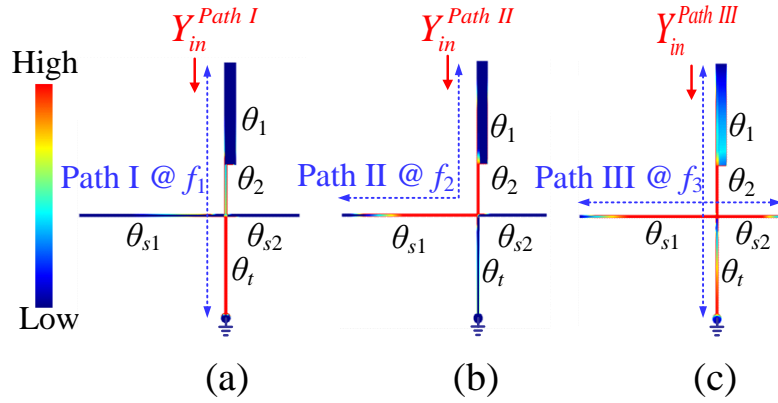From (3.1) - (3.4), we can see that the input admittance formula Y_{in} is extremely complex. Accordingly, with the verdict in Fig. 3-3, we can divide the input admittance Y_{in} into three parts $Y_{in}^{Path\ I}$, $Y_{in}^{Path\ II}$, and $Y_{in}^{Path\ III}$ as follows:

$$Y_{in}^{Path\ I} = j\frac{R_z \tan\theta_1 \tan(\theta_2 + \theta_t) - 1}{Z_1\left[\tan\theta_1 + R_z \tan(\theta_2 + \theta_t)\right]} \tag{3.5}$$

$$Y_{in}^{Path\ II} = j\frac{1 + R_z \tan\theta_1 \cot(\theta_2 + \theta_{s1})}{Z_1\left[R_z \cot(\theta_2 + \theta_{s1}) - \tan\theta_1\right]} \tag{3.6}$$

$$\begin{aligned}
Y_{in}^{Path\ III} &= Y_L + Y_R + Y_S \\
&= j\frac{R_z + R_z \tan\theta_2 (\cot\theta_t - \tan\theta_{s1} - \tan\theta_{s2})}{R_z Z_1 (\cot\theta_1 - R_z \tan\theta_2)} \\
&\quad + j\frac{\cot\theta_1 (\tan\theta_2 - \cot\theta_t + \tan\theta_{s1} + \tan\theta_{s2})}{R_z Z_1 (\cot\theta_1 - R_z \tan\theta_2)}
\end{aligned} \tag{3.7}$$

Therefore, the fundamental frequency f_1 and the first spurious frequency f_2 of the proposed SL-SIR are determined by the first roots of the following formulas:

$$R_z \tan\theta_1 \tan(\theta_2 + \theta_t) - 1 = 0, \qquad\qquad \text{for } f_1 \tag{3.8}$$

$$1 + R_z \tan\theta_1 \cot(\theta_2 + \theta_{s1}) = 0, \qquad\qquad \text{for } f_2 \tag{3.9}$$

$$\begin{aligned}
&R_z + R_z \tan\theta_2 (\cot\theta_t - \tan\theta_{s1} - \tan\theta_{s2}) \\
&\quad + \cot\theta_1 (\tan\theta_2 - \cot\theta_t + \tan\theta_{s1} + \tan\theta_{s2}) = 0
\end{aligned}, \qquad \text{for } f_3 \tag{3.10}$$

From the formulas (3.8) and (3.9), it can be seen that the frequency f_1 and f_2 can be

controlled by the impedance ratio R_z and electric length θ_1 and θ_2, and then the electric length θ_{s1} independent control the frequency f_2. According to the design requirement of frequency $f_1 = 1.57$ GHz, and $f_2 = 3.6$ GHz, we can determine the impedance ratio R_z, electric length θ_1, θ_2 and θ_{s1}. Thus, with those various, the relationship between electric length θ_{s2} and f_3 from equation (3.10). In a word, for the multi-band BPF design, we should be make the resonator operated at the needed frequency f_1 for the first passband by controlling the impedance ratio R_z and electric length θ_1 and θ_2, firstly. Then, to design the second frequency f_2 by changing the electric length θ_{s1}. Finally, it can be design suitable electric length to meet the requirement resonant frequency f_3.

3.2.2 Dual-Resonance Resonator (DRR)
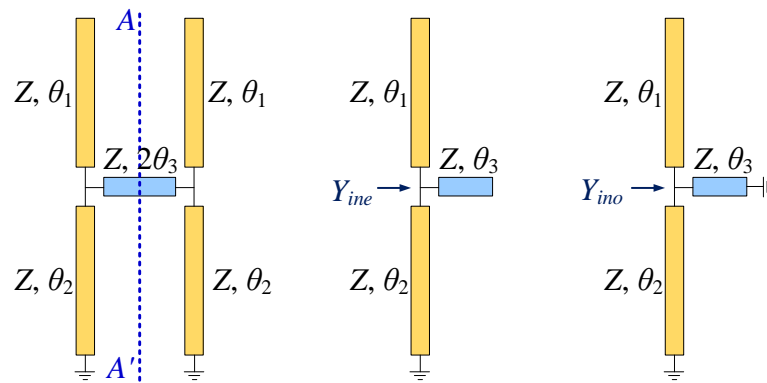
Fig. 3-4: (a) Transmission line model of the proposed dual-resonance resonator; (b) Even-mode equivalent circuit; (c) Odd-mode equivalent circuit.

Fig. 3-4(a) depicts the transmission line mode of the proposed dual-resonance resonator (DRR). It consists of two short-circuited microstrip lines and a short transversal connecting line. The characteristic impedances of these lines are all the same, and are indicated by Z. The electrical lengths of these lines are indicated by θ_1, θ_2 and $2\theta_3$, respectively. Since the resonator is a symmetrical structure, the even- and odd-mode method is good candidate for analyzing the proposed resonator. Under the even-/odd-mode excitation, the symmetrical plane AA' behaves as a perfect magnetic wall or electric wall, respectively, and the even-/odd-mode equivalent circuit of the resonator are shown in Fig. 3-4(b) and Fig. 3-4(c), respectively. As illustrated in Fig. 3-4(b), Y_{ine} represent the input admittance under the even-mode excitation and is given by
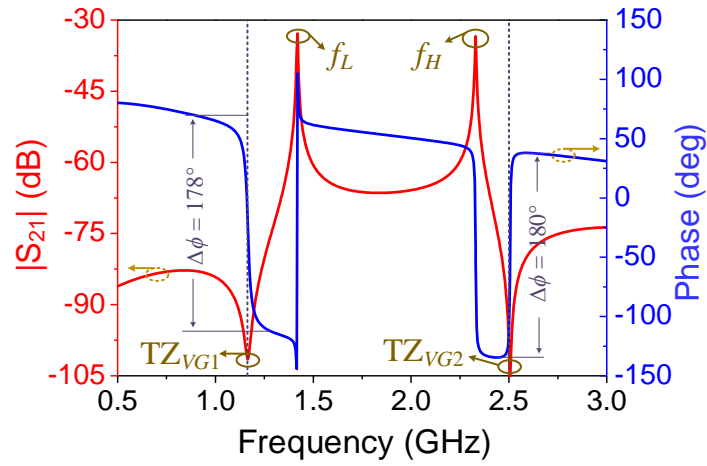
(a)
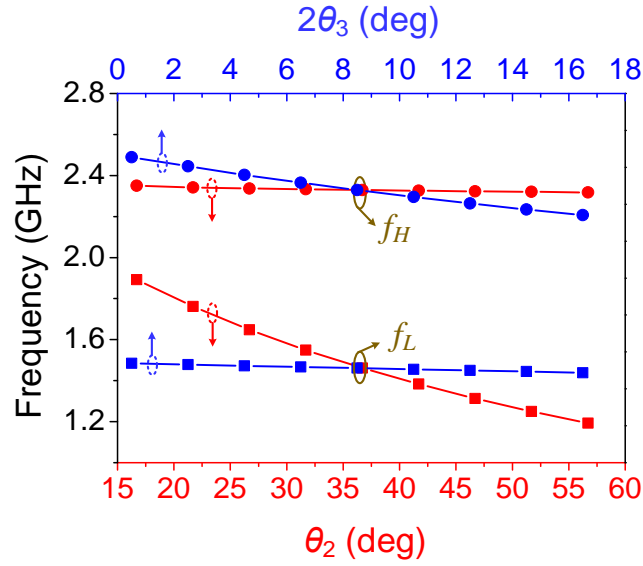
(b)

Fig. 3-5: (a) Simulated amplitude and phase of S_{21}, and (b) Variation of the even- and odd-mode resonant frequencies with θ_2 and $2\theta_3$.

$$Y_{ine} = jY_0 \left(\tan\theta_1 - \cot\theta_2 + \tan\theta_3 \right) \tag{3.11}$$

At resonance, the input admittance $Y_{ine} = 0$, thus the resonant condition is derived as

$$\tan\theta_1 - \cot\theta_2 + \tan\theta_3 = 0 \tag{3.12}$$

Similarly, under the odd-mode excitation, the Y_{ino} is express as

$$Y_{ino} = jY_0 \left(\tan\theta_1 - \cot\theta_2 - \cot\theta_3 \right) \tag{3.13}$$

and the resonant condition is derived as

$$\tan \theta_1 - \cot \theta_2 - \cot \theta_3 = 0 \tag{3.14}$$

Therefore, the resonant frequencies at the even-mode (f_{even}) and odd-mode (f_{odd}) can be calculated by solving (3.12) and (3.14). It can be seen from (3.12) that when θ_1 is fixed and θ_3 is very small compare with θ_2, θ_3 will has little effect on the even-mode frequency f_{even}. Under the same constraint, it can be seen from (3.14) that θ_2 has less influence on the odd-mode frequency f_{odd}. Therefore, f_{even} and f_{odd}, can be independently tuned by changing θ_2 and θ_3, respectively, with θ_1 fixed.

To verify the analysis, EM simulation results of the resonator under a week coupling with $Z = 98$ Ohm, $\theta_1 = 54°$, $\theta_2 = 36.7°$, and $\theta_3 = 4°$ are illustrated in Fig. 3-5(a). The proposed composite resonator has two resonant modes, f_{even} and f_{odd}. Moreover, two potential transmission zeros (TZs), TZ_{VG1} and TZ_{VG2}, are observed at the lower and upper sides of two resonant modes, respectively, they are mainly produced by the virtual grounds existed in composite resonator (when Y_{ine} and Y_{ino} are equal to ∞), and the phases reversal ($\Delta\phi = 180°$) at the TZs. The variation of resonant frequencies with θ_2 and $2\theta_3$ is illustrate in Fig. 3-5(b), which verify that f_{even} and f_{odd} can be independently controlled by changing θ_2 and θ_3, respectively.

According to the above analysis, it shows that the proposed two type MMRs both have multiple controllable resonance modes and compact structure size. Both of the two types of resonators are suitable for designing multi-band BPF with controllable frequencies and flexible frequency ratio.

3.3 Compact Dual-Band Bandpass Filters Using Stub-Loaded Stepped Impedance Resonators

In this section, an open-circuited stub-loaded quarter-wavelength steeped impedance resonator is adopted to design a compact bandpass filter with high selectivity performance. The compact dual-band BPF operating at 1.27 GHz for GPS-L2 application, and 2.45 GHz for WLAN application is designed and fabricated by using two stub-loaded stepped impedance resonators (SLSIRs). Mixed electric and magnetic coupling is introduced between two SLSIRs to produce multiple transmission zeros located at the two side of each passband, resulting in high passband selectivity and large isolation in-between the

two passbands. The filter is very compact and the measured results confirm the design well. The detail design procedure and the operating mechanism will be expressed and analyzed in detail in the following parts.

3.3.1 Analysis of the Modified Stub-Loaded Quarter-Wavelength SIR
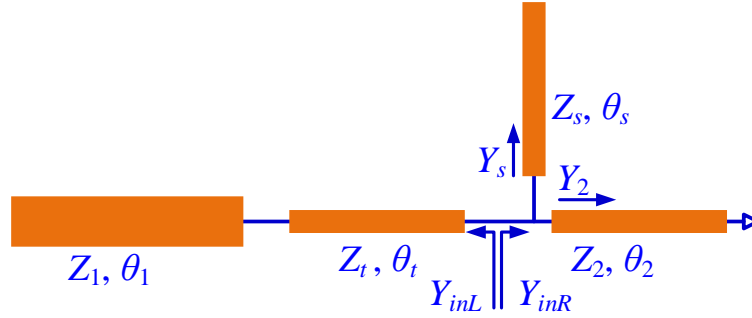
Fig. 3-6: Transmission line model of the proposed SLSIR.

Fig. 3-6 shows the transmission line model of the proposed stub-loaded stepped impedance resonator (SLSIR). The SIR is short-circuited at its high-impedance end. An open stub is loaded to this SIR. At the loading point, as shown in Fig. 1, the input admittance Y_{inL} looking to the left side, and Y_{inR} looking to the right side, can be derived easily using the transmission line theory as

$$Y_{inL} = -j\frac{Z_t + Z_1 \tan\theta_t \cot\theta_1}{Z_t\left(Z_t \tan\theta_t - Z_1 \cot\theta_1\right)} \tag{3.15}$$

$$Y_{inR} = Y_2 + Y_s = -j\frac{Z_s \cot\theta_2 - Z_2 \tan\theta_s}{Z_2 Z_s} \tag{3.16}$$

where Z_i (1, 2, s, t) and θ_i (1, 2, s, t) represent the characteristic impedances and electrical lengths of the transmission lines shown in Fig. 1, respectively. In order to make the design easier, we assume $Z_t = Z_2 = Z_s = Z$, and use $K = Z/Z_1$ to represent impedance ratio.

The resonance of the resonator occurs when $Y = Y_{inL} + Y_{inR} = 0$. On the other hand, when $Y = Y_{inL} + Y_{inR}$ approaches infinity, we will get a transmission zero. Fig. 3.7 shows the resonance characteristic with week coupling of the proposed SLSIR. It is seen that the proposed SLSIR resonates at two frequencies, f_{p1} and f_{p2}. By using Equation (3.15) and (3.16), and with appropriate choosing of the parameters of K and θ_i, we can make the two resonant modes operating at 1.27 and 2.45 GHz, respectively.
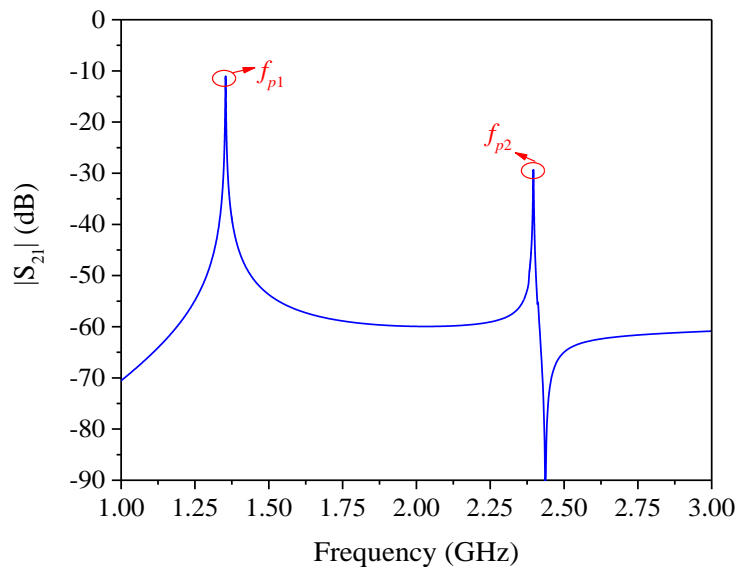
Fig. 3-7: The resonance characteristic with week coupling of the proposed SLSIR.

3.3.2 Design and Implement of the Dual-Band BPF with MEMC

Fig. 3-8(a) shows the layout of the proposed dual-band BPF. Two SLSIRs are used. The lower modes resonating at 1.27 GHz of the two SLSIRs are used to build the first passband, while the higher modes resonating at 2.45 GHz are used to form the second passband. The input and output feed lines and the loaded open stubs of the SLSIRs are folded and interlaced to reduce the circuit size and increase the coupling. The fringing electric fields across the gap g_c between the open stubs of the SLSIRs provide electric-coupling between the two resonators, while the electrical currents flowing on the open stubs produce magnetic-coupling between the two resonators. So the coupling between both the lower modes and higher modes of the SLSIRs are mixed electric and magnetic couplings [1]. Fig. 3-8(b) shows the coupling routing scheme of this proposed dual-band BPF.

The open stub creates one transmission zero (TZ_1) located at the lower sideband of the first passband. One the other hand, due to the cancelling effect of the mixed electric and magnetic couplings, the proposed dual-band BPF has another three TZs (TZ_2, TZ_3 and TZ_4). In addition, the coupling gap g_c and the folded open stubs can also be used to control the coupling coefficient of the dual-band BPF. It can meet the needed coupling coefficient for two passbands by selecting appropriate dimensions of g_c, g_l, L_t, and W_l. The external quality factor Q_{e1} and Q_{e2} can be met by choosing the length L_f of the folded

feedline. According to [2], once the coupling routing scheme, coupling coefficient, and external quality factor of the dual-band filter are determined, it can obtain an initial dual-band response. And then, the initial dimensions of the dual-band filter can be determined. In order to obtain the desire response, the layout of electromagnetic effects in Fig. 3-8(b) should be considered. The final parameters optimized by using an electromagnetic simulator, Sonnet EM, are as follows: $L_1 = 3.65$, $L_2 = 5.97$, $L_t = 5.55$, $L_s = 29.9$, $L_f = 25.85$, $L_l = 1.8$, $W = 1.7$, $W_1 = 2.4$, $W_s = 0.5$, $W_l = 0.2$, $g_f = g_c = 0.2$, $g_l = 0.6$, $d_1 = 0.4$, $d_2 = 0.8$, all in mm. The characteristic impedances of the input and output ports are both 50 Ohms.
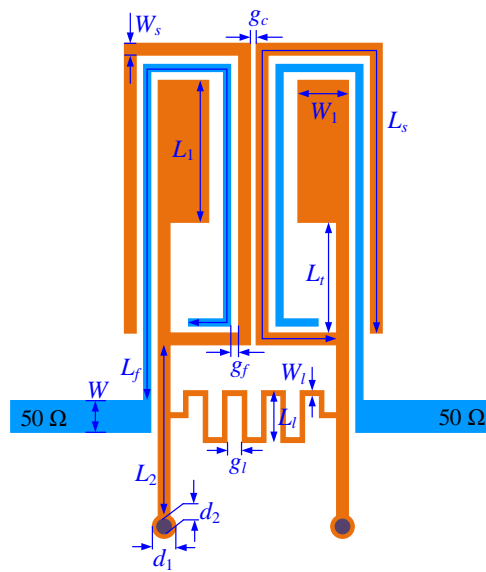
(a)
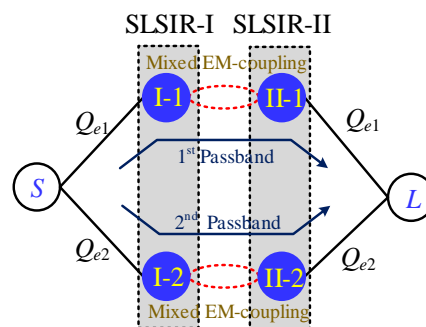
(b)

Fig. 3-8: (a) Layout of the proposed dual-band BPF. (b) Coupling routing scheme of the proposed dual-band BPF.

3.3.3 Experimental Results and Discussion
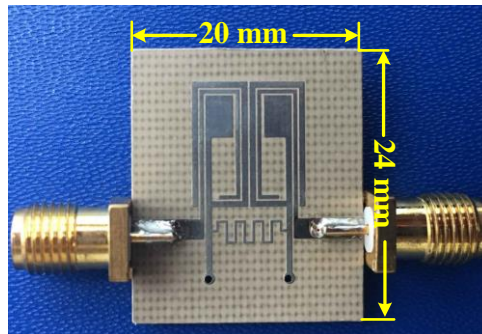
Fig. 3-9: Photograph of the fabricated dual-band BPF.
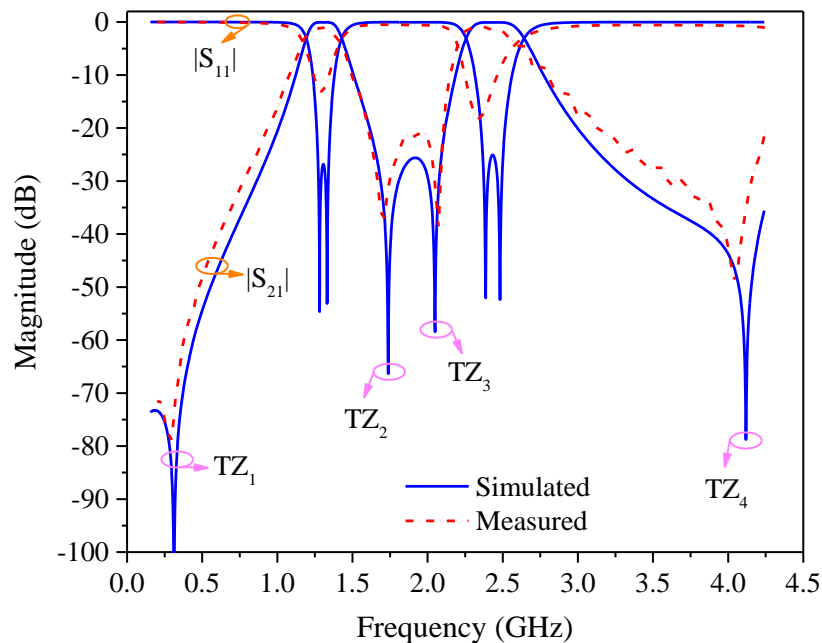
Fig. 3-10: Simulated and measured responses of the proposed dual-band BPF.

The final dual-band BPF is fabricated on a Taconic RF-35 substrate with a relative dielectric constant of 3.5 and a thickness of 0.8 mm. The photograph of the fabricated filter is shown in Fig. 3-9. The measurements were carried out using a network analyzer (E5071C, Keysight Technologies). The simulated and measured frequency responses of the dual-band BPF are given in Fig. 3-10. The measured two passbands are located at 1.27 and 2.45 GHz with a 3-dB bandwidth of 270 MHz (21.3%) and 360 MHz (14.7%), respectively. The measured minimal insertion losses (ILs) at the two center frequencies are 0.90/0.92 dB, and the return losses (RLs) within the two passbands are better than

13/18.5 dB, respectively. Four transmission zeros are measured at 0.3/1.7/2.1/4.0 GHz, which make the two passbands good at frequency selectivity. The isolation between the two passbands is better than 21 dB.

TABLE 3.1. Performance comparison with other dual-band BPFs

Refs	CFs (GHz)	3-dB FBW (%)	IL (dB)	TZs	Circuit size ($\lambda_g \times \lambda_g$)
[3]	1.0/1.44	10/9.3	0.85/0.9	5	0.1×0.25
[4]	2.45/5.2	18/4.8	0.6/0.9	3	0.11×0.23
[5]	3.32/5.32	27.71/19.17	0.62/0.91	4	0.084×0.102
[6]	0.58/1.31	39.6/18.3	0.3/0.9	3	0.04×0.54
[7]	1.63/2.73	7.5/5.1	1.5/2.15	7	0.25×0.25
This work	**1.27/2.45**	**21.3/14.7**	**0.90/0.92**	**4**	**0.084 ×0.102**

Table 3.1 gives a performance comparison with other reported dual-band BPFs. Compared with previous works, significant size reduction is achieved in this work. The center frequencies (CFs) and 3-dB FBW of the two passbands can be more easily controlled relative to the work in [4]. As shown in the work in [7], the BPF of this work has smaller insertion losses. In a word, this work has advantage in selectivity, circuit size, and complexity of design process.

3.4 Novel Compact Dual-Band Bandpass Filter Using Stub-Loaded Shorted Stepped-Impedance Resonators

In this section, a compact dual-band BPF is developed by using a new stub-loaded shorted SIR. A detailed analysis of the stub-loaded shorted SIR is given firstly, and then a parametric study of the dual-band BPF is carried out. The obtained results and related discussions reveal that with appropriate design of the geometrical parameters of the proposed structure, a dual-band BPF with individually controllable mid-band frequencies, passband bandwidths, and transmission zeros, can be designed with great flexibility.

Fig. 3-11 shows the configuration of the proposed dual-band BPF, which consists of two stub-loaded shorted stepped-impedance resonators (SIRs) with mixed electric and magnetic coupling, and a pair of dual-feedline structures (DFSs). As shown by the analysis of the resonator below, the even and odd-mode of the stub-loaded shorted SIRs

can be controlled separately to constitute two passbands with individually controllable mid-band frequencies. On the other hand, the parametric study of the filter illustrates that both the transmission zeros and the bandwidths of the two passbands can be controlled independently by using different geometrical parameters.
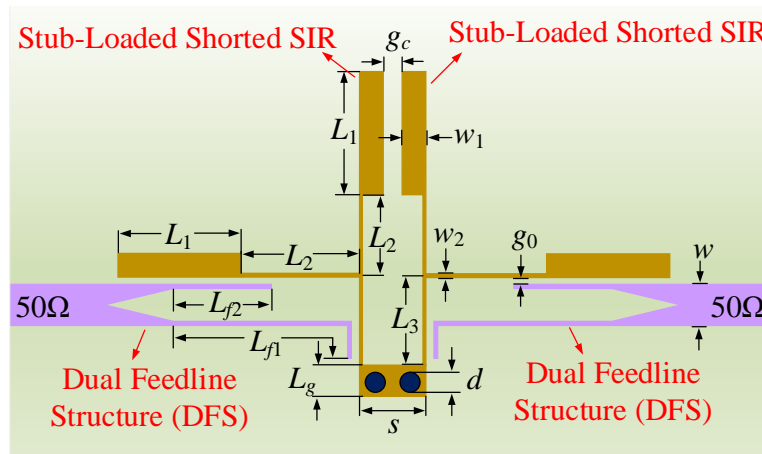
Fig. 3-11: Configuration of the proposed dual-band BPF.

3.4.1 Analysis the Stub-Loaded Shorted SIR

(a) (b) (c)
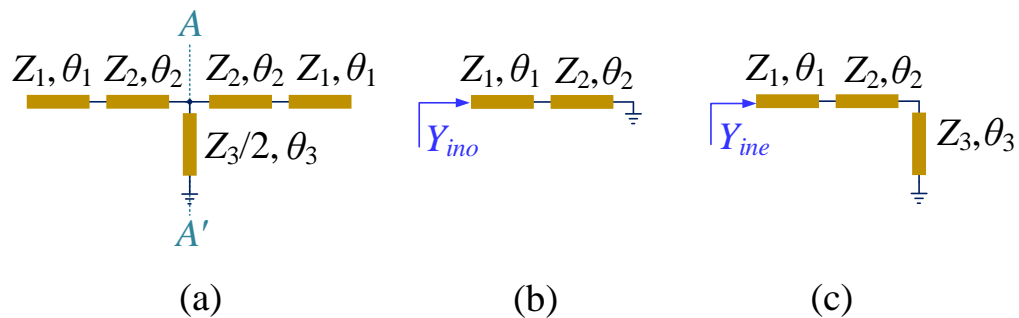
Fig. 3-12: Configuration of the proposed dual-band BPF.

Fig. 3-12(a) shows the transmission line model of the proposed stub-loaded shorted SIR. Since it is a symmetrical structure, it can be readily analyzed by the even- and odd-mode method. The simplified circuit of the odd- and even-mode are given in Fig. 3-12(b) and (c), respectively, from which, the input admittance, Y_{ino} and Y_{ine}, seen from the open ends as shown in Fig. 3-12(b) and (c), are derived as follows:

$$Y_{ino} = \frac{1 - R_z \tan\theta_1 \tan\theta_2}{jZ_1 \left(R_z \tan\theta_2 + \tan\theta_1 \right)} \tag{3.17}$$

$$Y_{ine} = \frac{1 - R_z \tan\theta_1 \tan\left(\theta_2 + \theta_3\right)}{jZ_1 \left[R_z \tan\left(\theta_2 + \theta_3\right) + \tan\theta_1 \right]} \tag{3.18}$$

where $R_z = Z_2/Z_1$. The resonance of the odd-mode or even-mode occurs when $Y_{ino} = 0$ or $Y_{ine} = 0$, so we get

$$1 - R_z \tan\theta_1 \tan\theta_2 = 0 \qquad @\ f_o \tag{3.19}$$

$$1 - R_z \tan\theta_1 \tan\left(\theta_2 + \theta_3\right) = 0 \qquad @\ f_e \tag{3.20}$$
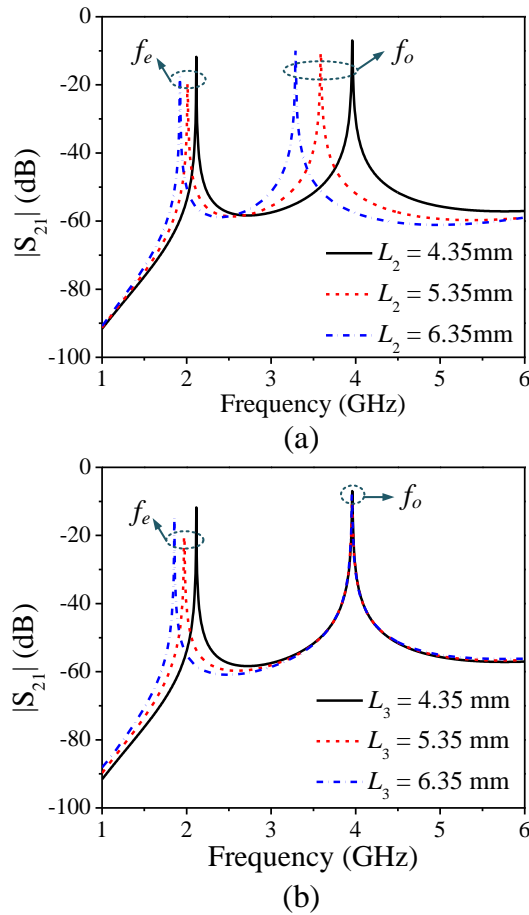
Fig. 3-13: (a) Variation of f_o and f_e versus different lengths of L_2 (θ_2). (b) Variation of f_e versus different lengths of L_3 (θ_3). The f_o remains unchanged.

From (3.19) and (3.20), it is seen that the both the odd-mode f_o and even-mode f_e can be varied by changing θ_1 and θ_2, while the even-mode f_e can also be varied individually

by changing θ_3. This conclusion can also be verified by Fig. 3-13 (a) and (b), from which, it seen that both f_o and f_e varies with different lengths of L_2 (θ_2), while when L_3 (θ_3) is increased, only f_e is shifted to lower frequencies and f_o remains unchanged. Therefore, with appropriate selection of the lengths L_1, L_2, and L_3, we can design a dual-band BPF with individually controllable mid-band frequencies.

3.4.2 Key Parameters Study of the Dual-Band FPD

To further characterize the design, a parametric study of the dual-band BPF is carried out by using an EM simulator. Three key parameters, the diameter d of the ground holes, the coupling gap g_c between the two stub-loaded shorted SIRs, and the length L_g of the ground patch size, as shown in Fig. 1, are used in the investigation.

Fig. 3-14(a)-(c) show the simulated transmission coefficient S_{21} with different parameters. In the figures, it is seen there are two passbands and three transmission zeros (TZs). The first TZ_1 is mainly determined by the total length of the loaded open stubs and occurs close to the even-mode frequency. Hence, it varies with different d and L_g, but does not vary with the gap g_c. On the other hand, TZ_2 and TZ_3 are produced by the mixed electric and magnetic coupling between two stub-loaded shorted SIRs, so they vary significantly with the three parameters, d, g_c, and L_g, with an exception that d has little influence on TZ_3.

In Fig. 3-14(b), it is seen that with the increasing coupling gap g_c, the TZ_3 moves to lower frequencies as the electric coupling between the two shorted SIRs decreases [8]. When g_c is as large as 1.5 mm, the electric coupling approaches zero, and TZ_2 and TZ_3 disappeared consequently.

As shown in Fig. 3-14(b), the bandwidth of the second passband become narrower with g_c ranging from 0.8 mm to 1.2 mm and the bandwidth of the first passband is keep unvaried. As can be observed from Fig. 3-14(c), as L_g increases, the bandwidth of the first passband becomes wider while that of the second passband remains unchanged.

In summary, the transmission zeros and the bandwidths of the two passbands can be controlled independently by using different geometrical parameters, and this facilitates the design of a dual-band BPF with great flexibility to meet different specifications.
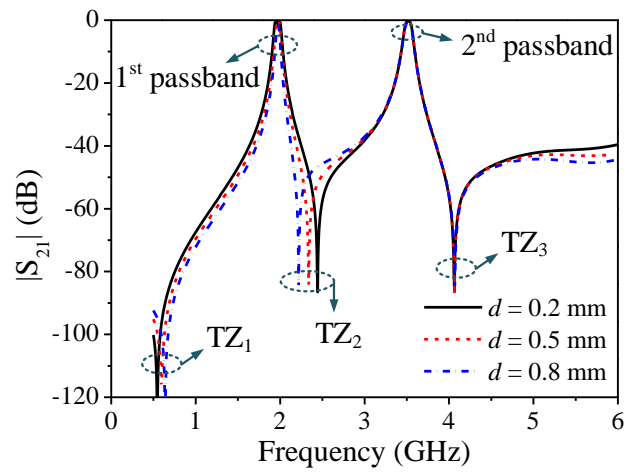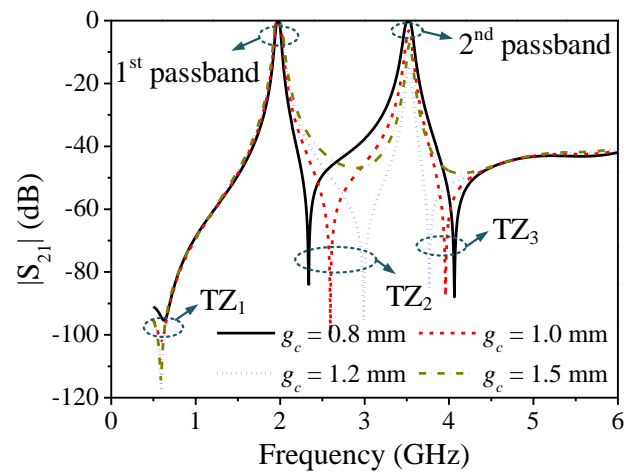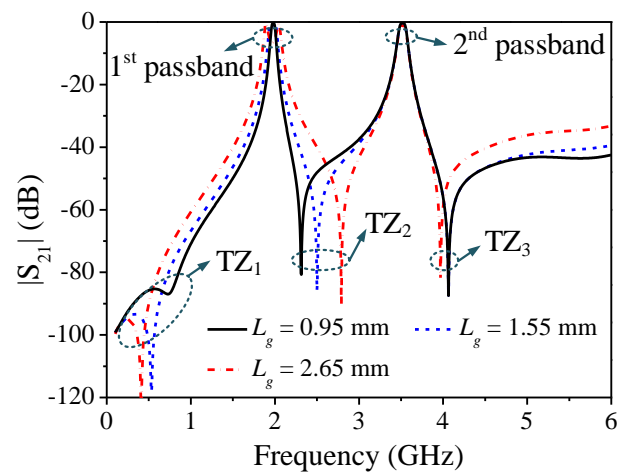
Fig. 3-14: Simulated S_{21} with different (a) diameter d of the ground holes, (b) coupling gap g_c, and (c) length L_g of the ground patch size.

3.4.3 Experimental Results and Discussion
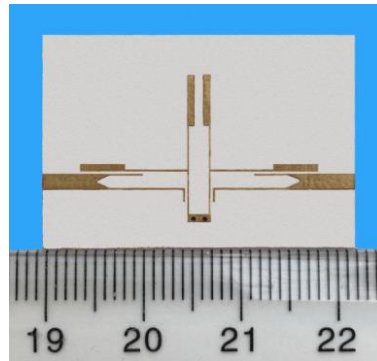
Fig. 3-15: Photograph of fabricated dual-band BPF. Dimensions of the circuit are $L_1 = 5.4$, $L_2 = 4.35$, $L_3 = 4.35$, $L_4 = 5.4$, $L_5 = 4.35$, $L_{f1} = 8.55$, $L_{f2} = 2.9$, $L_g = 1.05$, $w = 1.8$, $w_1 = 0.9$, $w_2 = 0.2$, $g_0 = 0.2$, $g_c = 0.8$, $s = 2.2$, and $d = 0.5$. (Unit: mm).
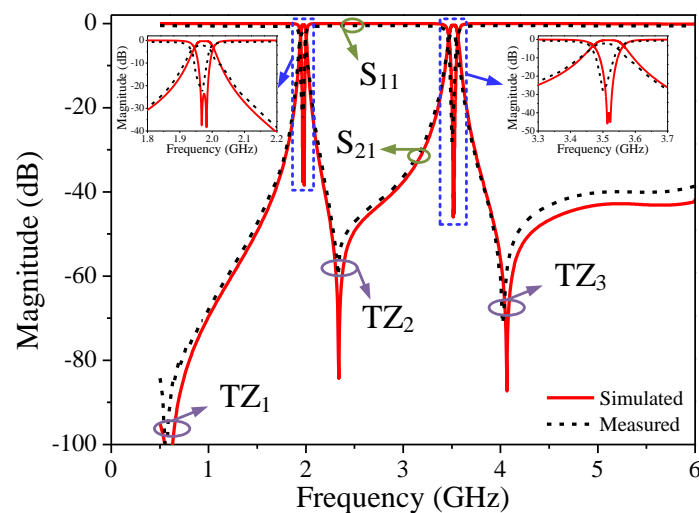
Fig. 3-16: Simulated and measured results of the proposed dual-band BPF.

Based on the above investigation and discussion, a dual-band BPF is designed and fabricated on a Taconic RF-35 substrate with a relative dielectric constant of 3.5 and a thickness of 0.8 mm. The photograph of the fabricated filter as shown in Fig. 3-15 with the final geometrical dimensions. The measurements were carried out using a network analyzer (E5071C, Keysight Technologies). The simulated and measured frequency responses of the filter is plotted in Fig. 3-16. Two passbands are measured at 1.96 and 3.5 GHz with 3-dB bandwidths (BW) of 58.4 MHz (2.98%) and 92.4 MHz (2.64%), respectively. The measured minimal insertion losses are 1.25/1.72 dB at the respective

center frequencies, and the return losses within two passbands are better than 22/28 dB, respectively. Three TZs around the two passbands are measured at 0.56/2.32/4.03 GHz. The isolation in between the two passbands is better than 40 dB. Finally, Table 3.2 compares the proposed filter with several reported dual-band BPFs, where it is shown the merits of this work about good dual-passband performance and compact size.

TABLE 3.2. Comparison with previous works

Refs	f_{c1}/f_{c2} (GHz)	IL (dB)	RL (dB)	TZs	Circuit size ($\lambda_g \times \lambda_g$)
[9]	1.84/2.65	0.43/0.65	13.4/15.5	4	0.17×0.21
[10]	1.63/2.73	1.5/2.15	19/22	7	0.25×0.25
[11]	1.8/3.5	0.8/0.9	25/18	5	0.15×0.12
[12]	1.8/3.5	0.21/0.25	30/19	3	0.20×0.26
[13]	1.8/5.8	1.33/1.7	21/13	2	0.23×0.17
	2.4/5.8	1.35/1.97	17/15	3	0.39×0.25
This work	**2.3/3.5**	**1.25/1.72**	**22/28**	**3**	**0.25×0.23**

3.5 Individually Controllable Dual-Band Bandpass Filter With Multiple Transmission Zeros and Wide Stopband

In this section, an open-ended stub-loaded shorted-circuited stepped-impedance resonator (OSL-SSIR) is analyzed at first. Next, a dual-band BPF is proposed, and its external and internal coupling behaviors are investigation in detail. Multiple mixed electric- and magnetic-coupling paths are introduced to produce transversal signal interference and multiple transmission zeros (TZs). Descriptions on the mechanism of the TZs are provided. Finally, a DB-BPF is designed, fabricated, and its measured response is compared with the simulated one.

3.5.1 Analysis of the Open-Ended Stub-Loaded Shorted-Circuited Stepped Impedance Resonator

Fig. 3-17(a) shows the transmission line model of the open-ended stub-loaded short-circuited stepped-impedance resonator (OSL-SSIR), which consist of four sections: a low

impedance section (Y_1, θ_1), a high impedance middle section (Y_2, θ_2), a short-circuited high impedance section (Y_3, θ_3), and an open-ended stub section (Y_s, θ_s). Among the multiple resonances of the OSL-SSIR, the two fundamental resonances with frequencies f_L and f_H are adopted to form the two passbands, respectively. The corresponding current distributions of the two resonances are shown in Fig. 3-17(b) and (c), respectively. It is observed from Fig. 3-17(b) that the resonance at f_L is occurred at the straight quarter-wavelength SIR, and the open-ended stub has no effect on this resonance. On the other hand, as illustrated in Fig. 3-17(c), the resonance at f_H is happened at the T-shaped resonator, and all line sections of the OSL-SSIR have influence on this resonance. According to above analysis, the input admittances Y_{inL} and Y_{inH} at the two resonant frequencies f_L and f_H can be derived as

$$Y_{inL} = Y_{in1} + Y_{in3} \qquad @ f_L \qquad (3.21)$$

$$Y_{inH} = Y_{in1} + Y_{in2} + Y_{in3} \qquad @ f_H \qquad (3.22)$$

where

$$Y_{in1} = Y_2 \frac{jY_1 \tan\theta_1 + jY_2 \tan\theta_2}{Y_2 - Y_1 \tan\theta_1 \tan\theta_2} \qquad (3.23)$$

$$Y_{in2} = jY_s \tan\theta_s \qquad (3.24)$$

$$Y_{in3} = -jY_3 \cot\theta_3 \qquad (3.25)$$
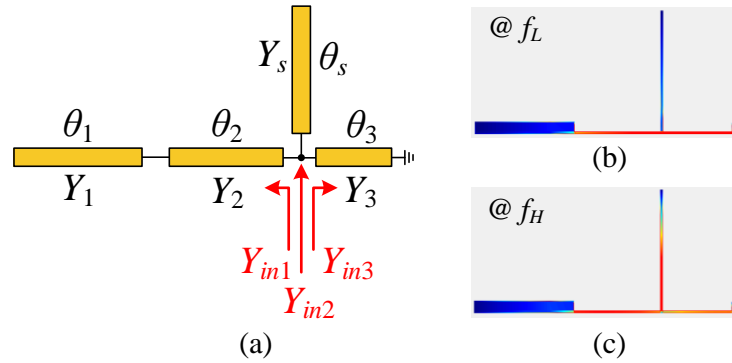
Fig. 3-17: (a) Transmission line model of the OSL-SSIR. (b) Current distribution of OSL-SSIR resonating at f_L. (c) Current distribution of OSL-SSIR resonating at f_H.

To simplify the design, we assume that $Y_2 = Y_3 = Y_s$ and define the admittance ratio $K = Y_1/Y_2$. Then, the two resonance frequencies f_L and f_H can be determined from the resonance condition $Y_{inL} = 0$ and $Y_{inH} = 0$, respectively, which result in the following two equations:

$$Y_2\left(K\tan\theta_1\tan\theta_2-1\right)\cot\theta_3+K\tan\theta_1+\tan\theta_2=0 \qquad @f_L \quad (3.26)$$

$$Y_2\left(K\tan\theta_1\tan\theta_2-1\right)\left(\tan\theta_s-\cot\theta_3\right)-K\tan\theta_1-\tan\theta_2=0 \quad @f_H \quad (3.27)$$

From (3.26) and (3.27), it is seen that θ_s has only effect on the higher resonance frequency f_H, but no effect on f_L. Therefore, the two resonance frequencies can be individually controllable by adjusting the open-end stub, and this is very important in the design of DB-BPF.

Fig. 3-18 shows the variation of the two resonance frequencies f_L and f_H with different electrical lengths of θ_1, θ_2, θ_3, and θ_s when $K = 2$ and $Y_2 = 0.008$ S. When one of θ_1, θ_2, θ_3, and θ_s is chosen as the variant, the other three are given electrical lengths from the following values: $\theta_1 = 27.5°$, $\theta_2 = 20.5°$, $\theta_3 = 18.5°$, $\theta_s = 27.5°$. It can be observed that with the increase of θ_1, θ_2, or θ_3, both f_L and f_H decrease. On the other hand, with the increase of θ_s, only f_H decreases, while f_L remains almost unvaried. So, it is easy to make individual control of these two frequencies.
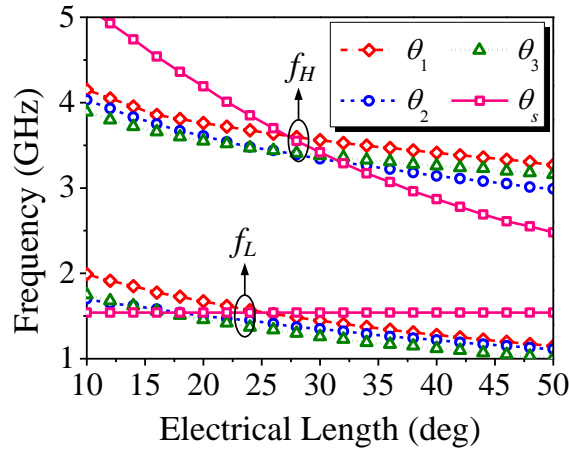
Fig. 3-18: Variation of f_L and f_H with different θ_1, θ_2, θ_3, and θ_s.

3.5.2 Design of Dual-Band Bandpass Filter

Based on the above analysis, a compact DB-BPF is designed in this section. The configuration of the proposed DB-BPF is illustrated in Fig. 3-19, which consists of two OSL-SSIRs, a common short-circuited magnetic coupling stub, and a pair of parallel-coupled feed lines. For size reduction, the low impedance sections and the open stubs of the OSL-SSIRs are folded.

The second-order filter is designed to operate at 1.5 GHz and 3.65 GHz, with a fractional bandwidth (FBW) of 5% and 3%, respectively. The lumped circuit elements of the low-pass prototype filter are $g_0 = 1$, $g_1 = 0.6648$, $g_2 = 0.5445$, and $g_3 = 1.2210$, when

the two passbands of the DB-BPF have Chebyshev responses with a 0.04321-dB ripple in both passbands [2]. The required coupling coefficients $M_{12}^{I} = 0.0831$ and $M_{12}^{II} = 0.0499$, and the external quality factors of the two passbands $Q_e^I = 13.30$ and $Q_e^{II} = 22.16$ are calculated from the following well-known formulas:

$$M_{i,i+1} = \frac{FBW}{\sqrt{g_i g_{i+1}}} \quad \text{for } i = 1 \text{ to } n-1 \tag{3.28}$$

$$Q_e = \frac{g_0 g_1}{FBW} \tag{3.29}$$
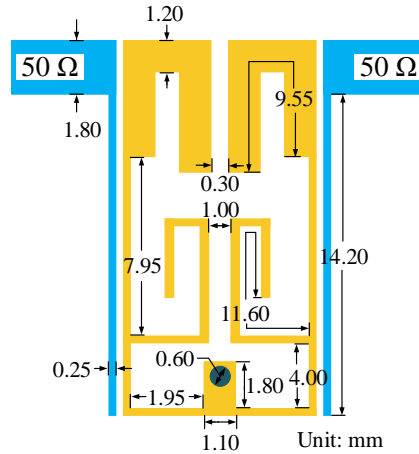
Fig. 3-19: Configuration of the proposed dual-band BPF.

Fig. 3-20(a) shows the variation of the simulated coupling coefficients between two neighboring OSL-SSIRs with the short-circuited stub width W_d and the diameter d of the short-circuited via-hole. It is seen that with the increase of W_d, the coupling coefficient of the lower passband (Band I) increases gradually, while the coupling coefficient of the higher passband (Band II) varies little. Fig. 3-20(b) illustrates shows the variation of the coupling coefficients with the folded line length L_L (when $S_H =1$mm) and the gap width S_H (when $L_L = 5.8$ mm) between two neighboring OSL-SSIRs.

Fig. 3-21 shows the variation of the simulated external quality factors of the OSL-SSIR with the length L_f of parallel-coupled feed line and the gap width C_f (when the width of parallel-coupled feed line $W_f = 0.25$mm). It is seen that both the external Q vales of the two passbands reduce with the increase of L_f. Also, as expected, with the increase of coupling gap C_f, both the external Q vales of the two passbands become larger.

Based on the above analysis, both the center frequencies and bandwidths of the two passbands can be individually controlled with appropriately chosen geometrical parameters of the proposed filter structure showing in Fig. 3-19. The finally obtained dimensions for the given design specifications of the DB-BPF are illustrated in Fig. 3-19.
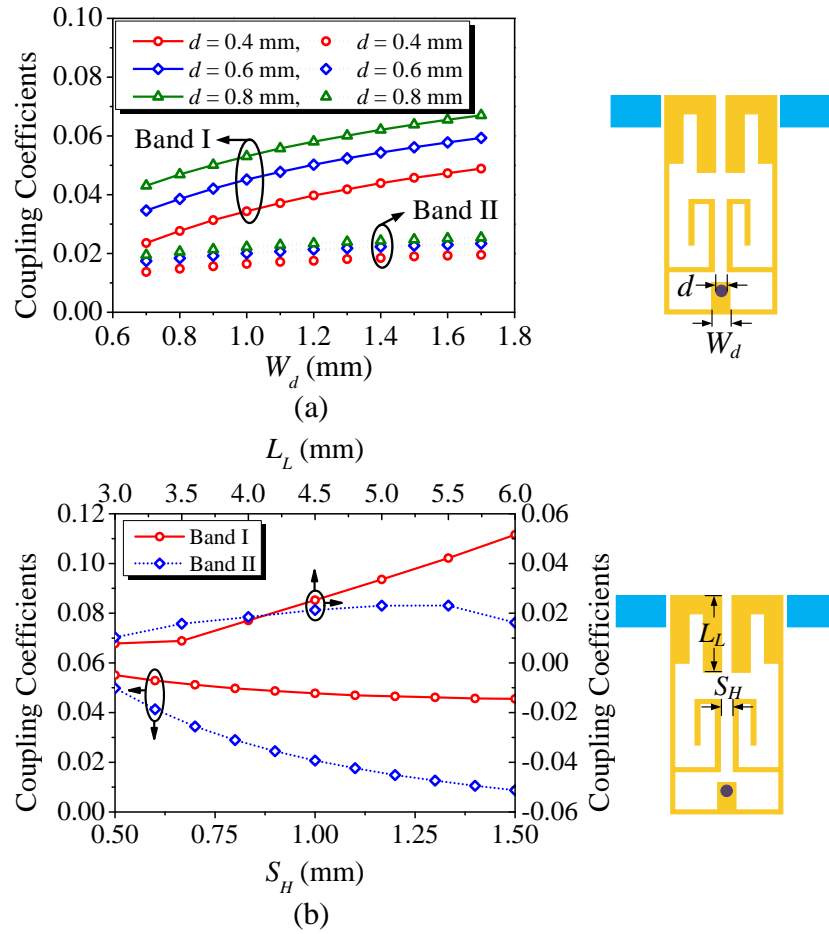
Fig. 3-20: Simulated coupling coefficients by an EM simulator. (a) Variation with W_d and d. (b) Variation with L_L when $S_H = 1$ mm, and variation with S_H when $L_L = 5.8$ mm.
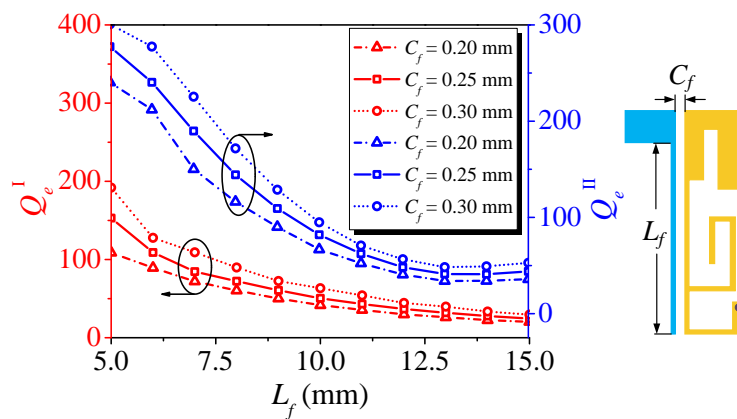
Fig. 3-21: Simulated coupling coefficients by an EM simulator. (a) Variation with W_d and d. (b) Variation with L_L when $S_H = 1$ mm, and variation with S_H when $L_L = 5.8$ mm.

3.5.3 Implementation and Experimental Results of the Proposed Dual-Band BPF
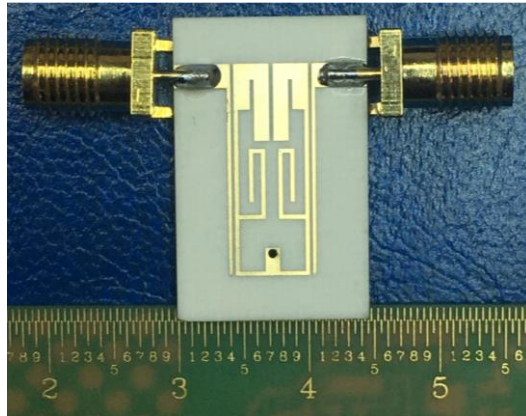
Fig. 3-22: Photograph of the fabricated dual-band BPF.
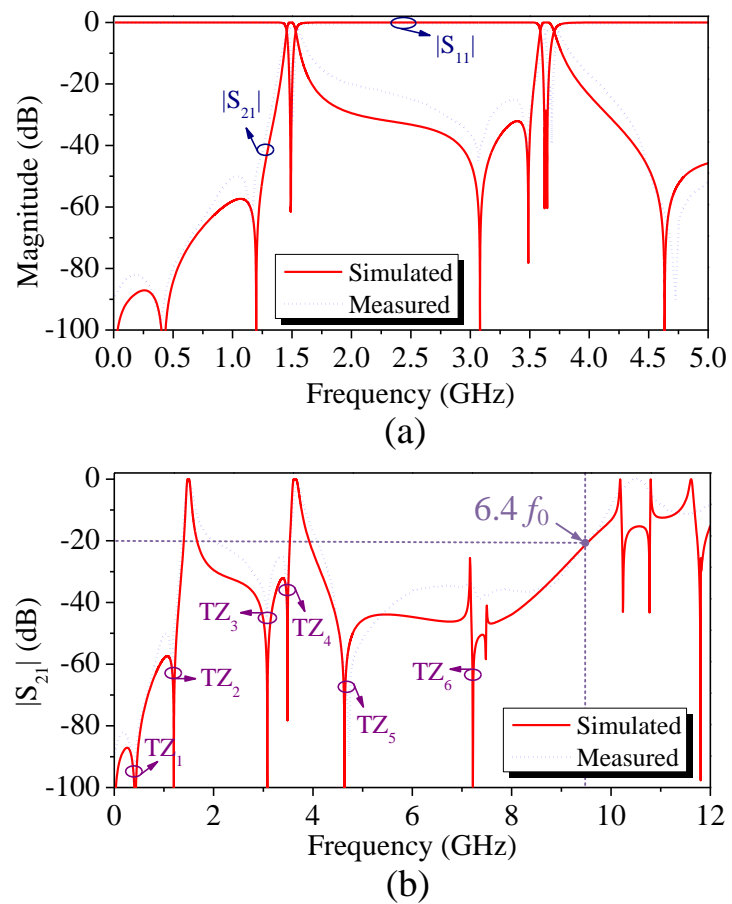
Fig. 3-23: Simulated and measured responses of the proposed DB-BPF. (a) Local frequency range response. (b) Wide frequency range response.

The designed DB-BPF is fabricated on a Rogers RO4003C substrate with a relative dielectric constant of 3.38 and a thickness of 0.813 mm. The photograph of the fabricated DB-BPF is shown in Fig. 3-22. The filter occupies an area of 16.0 mm × 6.5 mm excluding the feeding structure, which is about $0.13\lambda_g \times 0.05\lambda_g$, where λ_g is the guided wavelength at the center frequency $f_L = 1.5$ GHz of the lower passband.

In Fig. 3-23(a) and (b), the simulated frequency response of the DB-BPF by EM simulator is illustrated in solid lines. It is observed that the two passbands are centered at 1.5 and 3.65 GHz, and their corresponding FBW is 5.1% and 3.2%, respectively, which agree well with the desired specifications.

The measured response of the filter is drawn in Fig. 3-23(a) and (b) by dotted lines, which agree well with the simulated result. The measured maximum insertion loss of the two passbands, centered at 1.51 GHz and 3.68 GHz, are approximately 1.55 dB and 1.63 dB, respectively. The measured corresponding 3-dB bandwidths are 64.72 MHz (4.25%) and 95.72 MHz (2.60%), respectively. The measured return loss is better than 20 dB in both passbands. In addition, the stopband with a rejection level better than 20 dB is extended to 9.6 GHz ($6.4f_0$).

3.5.4 Analysis of Transmission Zeros and Performances Comparison
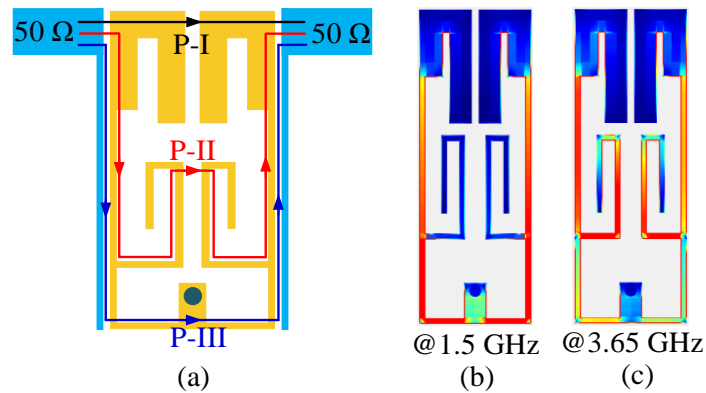
Fig. 3-24: (a) Coupling paths of the proposed DB-BPF. (b) Simulated current distribution at 1.5 GHz. (c) Simulated current distribution at 3.65 GHz.

Six transmission zeros (TZs) are observed at 0.44, 1.19, 3.09, 3.49, 4.64, and 7.20 GHz, which are represented by TZ_1, TZ_2, TZ_3, TZ_4, TZ_5, and TZ_6, respectively. These TZs are distributed on either side of the two passbands, which not only enhanced the selectivity of the filter, but also improved significantly the stopband property of the DB-BPF. TZ_1 is the inherent transmission zero of the DB-BPF, while TZ_6 is produced by the open-ended

stub of the OSL-SSIR. TZ_2, TZ_3, TZ_4, and TZ_5 are created by transversal signal interference of the multiple mixed electric and magnetic coupling paths [30, 31]. As indicated in Fig. 3-24(a), there are three signal transmission paths, i.e., P-I, P-II, and P-III for the two passbands. When the phase difference between two paths is odd times of 180°, a TZ will be created. From the current distributions in Fig. 3-24(b) and (c), we judge that the P-I and P-III provide electric coupling and magnetic coupling respectively for the lower passband, while the P-II and P-III provide magnetic coupling and electric coupling respectively for the higher passband. This judgment can also be verified by the extracted coupling coefficient showing in Fig. 3-20.

Table 3.3 lists the phase shifts for each signal path of the designed DB-BPF. It is observed that the two paths are out of phase at both below and above the resonance of the lower passband (Band I). Therefore, two TZs are produced on the both sides of the lower passband, as shown by TZ_2 and TZ_3 in Fig. 3-23(b). Similarly, the P-II and P-III are also out of phase at both below and above resonance of the higher passband (Band II). As a result, TZ_4 and TZ_5 are generated on the low skirt and upper skirt of the higher passband, respectively, as shown in Fig. 3-23(b).

Table 3.3 Phase shifts of each coupling path between the DB-BPDs in Fig. 3-24.

Passband	Location	Path	R1	M12	R2	Total Phase Shift	Phase Difference	Results
Band I	Below Resonance	P-I	+90°	−90°	+90°	+90°	180° (Out Phase)	TZ_2
		P-III	+90°	+90°	+90°	+270°		
	Above Resonance	P-I	−90°	−90°	−90°	−270°	180° (Out Phase)	TZ_3
		P-III	−90°	+90°	−90°	−90°		
Band II	Below Resonance	P-II	+90°	+90°	+90°	+270°	180° (Out Phase)	TZ_4
		P-III	+90°	−90°	+90°	+90°		
	Above Resonance	P-II	−90°	+90°	−90°	−90°	180° (Out Phase)	TZ_5
		P-III	−90°	−90°	−90°	−270°		

A comparison of this work with previous DB-BPFs is given in Table 3.4 in terms of their center frequencies, 3-dB FBW, insertion losses, return losses, TZs, out-band suppression (Supp.) (which is the ratio of the highest upper stopband frequency with rejection level better 20 dB to the center frequency of the first passband $f_0 = 1.5$ GHz),

and circuit size. It is observed that the overall performances of the proposed DB-BPF outperforms the others, especially in the terms of the return loss and circuit size.

Table 3.4 Comparison with previous DB-BPFs.

Ref.	CF/GHz	FBW/%	IL/dB	RL/dB	TZs	Supp.	Size ($\lambda_g \times \lambda_g$)
[14]	3.32/5.32	27.7/19.2	0.62/0.91	20/20	4	$2.70f_0$	0.18×0.40
[15]	3.00/5.34	10.0/3.7	0.19/2.34	13/15	4	NA	0.15×0.26
[16]	1.5/2.35	5.96/7.19	1.43/1.15	22/20	3	$2.33f_0$	0.06×0.14
[17]	2.71/5.05	10.3/8.7	0.2/0.9	NA	2	$7.01f_0$	0.06×0.14
[18]	3.78/4.82	11.3/10.7	1.38/1.82	14/30	>13	$10.5f_0$	0.16×0.31
This work	1.51/3.68	4.25/2.6	1.55/1.63	28/21	6	$6.4f_0$	0.05×0.13

3.6 Design of Compact Tri-Band Bandpass Filter Using Stub-Loaded Quarter-Wavelength SIRs

In this section, a modified SL-SIR is proposed and analyzed to design a compact tri-band BPF. With different schematics of the loaded stubs, the SL-SIR has flexibly controllable resonance modes to construct dual-band or tri-band BPFs. As an example, the tri-mode resonator is chosen to design a tri-band BPF. The configuration of the BPF is devised to allow four geometrical parameters to realize flexible variation of the FBWs of the three passbands. Two separately changeable source-load coupling paths are devised to produce up to ten transmission zeroes, which not only enhance significantly the selectivity of three passbands, but also widen greatly the stopband of the BPF.

3.6.1 Analysis of the Modified Stub-Loaded Stepped-Impedance Resonator

The SL-SIR has an open stub with Z_1 and θ_1 at its one end, and a short-circuited stub with Z_t and θ_t at the other end, together with a loaded structure indicated by Z_S. With the different stub-loaded situation, the proposed SL-SIR have two cases of dual-mode and tri-mode. In the tri-mode case, the loaded structure consists of two shunt open stubs with (Z_{s1}, θ_{s1}) and (Z_{s2}, θ_{s2}), respectively, as shown in Fig. 3-25(c). The simulated response S_{21} of

the proposed SL-SIR under week coupling is given in Fig. 3-25(d), from which, it is clearly seen that in case 1, the proposed SL-SIR behaves as a dual-mode resonator, while in case 2, it performs as a tri-mode resonator.
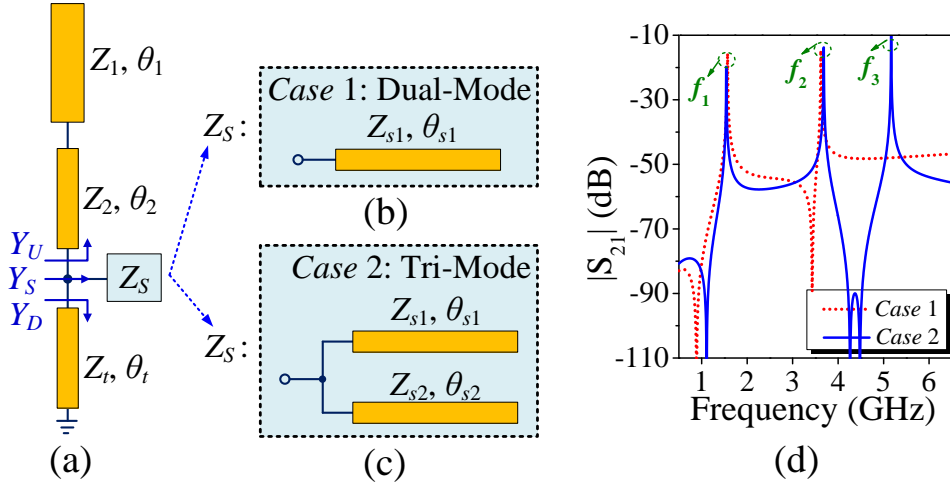
Fig. 3-25: (a) Transmission line model of the stub-loaded λ/4 SIR (SL-SIR). (b) Case 1: loaded with one open stub. (c) Case 2: loaded with two shunt open stubs. (d) Simulated S$_{21}$ of the SL-SIR with different loaded stubs.

By referring to Fig. 3-3(a)-(c), we can derive the input admittances of the three paths as follows, with assumption that $Z_2 = Z_t = Z_{s1} = Z_{s2}$, and $R_z = Z_2/Z_1$:

$$Y_{in}^{Path\ I} = j\frac{R_z \tan\theta_1 \tan(\theta_2+\theta_t)-1}{Z_1\left[\tan\theta_1 + R_z \tan(\theta_2+\theta_t)\right]} \tag{3.30}$$

$$Y_{in}^{Path\ II} = j\frac{1+ R_z \tan\theta_1 \cot(\theta_2+\theta_{s1})}{Z_1\left[R_z \cot(\theta_2+\theta_{s1})-\tan\theta_1\right]} \tag{3.31}$$

$$\begin{aligned}Y_{in}^{Path\ III} &= Y_U + Y_D + Y_S \\ &= j\frac{R_z + R_z \tan\theta_2(\cot\theta_t - \tan\theta_{s1} - \tan\theta_{s2})}{R_z Z_1(\cot\theta_1 - R_z \tan\theta_2)} \\ &+ j\frac{\cot\theta_1(\tan\theta_2 - \cot\theta_t + \tan\theta_{s1} + \tan\theta_{s2})}{R_z Z_1(\cot\theta_1 - R_z \tan\theta_2)}\end{aligned} \tag{3.32}$$

The resonance condition for the three modes at f_1, f_2, and f_3, are given by the following equations:

$$R_z \tan\theta_1 \tan(\theta_2+\theta_t)-1=0 \qquad\qquad \text{for } f_1 \tag{3.33}$$

$$1 + R_z \tan\theta_1 \cot(\theta_2 + \theta_{s1}) = 0 \qquad\qquad \text{for } f_2 \qquad (3.34)$$

$$\begin{aligned} R_z + R_z \tan\theta_2 \left(\cot\theta_t - \tan\theta_{s1} - \tan\theta_{s2} \right) \\ + \cot\theta_1 \left(\tan\theta_2 - \cot\theta_t + \tan\theta_{s1} + \tan\theta_{s2} \right) = 0 \end{aligned} \quad, \qquad \text{for } f_3 \qquad (3.35)$$

From (3.33) and (3.34), it is seen that we can change the frequencies f_1 and f_2 independently by varying the electrical length θ_t and θ_{s1}. Furthermore, we can change the frequency f_3 by varying the electrical length θ_{s2} without affecting the other two frequencies f_1 and f_2.

3.6.2 Design of Tri-Band BPF

After the design as described above, two tri-mode SL-SIRs are used to construct a tri-band BPF whose configuration is shown in Fig. 3-26(a). The coupling scheme of this tri-band BPF is shown in Fig. 3-26(b). The resonance modes at f_1, f_2, and f_3 of the two SL-SIRs are used to form the first, second, and third passbands, respectively. The two resonators are folded to reduce the circuit size and at the same time, to get four geometrical parameters to control the coupling strength between them: the diameter d of the ground via hole commonly used by the two resonators, the gaps g_0, g_1 and g_2, between the other three open stubs of the two resonators. Fig. 3-27(a)-(d) show the variation of the 3-dB fractional bandwidths (FBWs) of the three passbands of the filter versus these four parameters. From Fig. 3-27(a), (b), and (d), it is seen that the FBW of the first, second, and third passband is significantly varied versus d, g_0, and g_2, respectively, while the FBWs of the other two passbands varied little. Fig. 3-27(c) shows that the FBWs of all these three passbands can be adjusted simultaneously by changing g_1. Therefore, the FBWs of the tri-band BPF can be independently controlled using these four parameters.
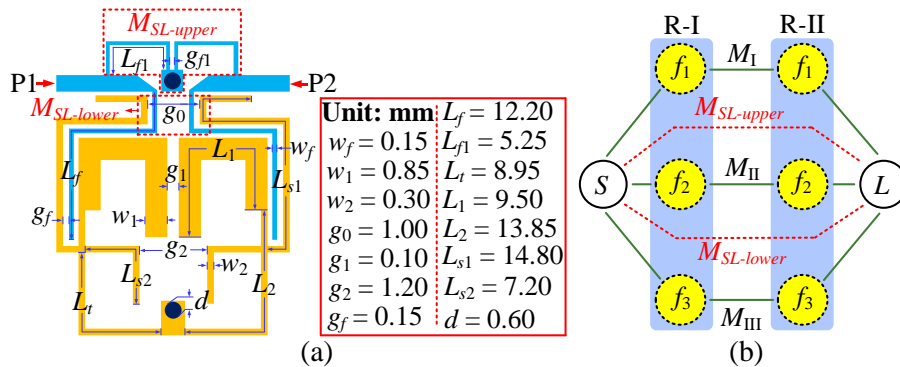
Fig. 3-26: (a) Configuration of the tri-band BPF. (b) Coupling scheme of the tri-band BPF.

On the other hand, source-loaded coupling between the feed lines of the filter are made at two places to form two coupling paths, $M_{SL-upper}$ and $M_{SL-lower}$, as shown in Fig. 3-26. As will be shown later, by employing these two source-loaded couplings, the number of transmission zeros (TZs) is significantly increased, which results in greatly improved selectivity and stopband suppression of the BPF. The tri-band BPF is designed and optimized by the EM simulator Sonnet, and its final dimensions are shown in Fig. 3-26.

Fig. 3-27: FBW characteristics of the proposed tri-band BPF: Variations of 3-dB FBWs for three passbands versus (a) d, (b) g_0, (c) g_1, (d) g_2.

3.6.3 Experimental Results and Discussion

The tri-band BPF is designed on a substrate (Rogers RO4003C) with a dielectric constant of 3.38 and thickness of 0.813 mm. A photograph of the fabricated filter is shown by the inset of Fig. 3-28, and it shows that the filter is compact with a size of $0.06\lambda_g$ × $0.15\lambda_g$, where λ_g is the guided wavelength at the centre frequency f_1 of the first passband. Moreover, the measurements were carried out using a network analyzer (E5071C, Keysight Technologies). In Fig. 3-28, it is seen that the simulated response of the filter is agree well with the measured one. The tri-band BPF operates at 1.28/3.65/5.20 GHz with respective FBWs of 7.26/9.50/5.90%, respectively. The measured minimum passband

insertion losses are 1.10/1.32/1.25 dB and return losses are better than 16/21/24 dB, respectively. The stopband rejection of two adjacent passbands are better than 15 dB and extend to $7.6f_1$. In addition, ten TZs appear at 1.19/1.47/2.28/3.98/4.72/5.50/7.58/ 8.14/8.55/9.63 GHz are produced which improve significantly both the selectivity and the stopband performance of the BPF. Most of the TZs are generated by the simultaneous use of the upper and lower source-loaded couplings, $M_{SL-upper}$ and $M_{SL-lower}$, as shown in Fig. 3-26. In Fig. 3-29, the distributions of TZs with different feed configurations are compared. It is seen that the lower S-L coupling $M_{SL-lower}$ creates $f_{z4}, f_{z5}, f_{z6}, f_{z8}, f_{z9}$ and f_{z10}, and the upper S-L coupling $M_{SL-upper}$ generates f_{z2} and f_{z3}, while the open stub with θ_{s1} and θ_{s2} produced f_{z1} and f_{z7}, respectively. With the simultaneous use of both the upper and lower S-L couplings, we get finally up to ten TZs.
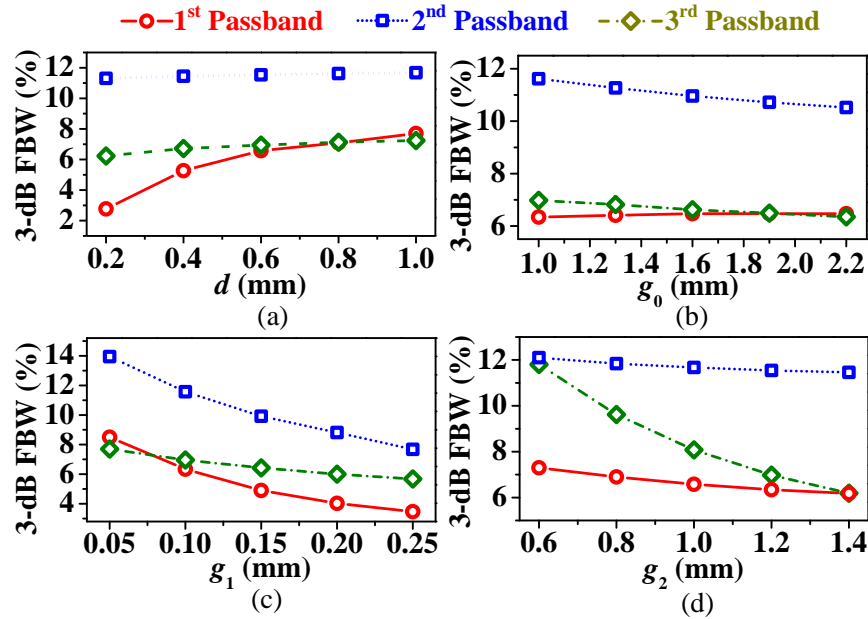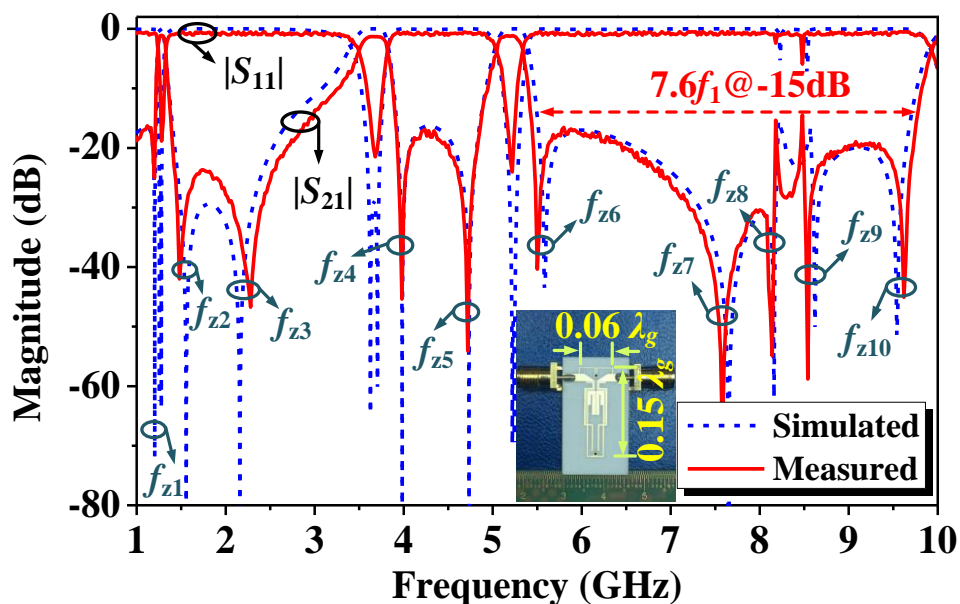

Fig. 3-28: FBW characteristics of the proposed tri-band BPF: Variations of 3-dB FBWs for three passbands versus (a) d, (b) g_0, (c) g_1, (d) g_2.
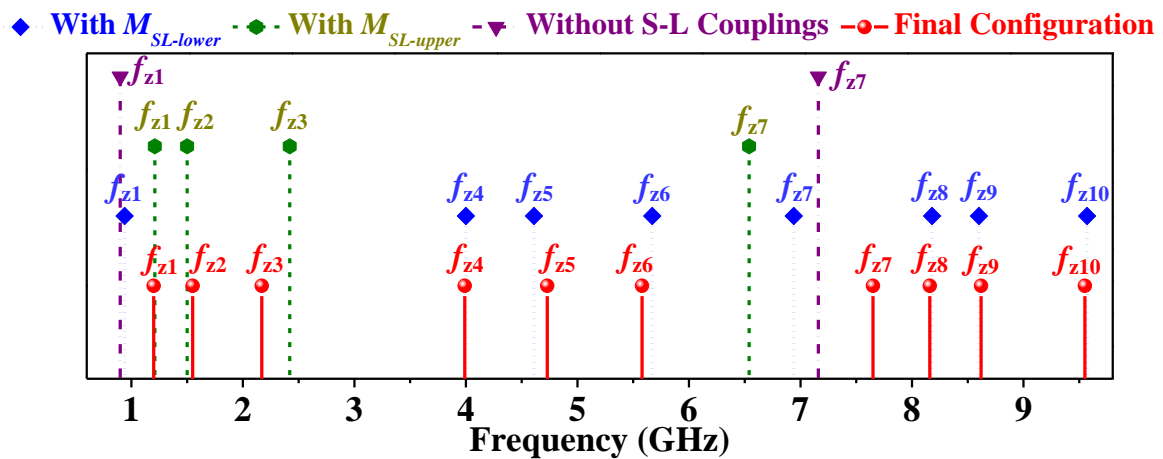
Fig. 3-29: Distribution of TZs with different feed configurations.

3.7 Miniaturized Dual-Band Bandpass Filter Using Composite Resonators with Flexible Frequency Ratio

In this section, a miniaturized DBPF is analyzed and realized with two cascaded the type two dual-resonance resonators, and a flexible frequency ratio of its dual-passband is easily achieved. Moreover, by introducing a mixed electric and magnetic coupling, a good frequency selectivity and out-band rejection performance of the DBPF is realized.

3.7.1 Implement of the Dual-Band FPD

The configuration of the DBPF is illustrated in Fig. 3-30. It consists of two composite resonators and a pair of side feeding lines. To realize the required coupling coefficients, the geometrical parameters g_1, g_{ic}, and L_{ic} are determined by simulated extraction. On the other hand, the side feeding structures with dimension L_{f1}, L_{f2}, and g_0 are adjusted to meet the demanded external quality factors. Furthermore, for purpose of enhance the selectivity of the DBPF, the common ground via-hole and interdigital capacitor structures are introduced to form a mixed electric and magnetic coupling (MEMC), which, together with the inherent transmission zeros of the composite resonators, results in three transmission zeros (TZ$_1$, TZ$_2$, and TZ$_3$), as shown in Fig. 3-31.
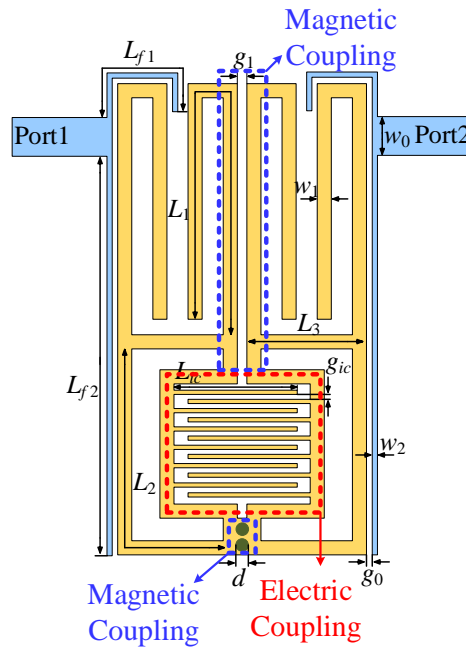
Fig. 3-30: Configuration of the proposed DBPF.

3.7.2 Experimental Results and Discussion
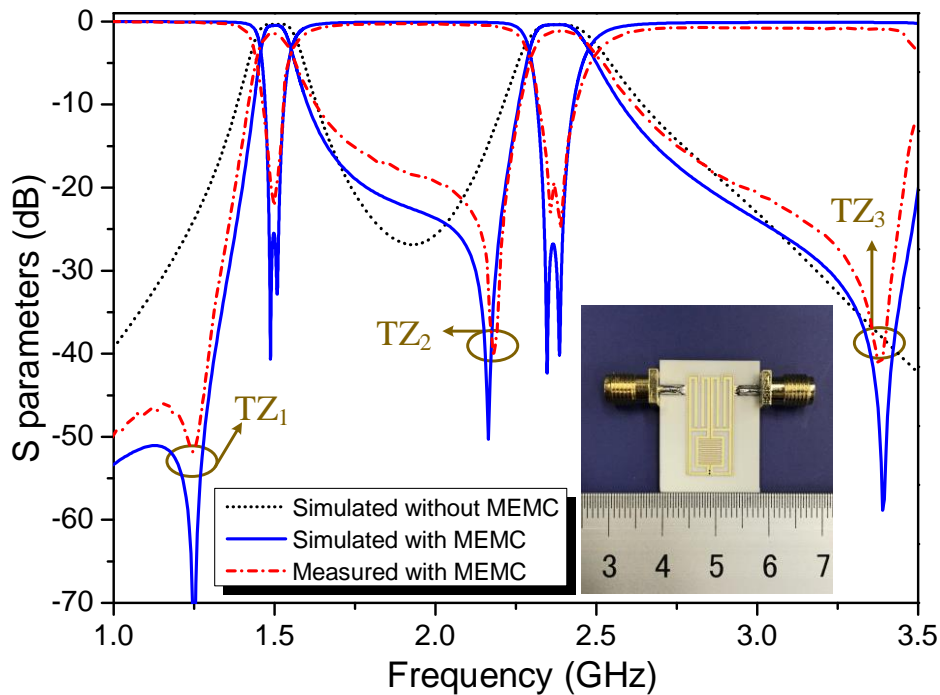
Fig. 3-31: Simulated and measured results and photograph of the fabricated DBPF.

The DBPF is fabricated on Rogers RO 4003C substrate with a relative permittivity $\varepsilon_r = 3.38$, loss tangent $\tan\delta = 0.0027$, and a thickness $h = 0.813$ mm, and the overall circuit

size is 0.06 λ_g×0.14 λ_g, where λ_g is the guided wavelength at the center frequency of the lower passband. The final dimensions of the DBPF are: L_{f1} = 6, L_{f2} = 15.2, g_0 = 0.2, L_1 = 20, L_2 = 13.5, L_3 = 3, L_{ic} = 3.95, w_0 = 1.8, w_1 = 0.5, w_2 = 0.2, g_1 = 0.15, g_{ic} = 0.2, and d = 0.4 (Unit: *mm*). Its simulated by means of the commercial softwave *Sonnet*, and measured with an *Keysight*-E5071C network analyzer. The measured results and photograph of the DBPF are shown in Fig. 3-31. As shown in Fig. 3-31, the two passbands are centered at near 1.5 GHz and 2.35 GHz, with a 3-dB fractional bandwidth of 5.96% and 7.19%, respectively. The measured minimum in-band insertion losses are 1.43 dB and 1.15 dB at the two center frequencies, respectively.

Both the return losses of the two passbands are greater than 20 dB. Moreover, the three TZs are located at 1.25 GHz, 2.19 GHz, and 3.39 GHz, respectively, which improve significantly the out-of-band suppression performance of the DBPF. Finally, Table 3.5 gives a comparison of the proposed DBPF with other reference works. It is seen that our DBPF has merits like low insertion loss and very compact circuit size.

TABLE 3.5. Comparison with previous works

Refs	Center Freq. (GHz)	3-dB FBWs (%)	IL (dB)	RL (dB)	TPs/TZs	Circuit size (λ_g ×λ_g)
[19]	2.4/5.2	6.4/5.8	1.4/1.76	15/19	8/4	0.21×0.35
[20]	2.4/5.2	9.2/9.5	1.2/2.7	15/11	4/4	0.18×0.18
[21]	1.63/2.73	7.5/5.1	1.5/2.15	17/23	8/7	0.25×0.25
[22]	2.4/5.8	4.63/3.6	1.35/1.97	17/15	4/2	0.39×0.25
This work	**1.5/2.35**	**5.96/7.19**	**1.43/1.15**	**22/20**	**4/3**	**0.06×0.14**

3.8 Conclusion

In this chapter, two type of multi-mode resonators are proposed and utilized to design four dual-band bandpass filters and a tri-band bandpass filter, respectively. The bandpass filters using stub-loaded stepped-impedance resonators have independently controllable frequencies, and the bandwidths also can be controlled by adopting multiple signal paths. Moreover, mixed electric and magnetic coupling and source and loaded coupling are introduced to produce transmission zeros to improve the selectivity and upper stopband

performance. The dual-band BPF using dual-resonance resonators has more compact size compare with other previous works. Thanks to the controllable resonance mode of the DRR, the proposed dual-band BPF has a flexible frequency ratio, which can meet different demands of communication services. Therefore, the proposed two type multi-mode resonators and a series of multi-band BPF are good candidate for high integration and low cost intelligent terminal devices.

References

[1] F. Zhu, W. Hong, J. X. Chen, and K. Wu, "Quarter-wavelength stepped-impedance resonator filter with mixed electric and magnetic coupling," *IEEE Microw. Wireless Comp. Lett.*, vol. 24, no. 2, pp. 90-92, Feb. 2014.

[2] J. S. Hong, and M. J. Lancaster, *Microwave Filters for RF/Microwave Applications*. New York: Wiley, 2011.

[3] H. W. Liu, P. Wen, Y. L. Zhao, B. P. Ren, X. M. Wang, and X. H. Guan, "Dual-band superconducting bandpass filter using quadruple-mode resonator," *IEEE Trans. Appl. Supercond.*, vol. 24, no. 2, pp. 4901204-1-4, April. 2014.

[4] J. Li, S. S. Huang, and J. Z. Zhao, "Compact dual-wideband bandpass filter using a novel penta-mode resonator (PMR)," *IEEE Microw. Wireless Comp. Lett.*, vol. 24, no. 10, pp. 668-670, Oct. 2014.

[5] H. Liu, B. Ren, X. Guan, J. Lei and S. Li, "Compact dual-band bandpass filter using quadruple-mode square ring loaded resonator (SRLR)," *IEEE Microw. Wireless Comp. Lett.*, vol. 23, no. 4, pp. 181-183, Apr. 2013.

[6] Y. Mo, K. Song, P. Tao, and Y. Fan, "Miniaturized dual-band bandpass filter using modified SIR," *Electronics Letters*, vol. 49, no. 14, pp. 888-890, Jul. 2013.

[7] W. Jiang, W. Shen, T. Wang, Y. M. Huang, Y. Peng, and G. Wang, "Compact dual-band filter using open/short stub loaded stepped impedance resonators (OSLSIRs/SSLSIRs)," *IEEE Microw. Wireless Comp. Lett.*, vol. 26, no. 9, pp. 672-674, Sep. 2016.

[8] Q. −X. Chu, and H. Wang, "A compact open-loop filter with mixed electric and magnetic coupling," *IEEE Trans. Microw. Theory Tech.*, vol. 56, no. 2, pp. 431–439, Feb. 2008.

[9] S. Yang, L. Lin, J. Chen, K. Deng, and C. −H. Liang, "Design of compact dual-band bandpass filter using dual-mode stepped-impedance stub resonators," *Electron. Lett.*, vol. 50, no. 8, pp. 611–613, Apr. 2014.

[10] W. Jiang, W. Shen, T. Wang, Y. M. Huang, Y. Peng, and G. Wang, "Compact dual-band filter using open/short stub loaded stepped impedance resonators (OSLSIRs/SSLSIRs)," *IEEE Microw. Wireless Comp. Lett.*, vol. 26, no. 9, pp. 672-674, Sep. 2016.

[11] L. Gao, and X. Y. Zhang, "High-selectivity dual-band bandpass filter using a quad-mode resonator with source-load coupling," *IEEE Microw. Wireless Compon. Lett.*, vol. 23, no. 9, pp. 474–476, Sep. 2013.

[12] H. W. Liu, P. Wen, Y. L. Zhao, B. P. Ren, X. M. Wang, and X. H. Guan, "Dual-band superconducting bandpass filter using quadruple-mode resonator," *IEEE Trans. Appl. Supercond.*, vol. 24, no. 2, pp. 4901204-1-4, Apr. 2014.

[13] Z. −C. Zhang, Q. −X. Chu, and F. −C. Chen, "Compact dual-band bandpass filters using open-/short-circuited stub-loaded λ/4 resonators," *IEEE Microw. Wireless Compon. Lett.*, vol. 25, no. 10, pp. 657–659, Oct. 2015.

[14] L. −C. Tsai, and C. −W. Hsue, "Dual-band bandpass filters using equal-length coupled-serial-shunted lines and Z-transform technique," *IEEE Trans. Microwave Theory Tech.*, vol. 52, no. 4, pp. 1111-1117, Apr. 2004.

[15] Y. Liu, and W. Dou, "Miniature dual-band filters sing integrated bandpass and bandstop filters for wide bandwidths," *IEICE Electron. Express*, vol. 6, no. 10, pp. 618-622, May, 2009.

[16] G. −L. Dai, Y. −X. Guo, and M. −Y. Xia, "Dual-band bandpass filter using parallel short-ended feed scheme," *IEEE Microw. Wireless Compon. Lett.*, vol. 20, no. 6, pp. 325-327, Jun. 2010.

[17] S. J. Maleki, and M. Dousti, "A compact dual-band bandpass filter using microstrip meander loop and square loop resonators," *IEICE Electron. Express*, vol. 9, no. 16, pp. 1342-1348, Aug. 2012.

[18] S. Zhang, and L. Zhu, "Compact split-type dual-band bandpass filter based on λ/4 resonators," *IEEE Microw. Wireless Compon. Lett.*, vol. 23, no. 7, pp. 344-346, Jul. 2013.

[19] J. M. Yan, L. Z. Cao, J. Xu, and R. S. Chen, "Design of a fourth-order dual-band bandpass filter with independently controlled external and inter-resonator coupling," *IEEE Microw. Wirel. Compon. Lett.*, vol. 25, no. 10, pp. 642-644, Oct. 2015.

[20] J. L. Xu, G. Zhang, Y. –M. Tang, and Y. –M. Bo, "Compact dual-mode dual-band bandpass filter with wide stopband for WLAN applications," *Electron. Lett.*, vol. 51, no. 17, pp. 1372-1374, Aug. 2015.

[21] W. Jiang, W. Shen, T. Wang, Y. M. Huang, Y. Peng, and G. Wang, "Compact dual-band filter using open/short stub loaded stepped impedance resonators (OSLSIRs/SSLSIRs)," *IEEE Microw. Wirel. Compon. Lett.*, vol. 26, no. 9, pp. 672-674, Sep. 2016.

[22] Z. –C. Zhang, Q. –X. Chu, and F. –C. Chen, "Compact dual-band bandpass filters using open-/short-circuited stub-loaded λ/4 resonators," *IEEE Microw. Wirel. Compon. Lett.*, vol. 25, no. 10, pp. 657-659, Oct. 2015.

Chapter 4

Dual-Band Filtering Power Divider Using Dual-Resonance Resonators with Ultra-Wide Stopband

4.1 Overview

In modern wireless communication systems, power dividers (PDs) and bandpass filters (BPFs) are essential passive components. Recently, to meet the high integration and low loss requirements, filtering power dividers (FPDs) and other composite function components are attracting great attention. Most of the previously reported works tried to achieve high frequency selectivity [4], [9] and harmonic suppression [3], [5] performances in a single-band or a wideband, yet there are a few papers on dual-band FPDs (DB-FPDs) [1], [2], [6] - [8]. These DB-FPDs exhibited good frequency selectivity and power division. However, their harmonic suppression property needs to be improved.

In this chapter, we propose a novel DB-FPD with ultrawide stopband and good isolation. It consists of a small U-shaped Wilkinson power divider, two pairs of dual-resonance resonators (DRRs), and a pair of spur-lines. With the simultaneous use and appropriate design of the coupled feedlines, mixed electric and magnetic couplings between the DRRs, and spur-lines with different lengths, multiple TZs are produced which result in two passbands with desired power division, high frequency selectivity, good isolation, and an ultrawide stopband. A prototype DB-FPD operating at 2.3 and 3.5 GHz with 3-dB fractional bandwidths of 8% and 6% is designed, fabricated and measured. The measured responses agree well with the design simulations, exhibiting a stopband up to 13.8 GHz ($6f_0$) with 20-dB rejection level. This is the widest stopband of DB-FPDs reported thus far, as shown by the comparison in the following part.

4.2 Analysis of the Stepped-Impedance DRR

The microstrip configuration of the proposed DRR is given in Fig. 4-3, and Fig. 4-1(a) depicts its transmission line model. The simplified even-mode and odd-mode circuits of the DRR are drawn in Fig. 4-1(b) and (c), respectively. The DRR is open-circuited at one end and short-circuited at the opposite end. The even-mode and odd-mode surface current distributions of the microstrip DRR are shown in Fig. 4-1(d) which revel that:
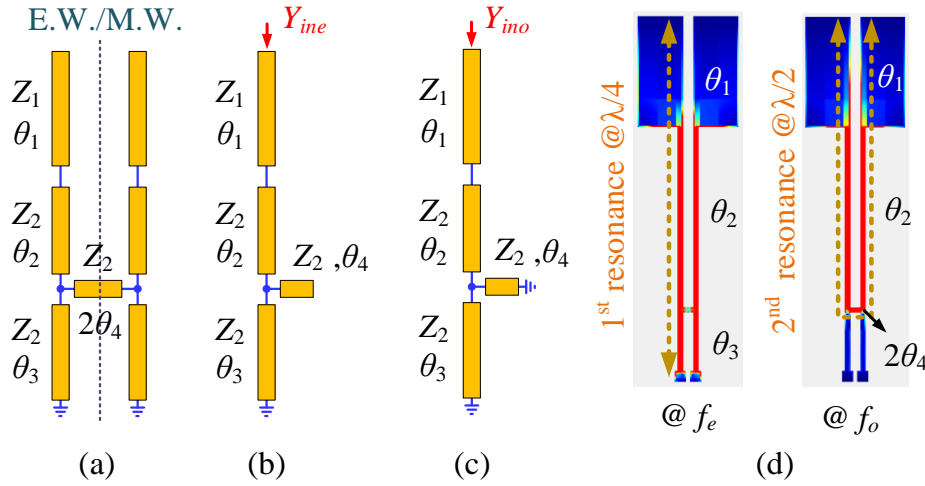
Fig. 4-1: (a) Transmission line model of the proposed DRR. (b) Even-mode model. (c) Odd-mode model. (d) Even-mode and odd-mode current distributions under week excitations.

(1) The even-mode resonance f_e is basically the quarter- wavelength resonance occurred at the line with an electrical length of $\theta_1 + \theta_2 + \theta_3$, and the line θ_4 has little effect on f_e.

(2) The odd-mode resonance f_o is basically the half- wavelength resonance occurred at the folded line with an electrical length of $\theta_1 + \theta_2 + 2\theta_4 + \theta_2 + \theta_1$, and the line θ_3 has little effect on f_o.

So, the analysis of the even-mode and odd-mode circuits in Fig. 4-1(b) and (c) are simplified when we neglect the line θ_4 in Fig. 4-1(b) and neglect the line θ_3 in Fig. 4-1(c). Then, the input admittance, Y_{ine} and Y_{ino} as shown in Fig. 4-1(b) and (c), of the even- and odd-mode equivalent circuits can be derived as:

$$Y_{ine} = \frac{R - \tan\theta_1 \tan\left(\theta_2 + \theta_3\right)}{jRZ_2\left[R\tan\theta_1 + \tan\left(\theta_2 + \theta_3\right)\right]} \tag{4.1}$$

$$Y_{ino} = \frac{R - \tan\theta_1 \tan(\theta_2 + \theta_4)}{jRZ_2\left[R\tan\theta_1 + \tan(\theta_2 + \theta_4)\right]} \tag{4.2}$$

where the impedance ratio $R = Z_1/Z_2$, Z_1, Z_2, and θ_i ($i = 1, 2, 3, 4$) are the characteristic impedances and electrical lengths of the corresponding line sections of the DRR, respectively. When $Y_{ine} = 0$ or $Y_{ino} = 0$, we get the equation for determining the resonant frequency of the even- or odd-mode as follows

$$\tan\left[(1-\alpha_1)\theta_{T1}\right]\tan(\alpha_1\theta_{T1}) = R \qquad @ f_e \tag{4.3}$$

$$\tan\left[(1-\alpha_2)\theta_{T2}\right]\tan(\alpha_2\theta_{T2}) = R \qquad @ f_o \tag{4.4}$$

where $\theta_{T1} = \theta_1 + \theta_2 + \theta_3$, $\theta_{T2} = \theta_1 + \theta_2 + \theta_4$. $\alpha_1 = \theta_1/\theta_{T1}$ and $\alpha_2 = \theta_1/\theta_{T2}$ are electrical length ratios of the even-mode and odd-mode, respectively.
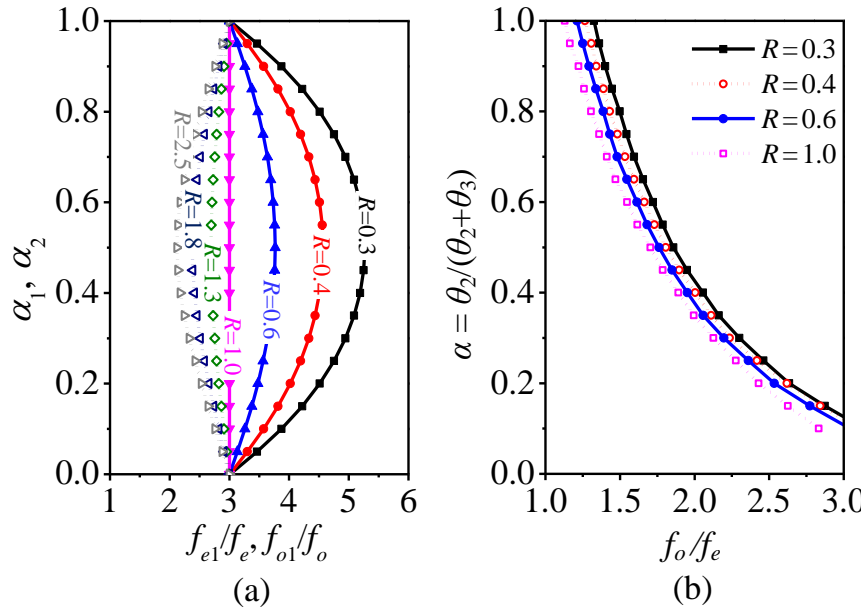
Fig. 4-2: (a) Normalized ratios of the first spurious mode frequency to the fundamental resonant frequency (f_{e1}/f_e & f_{o1}/f_o) with different electrical lengths and impedance ratios. (b) The frequency ratio f_o/f_e with different α.

From (4.3) and (4.4), it is obvious that the resonant frequencies of the even- and odd-modes vary with the impedance ratio R and the electrical length ratios α_1 and α_2. Fig. 4-2(a) depicts the variation of the first harmonic mode f_{e1} and f_{o1} normalized by the fundamental mode f_e and f_o under various combinations of R and α_1 or α_2. The curves show that with appropriate choose of R, α_1, and α_2, we can get the maximum values of

f_{e1}/f_e and f_{o1}/f_o, meaning the maximally widened upper stopband [10].

It is worth to note that (4.3) and (4.4) also reveal that the two resonant frequencies f_e and f_o can be controlled independently by varying θ_3 and θ_4, respectively. Fig. 4-2(b) illustrates the frequency ratio f_o/f_e of the two fundamental modes of the DRR versus the electrical length ratio $\alpha = \theta_2 / (\theta_2 + \theta_3)$, from which it is seen that the frequency ratio f_o/f_e can be designed flexibly with a value ranging from 1 to 3.

4.3 Dual-Band Filtering Power Divider Design

Fig. 4-3 shows the configuration of the proposed FPD, which consists of a small WPD with its two U-shaped quarter-wavelength arms connected with two pairs of DRRs. The fundamental even- and odd-mode of the DRRs, as will be discussed later, are used to form two passbands of the dual-band FPD. The signal transmitting paths of the DB-FPD is shown in Fig. 4-4. Mixed electric and magnetic coupling between the DRRs are introduced to produce transmission zeros (TZs) around the two passbands and improve thereby their frequency selectivity. Moreover, a pair of spur-lines with different lengths are embedded into the U-shaped quarter-wavelength transmission lines, as shown in Fig. 4-3, to enhance the harmonic suppression and widen the stopband of the DB-FPD. Detailed analysis is given below.
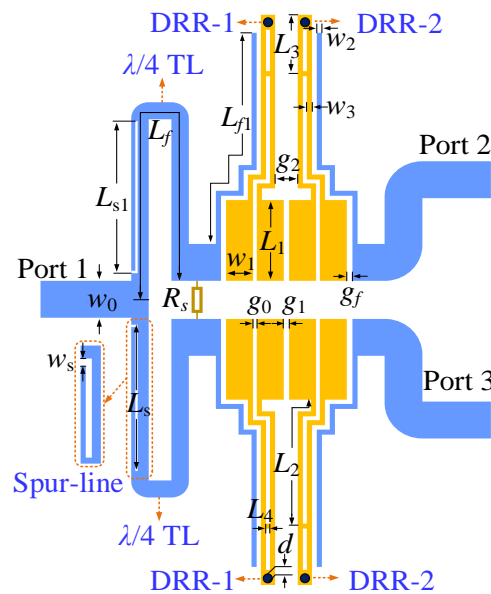
Fig. 4-3: Configuration of the proposed DB-FPD.
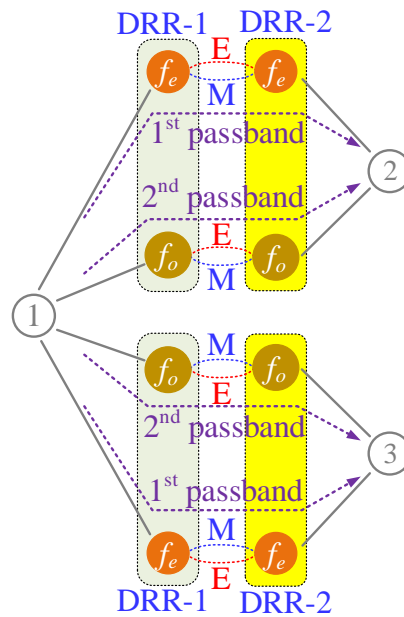
Fig. 4-4: Signal transmitting paths of the proposed DB-FPD.

4.3.1 Design Procedure of the Dual-Band FPD

Based on the above analysis, the design procedure of the proposed DB-FPD is summarized as follows.

(1) Specify the resonant frequencies f_e and f_o, the fractional bandwidths Δ_1 and Δ_2, and the harmonic frequencies f_{e1} and f_{o1}.

(2) Determine the impedance ratio R, the electrical length ratio α_1 and α_2, and the total electrical lengths θ_{T1} and θ_{T2}, using the equation (4.3) and (4.4).

(3) From the center frequencies f_e, f_o, and the fractional bandwidths Δ_1, Δ_2, determine the corresponding external quality factors Q_{e1}, Q_{e2}, and coupling coefficients M_I, M_{II}, of the two passbands, using the well-known classic BPF design formulas.

(4) Refer [11] to design a traditional WPD, which bandwidth should be cover the two passbands of the dual-band BPF. And then, add two extension feedlines (L_{f1}) at the two output ports of WPD to exciting the DRRs to achieve frequency selectivity.

(5) The feed lines (L_{f1}, g_f) and coupling gaps (g_1, g_2) control the external quality factor and coupling coefficients of the dual-band BPF, respectively. In step (3), the corresponding external quality factors Q_{e1}, Q_{e2}, and coupling coefficients M_I, M_{II} of the two passbands are calculated. And then used simulation method to extract the different

external quality factors of two passbands with varying the physical size of feed lines (L_{f1}, g_f), according to formula (4.5) [12]. After that, we obtain extracted external quality factor graph with different L_{f1} and g_f. With this graph, we can choose appropriate L_{f1} and g_f to meet the Q_{e1} and Q_{e2} at the same time. In a similarly, the value of coupling gaps can be determined based on formula (4.6).

$$Q_e = \frac{f_0}{\Delta f_{\pm 90^o}} \tag{4.5}$$

$$M = \pm \frac{f_{p2}^2 - f_{p1}^2}{f_{p2}^2 + f_{p1}^2} \tag{4.6}$$

(6) Finally, simulate the frequency response of the finally obtained DB-FPD using an electromagnetic simulator.

Summarizing above design procedure, firstly, we used coupling matrix to synthesize the dual-band bandpass filter in Fig. 4-5, which simulation result is shown in Fig. 4-6. Secondly, we design a wideband Wilkinson power divider, which bandwidth should be covering the two passbands of the dual-band bandpass filter. Finally, the dual-band bandpass filters are inserted into the two output arms of the Wilkinson power divider, and then optimize the design of the final filtering power divider.
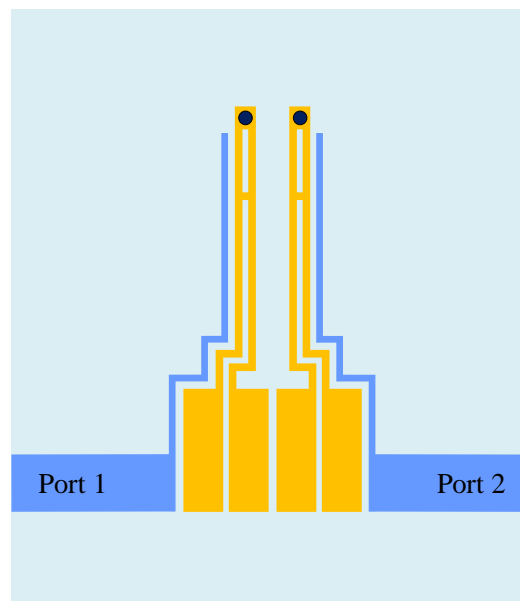
Fig. 4-5: The layout of the dual-band bandpass filter.
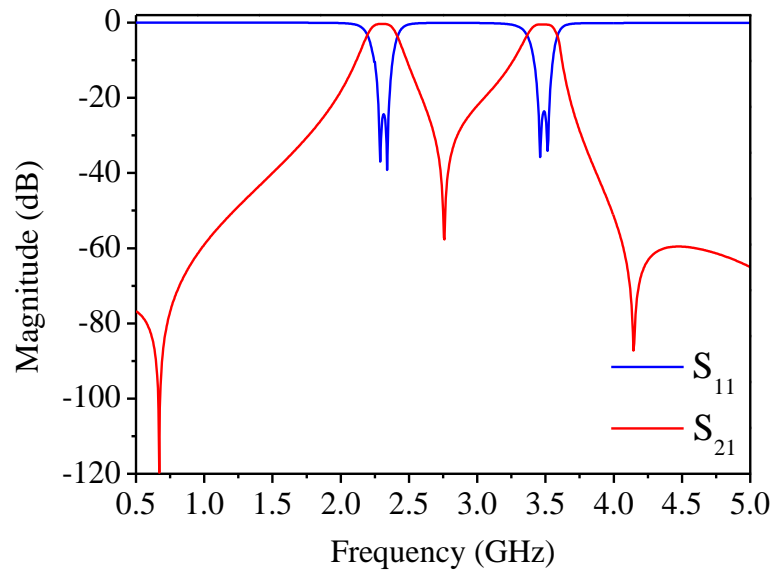
Fig. 4-6: The simulated response of the dual-band bandpass filter.

4.3.2 Analysis of the Ultrawide Stopband Performance
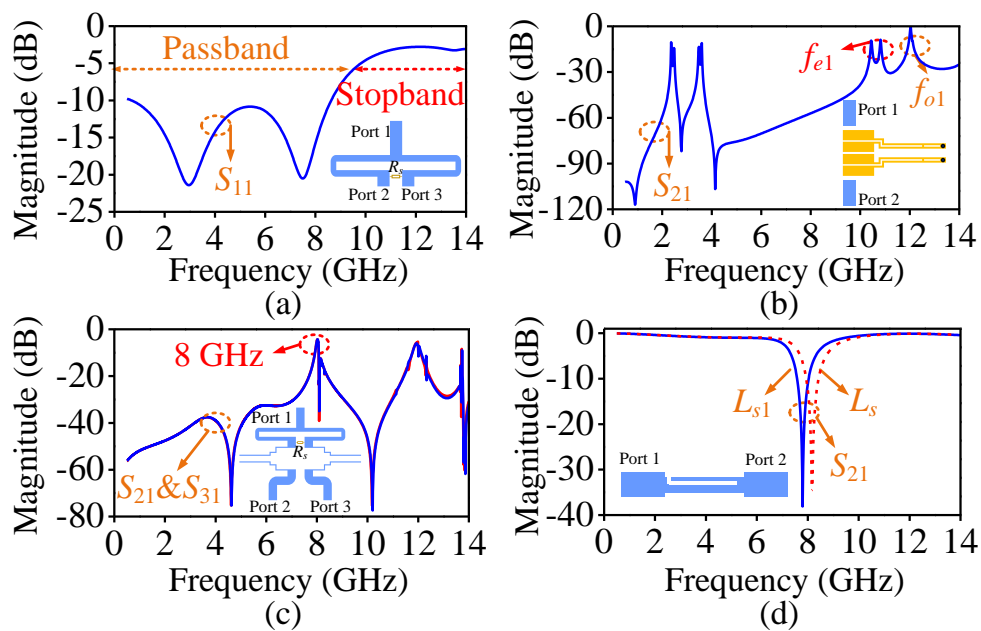
Fig. 4-7: Simulated responses of different parts of the proposed DB-FPD. (a) S_{11} the Wilkinson PD. (b) S_{21} of the DRRs under weak coupling. (c) S_{21} and S_{31} of the DB-FPD excluding the DRRs. (d) S_{21} of the spur-line with a length of L_{s1} (solid line) and a length of L_s (broken line).

Fig. 4-7 illustrates the simulated responses of different parts of the proposed DB-FPD. Fig. 4-7(a) is the S_{21} the Wilkinson PD, and Fig. 4-7 (b) is the S_{21} of the DRRs under

weak coupling. The spurious resonances of the DRRs occur at frequencies above 10 GHz, which are located at the stopband of Wilkinson PD. On the other hand, the S_{21} and S_{31} of the DB-FPD excluding the DRRs is given in Fig. 4-7(c), which exhibit extra resonances at about 8 GHz. In order to suppress these resonances and obtain a good notch performance, a pair of spur-lines with unequal length of L_s and L_{s1} is embedded into the U-shaped quarter-wavelength lines of the WPD as shown in Fig. 4-3(a). These spur-lines with different lengths are designed to create two transmission zeros around 8 GHz, as shown in Fig. 4-7(d), to suppress the aforementioned extra resonances around 8 GHz in Fig. 4-7(c).

4.3.3 Experimental Results and Discussion
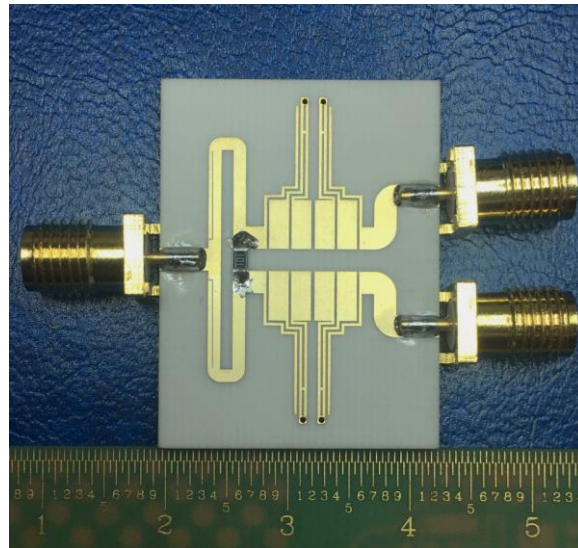
Fig. 4-8: Photograph of the proposed dual-band FPD.

To verify the design method, a DB-FPD is developed on a Rogers RO4003 substrate, with a relative dielectric constant of 3.38 and a thickness of 0.813 mm. The dimensions of the circuit are given in Fig. 4-11 with R_s = 100 Ω. The photograph of the fabricated DB-FPD is shown by the inset of Fig. 4-8. In addition, measurements were done using a network analyzer of Keysight-E5071C.

The simulated and measured results in Fig. 4-11(a) and (b) show a good agreement. The measured center frequencies of the two passbands are 2.3 and 3.5 GHz with 3-dB FBWs of 9.0% and 7.1%, respectively. In the two passbands, the measured insertion loss

(IL) is less than 4.2 dB and 4.5 dB, and the return loss (RL) is larger than 17.6 dB and 21.4 dB, respectively. The measured isolation between Port 2 and Port 3 (Iso.) of the two passbands are higher 19.2 dB and 18.6 dB, respectively. Four transmission zeros (TZs) are produced at 0.9, 2.8, 4.2, and 5.8 GHz, respectively, resulting in a very high frequency selectivity. Because of the coexistence of the mixed electric and magnetic couplings can also build up a pair of opposite coupling paths, which can produce a transmission zero. In Fig. 4-10 the inner mixed electric and magnetic couplings of DRR in Fig. 4-9(a), generate the third transmission zeros. The first transmission zero produced by the coupling between sources and loaded, which is built by the DRR act as coupling "bridge". Moreover, the mixed electric and magnetic couplings between two DRRs in Fig. 4-9(b) is generate the second transmission zero. The fourth transmission zero is produced by the Wilkinson PD with folded coupled feed lines, as shown by Fig. 4-7(c). The proposed DB-FPD with appropriately designed DRRs but without the spur-lines exhibited harmonic suppression larger than 20 dB over a wide frequency range from 0.5 to 7.5 GHz (3.3 f_o). By adding the spur-lines, the upper stopband with 20 dB rejection level is widened to 13.8 GHz ($6f_o$) in Fig. 4-11(b).
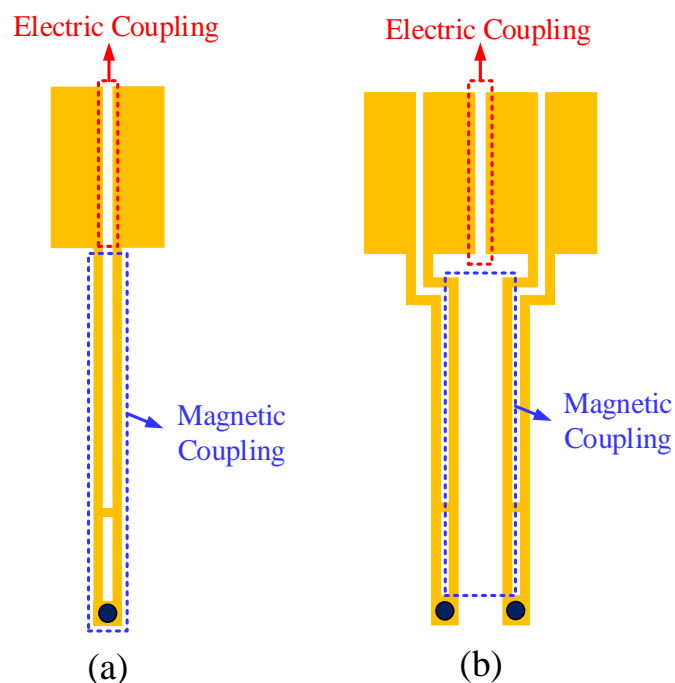
Fig. 4-9: The mixed electric and magnetic couplings of the (a) Inner of DRR, (b) Between two DRRs.
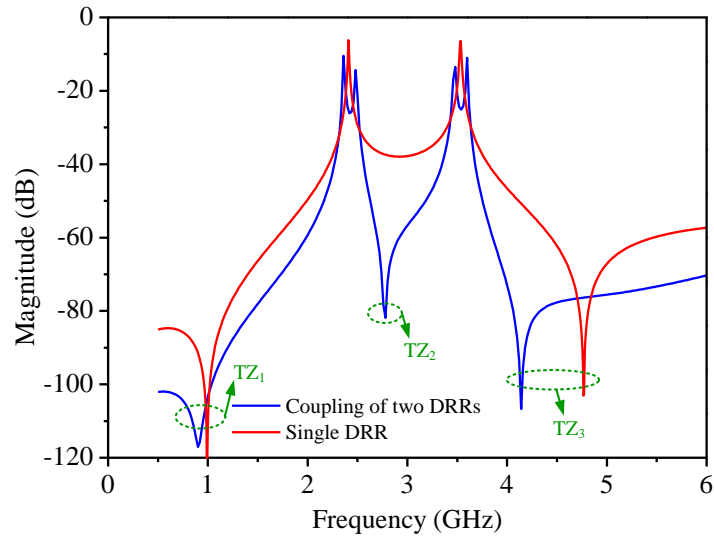
Fig. 4-10: The responses of coupling of two DRRs and single DRR under weak coupling excitation.

(a)

(b)
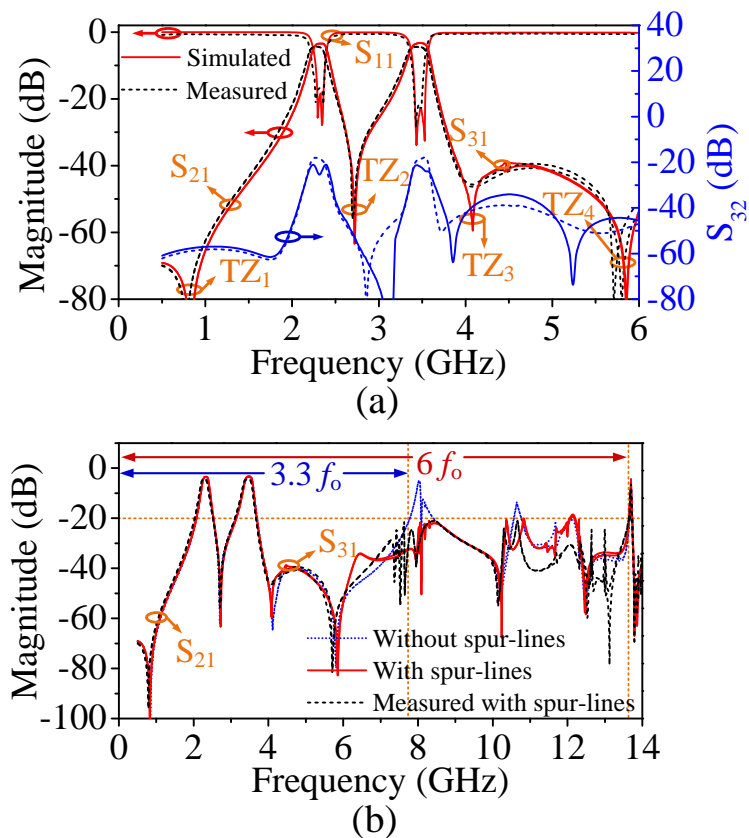
Fig. 4-11: Simulated and measured results of the DB-FPD: (a) Magnitude of S_{11}, S_{21}, S_{31}, and S_{32}. (b) Ultrawide stopband performance of the proposed FPD. Dimensions of the circuit are L_1 = 4.0, L_2 = 6.5, L_3 = 2.1, L_4 = 0.2, L_f = 17.2, L_{f1} = 12.3, L_s = 6.0, L_{s1} = 6.5, w_0 = 1.8, w_1 = 1.6, w_2 = 0.2, w_3 = 0.2, w_s = 0.2, g_0 = 0.2, g_1 = 0.3, g_2 = 0.9, g_f = 0.2, and d = 0.4. (Unit: mm).

TABLE 4.1. Comparison with previous works

Refs.	f_{c1}/f_{c2} (GHz)	IL (dB)	Stopband	TZs	Iso. (dB)	Circuit size ($\lambda_g \times \lambda_g$)
[1]	1.8/2.96	3.8/3.9	~2.67f_0	3	26/20	0.43×0.49
[2]	0.9/2.1	3.2/3.4	~3.4f_0	2	35/25	0.26×0.20
[6]	1.57/2.89	3.9/4.1	~3.89f_0	5	21/25	0.52×0.28
[8]	2.3/3.64	3.8/4.2	~2.6f_0	3	18/18	0.54×0.38
This work	**2.3/3.5**	**4.2/4.5**	**~6f_0**	**4**	**19/19**	**0.37×0.28**

In the end, a performance comparison of the proposed DB-FPD with other reported DB-FPDs is shown in Table 4.1. It indicates that the current DB-FPD exhibits not only good isolation and compact size but also an ultrawide stopband.

4.4 Conclusion

A novel DB-FPD with compact size and high performance was developed by cascading a Wilkinson PD with two pairs of well-designed DRRs. The simultaneous use and appropriate design of the coupled feedlines, mixed electric and magnetic couplings between DRRs, and spur-lines with different lengths produced multiple TZs which result in two passbands with desired power division, high frequency selectivity, good isolation, and an ultrawide stopband.

References

[1] Y. C. Li, Q. Xue, and X. Y. Zhang, "Single- and dual-band power dividers integrated with bandpass filters," *IEEE Trans. Microw. Theory Techn.*, vol. 61, no. 1, pp. 69–76, Jan. 2013.

[2] C. Shao, Y. Li, and J. –X. Chen, "Compact dual-band microstrip filtering power divider using T-junction structure and quarter-wavelength SIR," *Electron. Lett.*, vol. 53, no. 6, pp. 434–436, Mar. 2017.

[3] Y. Wang, X. Y. Zhang, F. –X. Liu, and J. –C. Lee, "A compact bandpass Wilkinson power divider with ultra-wide band harmonic suppression," *IEEE Microw. Wireless Compon. Lett.*, vol. 27, no. 10, pp. 888–890, Oct. 2017.

[4] G. Zhang, X. D. Wang, J. -S. Hong, and J. Q. Yang, "A high- performance dual-mode filtering power divider with simple layout," *IEEE Microw. Wireless Compon. Lett.*, vol. 28, no. 2, pp. 120–122, Feb. 2018.

[5] X. Y. Zhang, K. X. Wang, and B. J. Hu, "Compact filtering power divider with enhanced second-harmonic suppression," *IEEE Microw. Wireless Compon. Lett.*, vol. 23, no. 9, pp. 483–485, Sep. 2013.

[6] G. Zhang, J. P. Wang, L. Zhu, and W. Wu, "Dual-band filtering power divider with high selectivity and good isolation," *IEEE Microw. Wireless Compon. Lett.*, vol. 26, no. 10, pp. 774–776, Oct. 2016.

[7] Y. L. Wu, Z. Zhuang, G. Y. Yan, Y. A. Liu, and Z. Ghassemlooy, "Generalized dual-band unequal filtering power divider with independently controllable bandwidth," *IEEE Trans. Microw. Theory Techn.*, vol. 65, no. 10, pp. 3838–3848, Oct. 2017.

[8] X. D. Wang, J. P. Wang, G. Zhang, J. -S. Hong, and W. Wu, "Dual-wideband filtering power divider with good isolation and high selectivity," *IEEE Microw. Wireless Compon. Lett.*, vol. 27, no. 12, pp. 1071–1073, Dec. 2017.

[9] X. Wang, J. Wang, and G. Zhang, "Design of wideband filtering power divider with high selectivity and good isolation," *Electron. Lett.*, vol. 52, no. 16, pp. 1389–1391, Aug. 2017.

[10] S. –J. Sun, T. Su, K. Deng, B. Wu, and C. –H. Hong, "Shorted-ended stepped-impedance dual-resonance resonator and its application to bandpass filters," *IEEE Trans. Microw. Theory Techn.*, vol. 61, no. 9, pp. 3209–3215, Sep. 2013.

[11] E. J. Wilkinson, "An N-way hybrid power divider," *IEEE Trans. Microw. Theory Techn.*, vol. 8, Issue 1, pp. 116–118, Jan. 1960.

[12] J. S. Hong, and M. J. Lancaster, *Microwave Filter for RF/Microwave Application*. New York, USA: Wiley, 2001.

Chapter 5

Balanced-to-Unbalanced Filtering Power Dividers Using Multi-Mode Resonators with Variable Bandwidth

5.1 Overview

Balanced-to-unbalanced (BTU) circuits are widely utilized to connect the balanced port and single-ended ports with common-mode noise suppression, in modern wireless communication systems. To meet the requirements of conversion between balanced signal and unbalanced signal, high immunity to environment, and integrate multifunction design, many attentions have been focused on the BTU and balun microwave components, such as balun filters [1–3], BTU diplexers [4–6], and BTU power dividers (PDs) [7–21].

For BTU PD, there are integration balun and power divider in one component to combine single-end signals from receiving antenna array (Rx antenna array) into differential signals for differential low noise amplifiers (DLNAs), or vice versa. Over the past several years, BTU PDs have been studied based on square ring network as shown in Fig. 5-1 [7-14]. In [7], shorted-ended four-wire coupled-line and T-shaped structure were used to design a BTU PD with operating bandwidth of 25% for the first time. In order to enhance the operating bandwidth, three pairs of cascaded coupled-lines replaces the shorted-ended four-wire coupled-line, T-shaped structure and other transmission lines. Thus, the operating bandwidths are broadened to 37.2% [8] and 30% [11]. Moreover, those designs also realize a miniaturized circuit size. In [13], a multilayer structure was adopted to further enhance the bandwidth of BTU PD. Despite the power division response with the bandwidth of 63% was achieved, the multilayer structure is difficult to fabricate. A wideband BTU FD using symmetrical transmission lines was presented in [14], and the bandwidth can be raised to 89.1%. All of these previous works payed attention to BTU PDs design, which still need to connect filters in system applications. Therefore, BTU filtering power divider (FPD) with higher integration had been proposed

based on branch-lines with several open-stubs [15], which is used to implement lower insertion loss and smaller circuit size. A pair of coupled-lines are utilized to realize filtering response with wideband performance [16]. Moreover, open/shorted coupled-lines and half-wavelength open stubs were applied to introduce two transmission zeros near the passband, which enhance the selectivity of the proposed BTU FPD, while the in-band isolation also need to further improve. In [17], the in-band isolation better than 20 dB is realized based on branch lines and the modified two-port coupled-lines with short- and open-circuit stubs. For widening the frequency range of common mode (CM) suppression, hybrid microstrip/slotline structure was used to design a filtering BTU PD (BTU FPD) with wider differential mode (DM) matching bandwidth and wider CM suppression bandwidth [19]. Despite this structure can achieve a better CM suppression, it is relatively difficult and expensive to process. Note that all the aforementioned works focus on how to design wideband BTU PDs more or less, and only limited works have been done on the designs of variable bandwidth [15], [16] or narrowband [18].

In this chapter, the stub-loaded dual-mode resonator (SL-DMR) with controllable resonant frequency and an intrinsic transmission zero is adopted to design BTU FPDs for the first time. The designs of this chapter not only achieved controllable operating frequency and high selectivity, but also have a big variable range of the bandwidth from narrowband to wideband. The remainder of this chapter is organized as follows. The mixed-mode scattering matrix is analyzed, thus the final condition of better DM matching, high isolation and deeper CM suppression are obtained. Secondly, based on even-mode and odd-mode analysis method, the closed-form analytical equations, detail design procedure and key parameters study is synthetically analyzed. Then, to realize the characteristic of variable bandwidth, two situations of bandwidth controllability are provided. Next, in order to demonstrate the design method of BTU FPD, a BTU FPD with one transmission zero is implemented and their responses are also discussed. Moreover, for enhancing the selectivity of the proposed BTU FPD, another BTU FPD structure based on a coupled-line branch line (CBL), which can generate multiple transmission zeros distributing on the both sides of the passband, is implemented. Finally, a conclusion is given at the end of this chapter.

5.2 Analysis of the Mixed-Mode Scattering Matrix of Balanced-to-Unbalanced Network
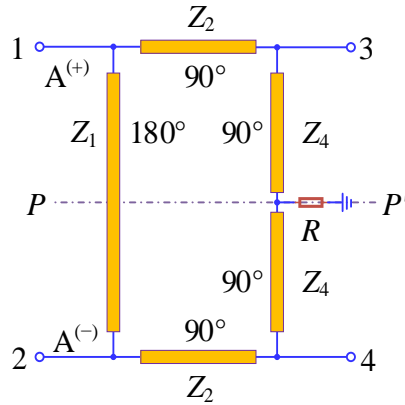
Fig. 5-1: Circuit model of the typical four-port balanced-to-unbalanced power divider.

Fig. 5-1 depicts the typical circuit model of the balanced-to-unbalanced filtering power divider. It is a four ports reciprocal network which is including a pair of differential input ports $A^{(+)}$ and $A^{(-)}$ (port 1 and port 2), two-single ended ports 3 and 4, four microstrip branch lines, and a resistor. In this section, theoretical and simulation analysis are given out to explore the operating principle of the proposed three structures, respectively. Finally, the design procedure is summarized.

The ideal standard matrix (S_{std}) of the four ports reciprocal network exhibited in Fig. 5-1, can be defined as

$$S_{std} = \begin{bmatrix} S_{11} & S_{13} & S_{12} & S_{14} \\ S_{31} & S_{33} & S_{32} & S_{34} \\ S_{21} & S_{23} & S_{22} & S_{24} \\ S_{41} & S_{43} & S_{42} & S_{44} \end{bmatrix} = \begin{bmatrix} S_{A^{(+)}A^{(+)}} & S_{A^{(+)}3} & S_{A^{(+)}A^{(-)}} & S_{A^{(+)}4} \\ S_{3A^{(+)}} & S_{33} & S_{3A^{(-)}} & S_{34} \\ S_{A^{(-)}A^{(+)}} & S_{A^{(-)}3} & S_{A^{(-)}A^{(-)}} & S_{A^{(-)}4} \\ S_{4A^{(+)}} & S_{43} & S_{4A^{(-)}} & S_{44} \end{bmatrix} \quad (5.1)$$

The mixed-mode scattering matrix (S_{mm}) of the proposed balanced-to-unbalanced filtering power divider can be derived from the standard matrix (S_{std}) using the matrix transformation as bellow [22]

$$S_{mm} = M S_{std} M^{-1} \quad (5.2a)$$

where

$$\boldsymbol{M} = \frac{1}{\sqrt{2}} \begin{bmatrix} 1 & -1 & 0 & 0 \\ 1 & 1 & 0 & 0 \\ 0 & 0 & \sqrt{2} & 0 \\ 0 & 0 & 0 & \sqrt{2} \end{bmatrix} \tag{5.2b}$$

Combining (5.1) and (5.2), the mixed-mode scattering matrix ($\boldsymbol{S}_{mm}$) can be derived as:

$$\boldsymbol{S}_{mm} = \begin{bmatrix} S_{dd11} & S_{ds13} & S_{dc11} & S_{ds14} \\ S_{sd31} & S_{ss33} & S_{sc31} & S_{ss34} \\ S_{cd11} & S_{cs13} & S_{cc11} & S_{cs14} \\ S_{sd41} & S_{ss43} & S_{sc41} & S_{ss44} \end{bmatrix} \tag{5.3}$$

$$S_{dd} = \frac{1}{2} \begin{bmatrix} S_{dd11} = \left(S_{A^{(+)}A^{(+)}} - S_{A^{(+)}3} - S_{3A^{(+)}} + S_{33} \right) & S_{dd12} = \left(S_{A^{(+)}A^{(-)}} - S_{A^{(+)}4} - S_{3A^{(-)}} + S_{34} \right) \\ S_{dd21} = \left(S_{A^{(-)}A^{(+)}} - S_{A^{(-)}3} - S_{4A^{(+)}} + S_{43} \right) & S_{dd22} = \left(S_{A^{(-)}A^{(-)}} - S_{A^{(-)}4} - S_{4A^{(-)}} + S_{44} \right) \end{bmatrix} \tag{5.4a}$$

$$S_{dc} = \frac{1}{2} \begin{bmatrix} S_{dc11} = \left(S_{A^{(+)}A^{(+)}} + S_{A^{(+)}3} - S_{3A^{(+)}} - S_{33} \right) & S_{dc12} = \left(S_{A^{(+)}A^{(-)}} + S_{A^{(+)}4} - S_{3A^{(-)}} - S_{34} \right) \\ S_{dc21} = \left(S_{A^{(-)}A^{(+)}} + S_{A^{(-)}3} - S_{4A^{(+)}} - S_{43} \right) & S_{dc22} = \left(S_{A^{(-)}A^{(-)}} + S_{A^{(-)}4} - S_{4A^{(-)}} - S_{44} \right) \end{bmatrix} \tag{5.4b}$$

$$S_{cd} = \frac{1}{2} \begin{bmatrix} S_{cd11} = \left(S_{A^{(+)}A^{(+)}} - S_{A^{(+)}3} + S_{3A^{(+)}} - S_{33} \right) & S_{cd12} = \left(S_{A^{(+)}A^{(-)}} - S_{A^{(+)}4} + S_{3A^{(-)}} - S_{34} \right) \\ S_{cd21} = \left(S_{A^{(-)}A^{(+)}} - S_{A^{(-)}3} + S_{4A^{(+)}} - S_{43} \right) & S_{cd22} = \left(S_{A^{(-)}A^{(-)}} - S_{A^{(-)}4} + S_{4A^{(-)}} - S_{44} \right) \end{bmatrix} \tag{5.4c}$$

$$S_{cc} = \frac{1}{2} \begin{bmatrix} S_{cc11} = \left(S_{A^{(+)}A^{(+)}} + S_{A^{(+)}3} + S_{3A^{(+)}} + S_{33} \right) & S_{cc12} = \left(S_{A^{(+)}A^{(-)}} + S_{A^{(+)}4} + S_{3A^{(-)}} + S_{34} \right) \\ S_{cc21} = \left(S_{A^{(-)}A^{(+)}} + S_{A^{(-)}3} + S_{4A^{(+)}} + S_{43} \right) & S_{cc22} = \left(S_{A^{(-)}A^{(-)}} + S_{A^{(-)}4} + S_{4A^{(-)}} + S_{44} \right) \end{bmatrix} \tag{5.4d}$$

The elements value of the mixed-mode matrix ($\boldsymbol{S}_{mm}$) can be calculate by (5.4). For the requirement of impedance matching, isolation, equal power division under differential-mode excitation, and common-mode suppression, the mixed-mode matrix ($\boldsymbol{S}_{mm}$) should be satisfied the following conditions

$$\begin{cases} S_{dd11} = S_{dc11} = S_{sc31} = S_{sc41} = 0 \\ S_{ss33} = S_{ss44} = S_{ss43} = S_{ss34} = 0 \\ |S_{sd31}| = |S_{sd41}| = \dfrac{1}{\sqrt{2}} \\ |S_{cc11}| = 1 \end{cases} \tag{5.5}$$

As shown in Fig. 5-1 the circuit model of the typical balanced-to-unbalanced power divider is a symmetric structure along the center of the balanced ports (dash dot line). For simplify, the odd-/even-mode equivalent circuits can be applied to the analysis, and the individual S-parameter of the odd-/even-mode equivalent circuit can be expressed as [23]

$$S_{i,j}^{o} = S_{i,j} - S_{i,n+j} \tag{5-6a}$$

$$S_{i,j}^{e} = S_{i,j} - S_{i,n+j} \tag{5-6b}$$

where $i, j = 1, 2, n = 2$, and $S_{i,j}$, and $S_{i, n+j}$ are the elements of the standard matrix (S_{std}).

Combining (5.4) and (5.5) and according to the symmetrically of the of the proposed four-ports balanced-to-unbalanced filter power divider, these formulas can be obtained as bellow

$$\begin{cases} S_{33} = S_{34} = S_{43} = S_{44} = 0 \\ S_{12} = S_{21} = S_{42} = S_{24} = -S_{14} = -S_{41} = b \\ S_{11} = S_{13} = S_{31} = S_{33} = a \\ |a| = |b| = \dfrac{1}{2} \end{cases} \tag{5.7}$$

Therefore, the standard matrix (S_{std}) can be simplified as

$$S_{std} = \begin{bmatrix} a & b & a & -b \\ b & 0 & -b & 0 \\ a & -b & a & b \\ -b & 0 & b & 0 \end{bmatrix} \tag{5.8}$$

Furthermore, combining (5.6) and (5.8), the odd-/ even-mode S parameter scattering matrices can be derived as

$$S_{o} = \begin{bmatrix} 0 & 2b \\ 2b & 0 \end{bmatrix} \tag{5.9a}$$

$$S_{e} = \begin{bmatrix} 2a & 0 \\ 0 & 0 \end{bmatrix} \tag{5.9b}$$

5.3 Narrowband Balanced-to-Unbalanced Filtering Power Divider

5.3.1 Analysis of the Equivalent Circuits With the DM and CM Excitations

Fig. 5-2: Transmission line circuit model of the proposed BTU FPD.

Fig. 5-2 exhibits the transmission line circuit model of the proposed BTU FPD. It consists of a pair of stub-loaded dual-mode resonators (SL-DMRs), a pair of differential input ports $A^{(+)}$ and $A^{(-)}$ (ports 1 and 2), two branch lines ((Z_1, θ_1) and (Z_4, θ_1)), two pairs of coupled-line feeding structures (Z_{0e}, Z_{0o}, θ_2), a resistor (R), and two single-ended output ports (port 3 and 4). Moreover, the ideal transmission line model of the proposed BTU FPD is a symmetrical structure along the dash dot line PP', therefore, odd-/even-mode method can be used to analyze their operating principle.

Under the differential-mode (DM) excitation from $A^{(+)}$ and $A^{(-)}$ in Fig. 5-2, a virtual shorted face PP' will appear along the dash dot line. The odd-mode equivalent circuit model is shown in Fig. 5-3(a). When the electric lengths of the two shunted shorted stubs are equal to 90°, the input impedances are both equal to infinity at f_0 (The fundamental resonance frequency), therefore, the equivalent circuit in Fig. 5-3(a) can be simplified as in Fig. 5-3(b). Based on the even-/ and odd-mode analysis method, the circuit model can be further simplified as shown in Figs. 5-3(c) and (d), which input impedances of the two equivalent circuits can be calculated by
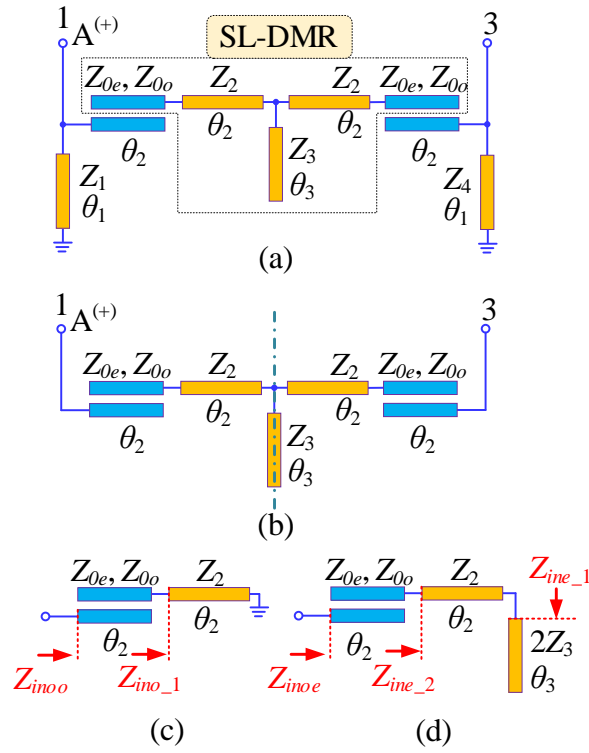
Fig. 5-3: (a) Differential-mode equivalent circuit model of the proposed BTU FPD. (b) The simplified equivalent circuit of the differential -mode of the BTU FPD. (c) The odd-mode equivalent circuit of (b). (d) The even-mode equivalent circuit of (b).

$$Z_{inoo} = Z_{11} + \frac{Z_{13}Z_{31}}{Z_{ino\_1} - Z_{33}} \tag{5.10}$$

$$Z_{ino\_1} = jZ_2 \tan\theta_2 \tag{5.11}$$

$$Z_{inoe} = Z_{11} + \frac{Z_{13}Z_{31}}{Z_{ine\_2} - Z_{33}} \tag{5.12}$$

$$Z_{ine\_2} = Z_2 \frac{Z_{ine\_1} + jZ_2 \tan\theta_2}{Z_2 + jZ_{ine\_1} \tan\theta_2} \tag{5.13}$$

$$Z_{ine\_1} = -2jZ_3 \cot\theta_3 \tag{5.14}$$

and the Z-matrix elements of the coupled-lines are [24, eq. (8.99)]

$$Z_{11} = Z_{22} = Z_{33} = Z_{44} = \frac{-j}{2}\left(Z_{0e} + Z_{0o}\right)\cot\theta_2 \tag{5.15a}$$

$$Z_{12} = Z_{21} = Z_{34} = Z_{43} = \frac{-j}{2}\left(Z_{0e} - Z_{0o}\right)\cot\theta_2 \tag{5.15b}$$

$$Z_{13} = Z_{31} = Z_{24} = Z_{42} = \frac{-j}{2} \left(Z_{0e} - Z_{0o} \right) \csc\theta_2 \qquad (5.15c)$$

$$Z_{14} = Z_{41} = Z_{23} = Z_{32} = \frac{-j}{2} \left(Z_{0e} + Z_{0o} \right) \csc\theta_2 \qquad (5.15d)$$

When $\theta_2 = 45°$, and $\theta_3 = 90°$, the input impedances of the odd-mode and even-mode can be simplified and calculated by combine equations (5.10) - (5.15). Thus

$$Z_{inoo} = Z_{inoe} = -j\frac{2PZ_2 - P^2 + 8M}{4Z_2 + 2P} \qquad (5.16)$$

and

$$P = Z_{0e} + Z_{0o} \qquad (5.17a)$$

$$M = Z_{0e}Z_{0o} \qquad (5.17b)$$

The reflect coefficient of the odd-mode equivalent of the circuit S_{o11} shown in Fig. 5-3(b) can be calculated using the reflection coefficients of the odd-mode and even-mode as below

$$S_{o11} = \frac{\Gamma_e + \Gamma_o}{2} \qquad (5.18)$$

where

$$\Gamma_e = \frac{Z_{inoe} - Z_0}{Z_{inoe} + Z_0}, \ \Gamma_o = \frac{Z_{inoo} - Z_0}{Z_{inoo} + Z_0}$$

By solving $S_{o11} = 0$ with (5.9a), the following equation can be easily derived as follows

$$Z_{inoo}Z_{inee} = Z_0^2 \qquad (5.19)$$

Combining (5.16) and (5.19), the relationship of (5.20) can be obtained

$$\left(16Z_0^2 + 4P^2\right)Z_2^2 + \left(16PZ_0^2 - 4P^3 + 32MP\right)Z_2$$
$$+ \left(4P^2Z_0^2 + P^4 - 16MP^2 + 64M^2\right) = 0 \qquad (5.20)$$

For common-mode (CM) excitation, a virtual open-circuited face will appear in the symmetrical face along the dash-dot line in Fig. 5-2. The even-mode equivalent circuit model of the BTU FPD is shown in Fig. 5-4(a). When the electrical length θ_1 of left shunted branch line is 90°, the input impedance Z_{in1} is equal to zero at f_0 (i. e., short circuited), thus the port 1 is short-circuited, the even-mode equivalent circuit in Fig. 5-4(a) can be simplified into the circuit shown in Fig. 5-4(b). Moreover, the loaded position

of the open-stub equivalent to a short-circuited when the electrical length of the open-stub θ_3 equal to 90° at f_0. Hence, the circuit model in Fig. 5-4(b) can be simplified as in Fig. 5-4(c). From the circuit model in Fig. 5-4(c), the input impedance Z_{ine} can be expressed as

$$Z_{ine} = \frac{1}{Z_{inL}} + \frac{1}{Z_{inR}} \tag{5.21}$$

$$Z_{inR} = \frac{2RZ_4 + jZ_4^2 \tan\theta_4}{Z_4 + j2R\tan\theta_4} \xrightarrow{\theta_4 = \pi/2} Z_{inR} = \frac{Z_4^2}{2R} \tag{5.22}$$

$$Z_{inL} = Z_{44} + \frac{Z_{42}Z_{24}}{Z_{inL\_1} - Z_{22}} \tag{5.23}$$

$$Z_{inL\_1} = jZ_2 \tan\theta_2 \tag{5.24}$$

With calculating the input impedance Z_{ine} of the circuit mode in Fig. 5-4(c), S_{11} of the even-mode can be calculated by the following equation

$$\left|S_{e11}\right| = \left|\frac{Z_{ine} - Z_0}{Z_{ine} - Z_0}\right| \tag{5.25}$$

From (5-9b), with $S_{e11} = 1$, the following relationship can be obtained by combining (5.21)−(5.25)

$$\begin{aligned} 2RP^2 - 4RZ_2P - 16RM - j\left(4Z_2 + 2P\right)Z_4^2 \\ = \left(2Z_2P - P^2 + 8M\right)Z_0Z_4^2 \end{aligned} \tag{5.26}$$

In order to obtain good power division, filtering, isolation and common-mode suppression performances, the designed BTU FPD should be satisfied the conditions of (5.20) and (5.26), simultaneously. The odd-mode impedance Z_{0o} and even-mode impedance Z_{0e} of the parallel coupled-line can be obtained according to the specification of bandwidth, which will introduce in the next section. Once the Z_{0o} and Z_{0e} are determined, we can calculate the value of the characteristic impedance Z_2 by equation (5.20). And then, the relationship between the characteristic impedance Z_4 of the branch-line and isolation resistor R can be established. Finally, the optimized values of Z_4 and R can be decided by parameter sweep analyzing.
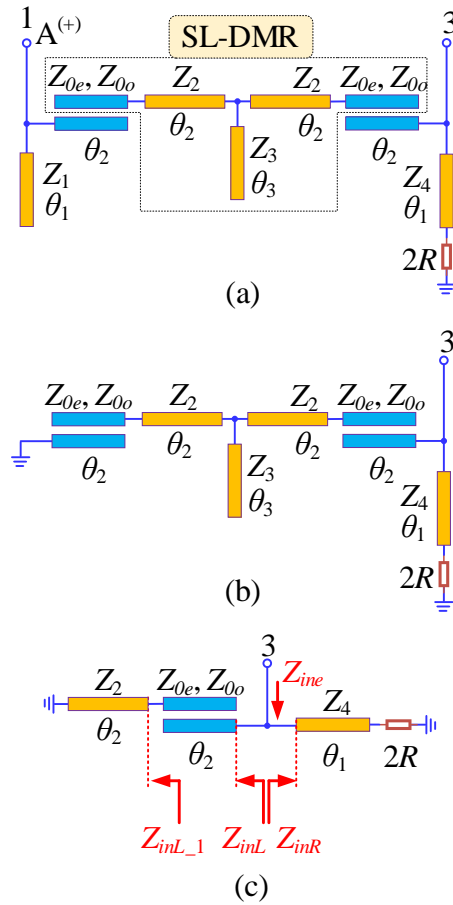
Fig. 5-4: (a) Common-mode equivalent circuit model of the proposed BTU FPD. (b) The simplified equivalent circuit of the common-mode of the BTU FPD. (c) The final simplified equivalent circuit of the even-mode of the BTU FPD.

5.3.2 Parameters Study

For studying the key design parameters, we assume that the initial values of the ideal transmission line model in Fig. 5-2 are $Z_1 = Z_4 = 24.9\ \Omega$, $Z_2 = 156\ \Omega$, $Z_3 = 72\ \Omega$, $Z_{0e} = 196\ \Omega$, $Z_{0o} = 115\ \Omega$, $R = 200\ \Omega$, $\theta_1 = \theta_3 = 90°$, and $\theta_2 = 45°$, respectively. The simulated results of the BTU FPD for Fig. 5-2 with parameters analysis by Advanced Design System software are shown in Figs. 5-5(a)–(f). In Figs. 5-5(a) and (d), it can be found that with Z_1 or (and) Z_4 decreasing, the CM responses become better, while the in-band return loss of DM responses is worse away from the matching point, and there are both little effect on the isolation performances. Fig. 5-5(b) exhibits the responses with different Z_2 (152,
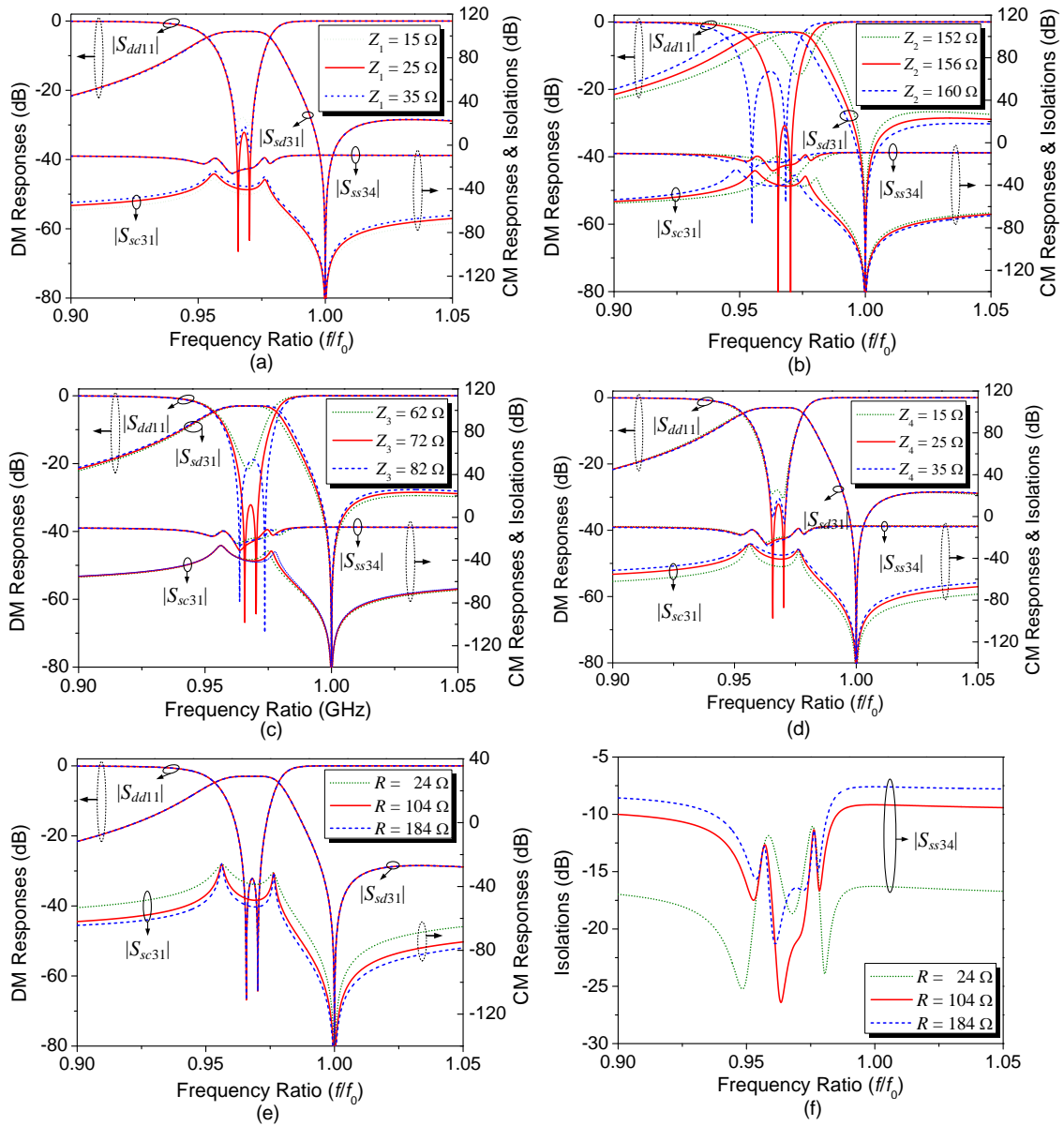
Fig. 5-5: Simulated responses of the proposed BTU FPD with parameters study. (a) DM responses, CM responses, and isolation performances versus Z_1; (b) DM responses, CM responses, and isolation performances versus Z_2; (c) DM responses, CM responses, and isolation performances versus Z_3; (d) DM responses, CM responses, and isolation performances versus Z_4; (e) DM responses, and CM responses versus R; and (f) Isolation performances versus R.

156, and 160 Ω). It is seen that the bandwidth and resonance frequency can be controlled by Z_2. With Z_2 increasing, the bandwidth becomes wider and the resonance frequencies of the DM and CM excitation are shift to lower, while the isolation performance has little

influence. From Fig. 5-5(c), Z_3 can be used to slightly adjust the bandwidth of the DM condition. Moreover, the CM suppression and isolation performance can be controlled by adjusting the isolation resistor R without having effect on DM response, as shown in Figs. 5-5(e) and (f), respectively. By increasing R, the CM suppression performance becomes better, but the isolation performance becomes worse, illustrated in Figs. 5-5(e) and (f). Therefore, the CM suppression and isolation performances should be both take in account at the same time when the value of R decided.

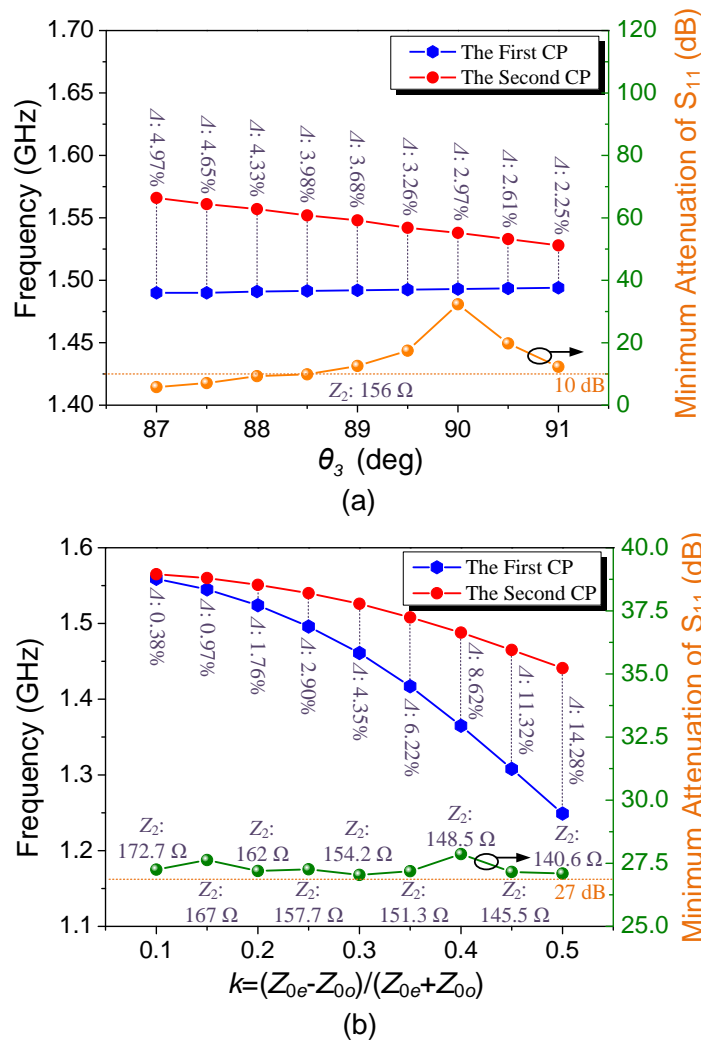## 5.3.3 Analysis of the Controllability of Bandwidth

(a)

(b)

Fig. 5-6: Differential responses of the proposed BTUB-FPD with different values of (a) θ_3 and (b) coupling coefficient k.

According to the methods of bandwidth broaden, the variation of bandwidth is divided into two situations. For the first situation, the bandwidth can be varied by separating the odd-mode and even-mode resonant frequencies (f_{odd} and f_{even}), as shown in Fig. 5-6(a). With θ_3 decreasing, the frequency of the second crossing point (CP, f_{CP2}) between reflect curve ($|S_{dd11}|$) and transfer curve ($|S_{sd31}|$) of the proposed BTU FPD, which is positively correlated with the even-mode resonant frequency, shifts to higher frequency range. At the same, the frequency of the first crossing point (CP, f_{CP1}), which is positively correlated with the odd-mode resonant frequency, is fixed. Thus, the fractional bandwidth ($\Delta = (f_{CP2} - f_{CP1}) / 0.5(f_{CP2} + f_{CP1})$) becomes wider when θ_3 decreases. However, the minimum in-band attenuation of S_{11} will becomes worse when θ_3 changes while other electric parameters are fixed. Therefore, in order to ensure a good in-band attenuation, this situation is only suitable for bandwidth adjustment in a small range.

In the second situation, the electrical lengths (θ_2 and θ_3) of the determined odd-mode resonant frequency f_{odd} and even-mode resonant frequency f_{even} are fixed to check bandwidth variation with the coupling coefficient k. The coupling coefficient k is equivalent as external coupling in filter design, which is effect on the bandwidth of the designed filter directly. In this design, the coupling coefficient k can be calculated as

$$k = \frac{Z_{0e} - Z_{0o}}{Z_{0e} + Z_{0o}} \tag{5.27}$$

In order to determine the influence of the parameter k on the bandwidth controllability, a circuit model with $Z_1 = Z_4 = 24.9\ \Omega$, $Z_3 = 72\ \Omega$, $R = 100\ \Omega$, $\theta_1 = \theta_3 = 90°$, and $\theta_2 = 45°$ is used to analyze the bandwidth controllability varies with k. As shown in Fig. 5-6 (b), the fractional bandwidth changed from 0.38% to 14.28% with the coupling coefficient k increasing from 0.1 to 0.5. Theoretically, the stronger the coupling coefficient, the wider the bandwidth, but it is difficult to fabricate in practice when k larger than 0.5. Moreover, it is worth mentioning that the characteristic impedance Z_2 is also adjusted to remain a good impedance matching with k changing. Fig. 5-6(b) illustrates that the minimum in-band attenuations of S_{11} are better than 27dB. Therefore, the bandwidth of the BTU FPD can be controlled by the even-mode impedance Z_{0e} and odd-mode impedance Z_{0o} of the coupled-line sections in this situation. Table 5.1 gives the

corresponding values of bandwidth ($BW = f_{CP2} - f_{CP1}$), isolation of DM condition (Iso.$|_{DM}$), and common-mode suppression ($Supp.|_{CM}$) of the proposed BTU FPD. It shows that the isolations and CM suppressions are both lower than 25 dB. Therefore, the proposed BTU FPD has a good bandwidth variable ability, which can meet different bandwidth requirements with high isolation and CM suppression performances.

TABLE 5.1. Four group values of the bandwidth, center frequency, in-band attenuation, and common-mode suppression of the proposed BTUB-FPD

Characteristic impedances (Ω)			k	BW (MHz)	Iso.$|_{DM}$ (dB)	$Supp.|_{CM}$ (dB)
Z_{0e}	Z_{0o}	Z_2				
190	155.46	172.7	0.10	6	25.36	54.34
192	141.93	167.0	0.15	15	25.71	47.09
194	129.33	162.0	0.20	27	25.59	42.21
196	117.60	157.7	0.25	44	25.64	35.8
198	106.62	154.2	0.30	65	25.75	34.91
200	96.30	151.3	0.35	91	25.89	31.88
202	86.57	148.5	0.40	123	26.56	29.69
204	77.38	145.5	0.45	157	27.62	27.43
206	68.67	140.6	0.50	192	28.82	25.23

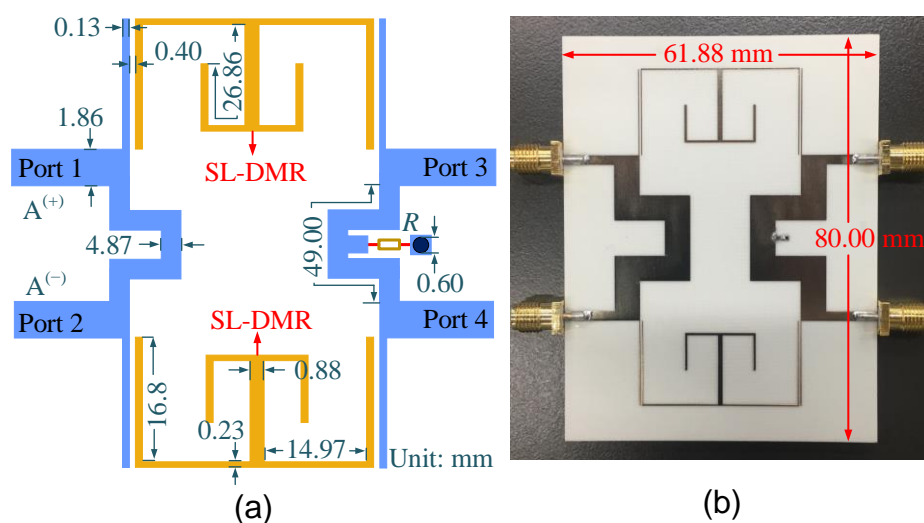## 5.3.4 Implement of the Narrowband BTU FPD

Fig. 5-7: Structure I: (a) Configuration of the BTU FPD without the coupled branch line (CBL); (b) Photograph of the BTU FPD without the coupled branch line (CBL).

To demonstrate the aforementioned design theory, a BTU FPD prototype with center frequency of f_0 = 1.57 GHz, fractional bandwidth of 2.6% is designed with good filtering and high CM suppression responses. Firstly, based on the odd-mode theory analysis, the electric lengths $\theta_1 = \theta_3 = 90°$, and $\theta_2 = 45°$ at f_0 = 1.57 GHz are readily selected. Then, according to the above analysis about the bandwidth controllability in Fig. 5-6 and the limitation of the printed circuit broad (PCB) fabrication technology [24, Fig. 7.29], the even-mode impedance Z_{0e} and odd-mode impedance Z_{0o} of the coupled-line section can be determined. Once the even-mode and odd-mode impedances of the coupled-line section Z_{0e} and Z_{0o} are determined, the characteristic impedance Z_2 can be calculated by (5.20). Finally, we can derive the relationship between the branch line characteristic impedance Z_4 and the isolation resistor R using (5.26). In order to obtain a high isolation and CM suppression performances at the same time, the values of Z_4 and R can be determined under the compromise choice. The final configuration of the proposed BTU FPD is constructed as shown in Fig. 5-7(a). The circuit is fabricated on a Rogers RO4003C substrate with a dielectric constant of 3.38, a thickness of 0.813 mm, and a loss tangent of 0.0027, which physical sizes are illustrated in Fig. 5-7(a). The photograph of the proposed BTU FPD with overall circuit size of 61.88 mm × 80 mm is shown in Fig. 5-7(b).

5.3.5 Experimental Results and Discussion

The fabricated BTU FPD is measured using a four-port network analyzer *CETC-41 Ceyear* 3672E. The theoretical, simulated and the measured results are compared as shown in Fig. 5-8 and Fig. 5-9. In Fig. 5-8, the proposed BTU FPD operate at 1.528 GHz, with fractional bandwidth is 2.02% for the DM. The minimum input-power-matching $|S_{dd11}|$ is lower than 20 dB within the frequency range 1.52 GHz to 1.54 GHz, and the measured minimum in-band power insertion loss $|S_{sd31}|$ is 1.14 dB (ignore the 3-dB power division factor). In addition, the power isolation $|S_{ss34}|$ between the two single-ended output ports is better than −15 dB at the center frequency of the proposed BTU FPD, and also better than −8 dB from DC to 6 GHz, as shown in Fig. 5-8(b). Fig. 5-8(b) shows that the upper stopband performance of proposed BTU FPD without CBL is only 1.83f_c with lower than −10 dB (where f_c is the center frequency of the proposed BTU FPD). From

Fig. 5-9, the measured CM suppression is better than 23 dB from DC to 2.5 GHz. Moreover, a transmission zero is generated at the upper stopband of 1.57 GHz by the open-circuited stub (Z_3, θ_3), which exists in both DM and CM responses in Fig. 5-8(b) and Fig. 5-9.
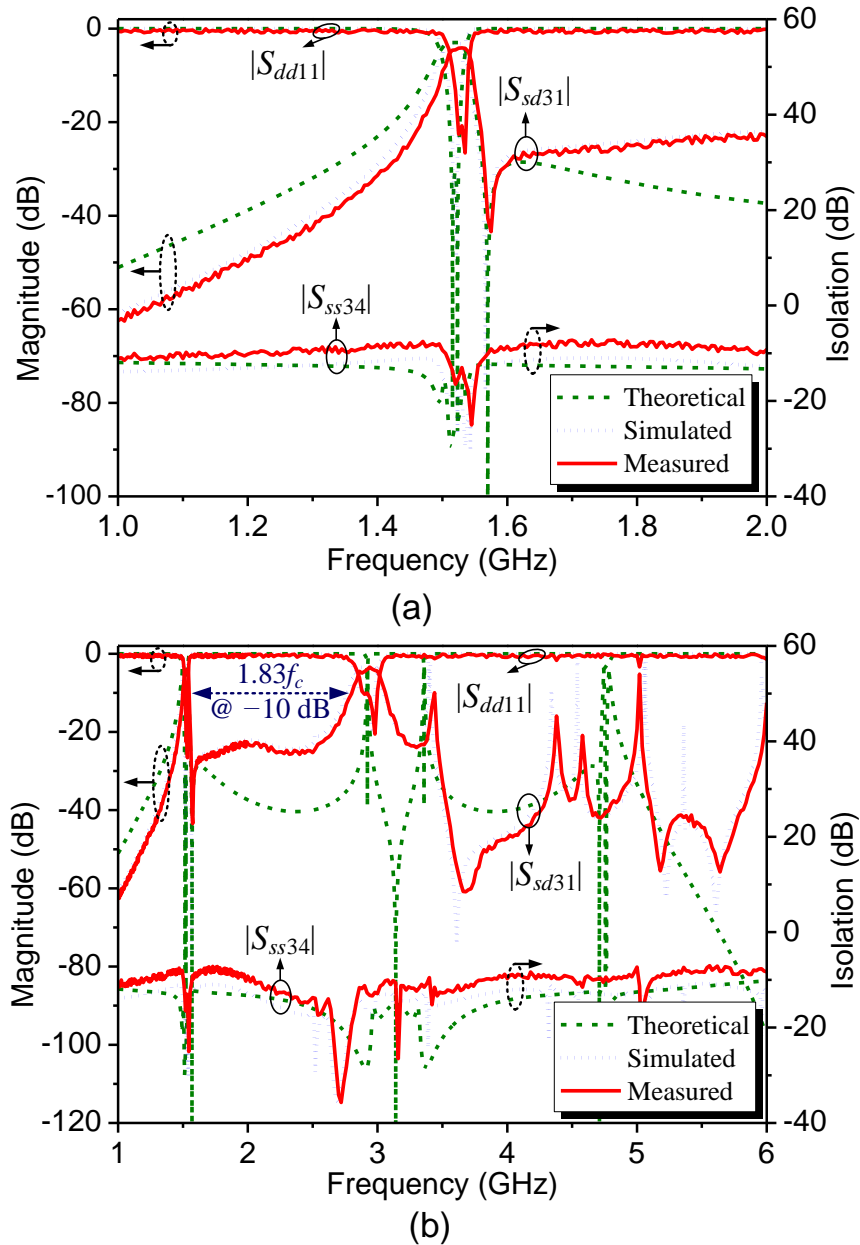

(a)

(b)

Fig. 5-8: The theory, simulation and measurement of DM responses the BTUB-FPD without coupled branch line (CBL) (Structure I).
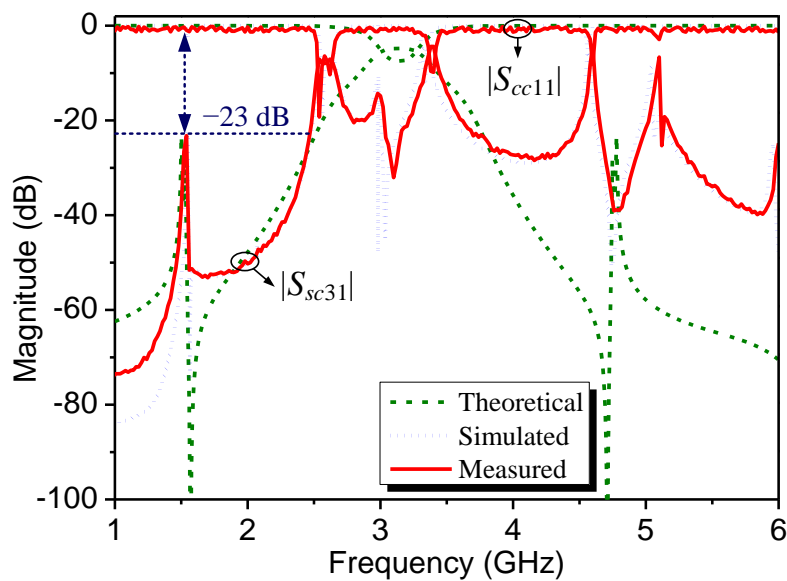
Fig. 5-9: The theory, simulation and measurement CM responses of the BTUB-FPD without coupled branch line (CBL) (Structure I).

5.4 High-Selectivity Narrowband Balanced-to-Unbalanced Filtering Power Divider

It shows that the proposed BTU FPD (Structure I) has only one transmission zero (f_{Z1}) in Fig. 5-8, in above section. In order to enhance the selectivity of passband, a coupled line is used to replace the microstrip branch line (Z_1, θ_1), as shown in Fig. 5-10. The coupled branch line (CBL) structure can generate a pair of additional transmission zeros (f_{Z2} and f_{Z3}) locate at both sides of the passband.

5.4.1 Analysis of the Multiple Transmission Zeros

From Fig. 5-11, the circuit model simulated DM response of structure II shows that there are six transmission zeros located at the both side of the DM passband. Comparing with the structure I, the additional DM transmission zeros (f_{Z2}, f_{Z3}, f_{Z5} and f_{Z6}) are generated by the CBL. Under the DM excitation, the equivalent circuit of CBL is a short-circuited coupled-line structure shown in Fig. 5-10. The frequencies of the additional DM transmission zeros (f_{Z2}, f_{Z3}, f_{Z5} and f_{Z6}) can be calculated by setting the input impedance Z_{in_CBL} of the short-circuited CBL equal to zero. The input impedance Z_{in_CBL} can be

derived as

$$Z_{in\_CBL} = \frac{Z_{22}Z_{44} - Z_{24}Z_{42}}{Z_{44}}$$

$$= j\frac{(Z_{0e1} + Z_{0o1})^2 \sin^2\theta_{CBL} - 4Z_{0e1}Z_{0o1}}{2(Z_{0e1} + Z_{0o1})\sin\theta_{CBL}\cos\theta_{CBL}}$$
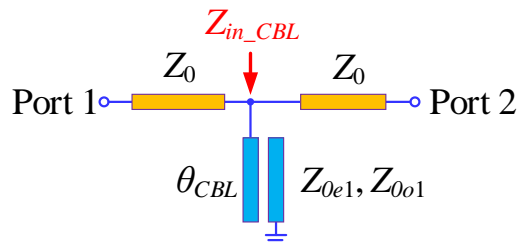
(5.28)

Fig. 5-10: Short-circuited coupled branch line (CBL).
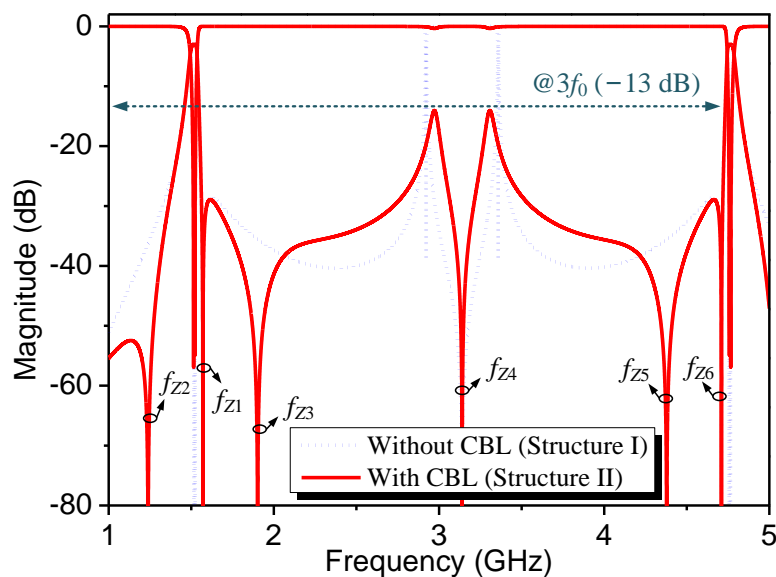

Fig. 5-11: The theoretical DM responses of the proposed structure I and II.

The frequencies of the transmission zeros can be derived when the input impedance $Z_{in\_CBL} = 0$.

$$f_{Z1} = f_0 \quad (\theta_3 = 90° \ @f_0)$$

(5.29a)

$$f_{Z2} = \frac{2f_0}{\pi}\arcsin\sqrt{\frac{4Z_{0e1}Z_{0o1}}{(Z_{0e1} + Z_{0o1})^2}}$$

(5.29b)

$$f_{Z3} = 2f_0 - f_{Z2} \tag{5.29c}$$

$$f_{Z4} = 2f_0 \tag{5.29d}$$

$$f_{Z5} = 4f_0 - f_{Z3} \tag{5.29e}$$

$$f_{Z6} = 3f_0 \tag{5.29f}$$

In Fig. 5-11, it is can be seen that the structure II not only has a better selectivity, but also a wider upper stopband performance. Moreover, the structure II have six transmission zeros are located at 1.24, 1.57, 1.90, 3.14, 4.38, and 4.71 GHz, respectively.

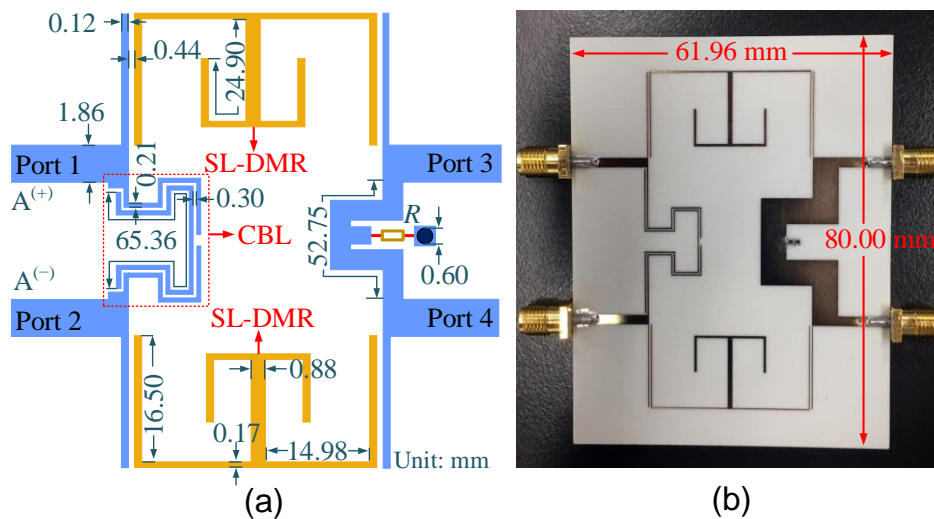## 5.4.2 Experimental Results and Discussion

Fig. 5-12: Structure II: (a) Configuration of the BTU FPD with the coupled branch line (CBL); (b) Photograph of the BTU FPD with the coupled branch line (CBL).

With the similar design procedure, the BTU FPD with CBL (Structure II) is fabricated and measured with final physical sizes illustration in Fig. 5-12(a). The photograph of the proposed BTU FPD with CBL is shown in Fig. 5-12(b), and the overall circuit size is 61.96 mm × 80 mm. Fig. 5-13 shows the results of the proposed BTU FPD with CBL. It can be seen from Fig. 5-13(a) that the measured center frequency of 1.528 GHz, fractional bandwidth $\Delta = 2.43\%$ and the minimum input-power-matching $|S_{dd11}|$ is lower than 20 dB within the frequency range 1.52 GHz to 1.54 GHz. Moreover, the measured minimum in-band power insertion loss $|S_{sd31}|$ is 1.01 dB (ignore the 3-dB power

division factor). The power isolation $|S_{ss34}|$ between the two single-ended output ports is better than −20 dB at the center frequency 1.528 GHz, and also better than −10 dB from DC to 6 GHz, as shown in Fig. 5-13(b). Moreover, the proposed BTU FPD with CBL has good performance of upper stopband from DC to 6 GHz (about 3.9f_c, where f_c is the center frequency of the proposed BTU FPD) better than -10dB, as shown in Fig. 5-13(b). Under the CM excitation, the measured CM suppression is better than 32 dB in DM passband from 1.52 GHz to 1.54 GHz, as illustrated in Fig. 5-14.
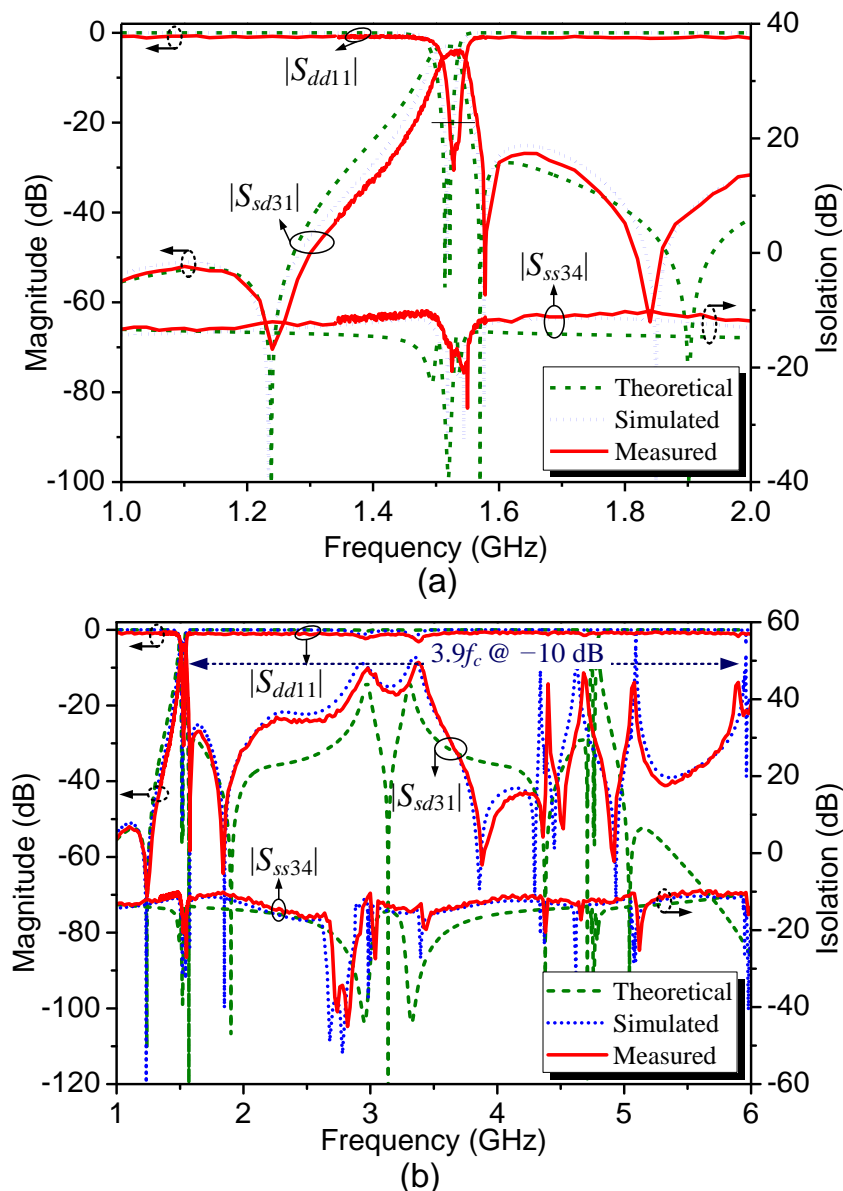

Fig. 5-13: The theory, simulation and measurement DM responses of the BTUB-FPD with coupled branch line (CBL) (Structure II).
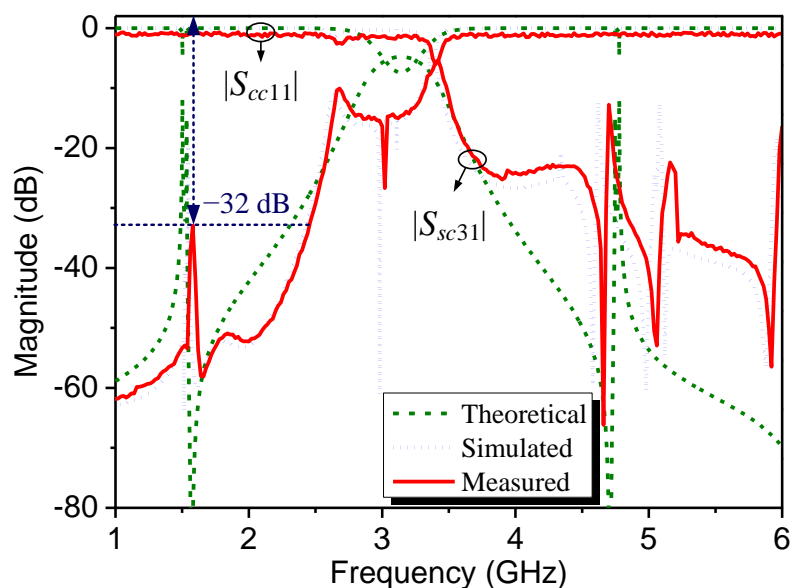
Fig. 5-14: The theory, simulation and measurement CM responses of the BTUB-FPD with coupled branch line (CBL) (Structure II).

5.5 Conclusion

In this chapter, two narrowband BTU FPDs with composite functions of power division, frequency selectivity, isolation between single output ports, and common-mode suppression have been proposed by stub-loaded dual-mode resonators and parallel coupled-line feeding structure. Mixed-mode S-parameters matrix and odd-/even-mode input impedances are derived to reveal the operation principle. The bandwidth of the proposed BTU FPDs can be varied and controlled. The measured results of the two prototypes are agree well with the simulation results with good DM transmission under CM noise suppression and high isolation between two single ended output ports. Moreover, multiple transmission zeros were produced to enhance frequency selectivity and stopband performance in the Structure II. Therefore, the proposed BTU FPDs are good candidate for balanced-to-unbalanced wireless system with satisfying different bandwidth requirements.

References

[1] J. Wang, F. Huang, L. Zhu, C. Cai, and W. Wu, "Study of a new planar-type balun topology for application in the design of balun bandpass filters," *IEEE Trans. Microw. Theory Techn.*, vol. 64, no. 9, pp. 2824–2832, Sep. 2016.

[2] J. –X. Chen, Y. Zhan, W. Qin, and Z.-H. Bao, "Design of high-performance filtering balun based on TE01-mode dielectric resonator," *IEEE Trans. Ind. Electron.*, vol. 64, no. 1, pp. 451–458, Jan. 2017.

[3] L. –P. Feng, and L. Zhu, "Compact wideband filtering balun using stacked composite resonators," *IEEE Access*, vol. 6, pp. 34651–34658, Jul. 2018.

[4] C. –H. Wu, C. –H. Wang, and C. H. Chen, "A novel balanced-to-unbalanced diplexer based on four-port balanced-to-balanced bandpass filter," *Proceedings of the 38th European Microwave Conference*, pp. 28–31, 2008.

[5] Q. Xue, J. Shi, and J. –X. Chen, "Unbalanced-to-balanced and balanced-to-unbalanced diplexer with high selectivity and common-mode suppression," *IEEE Trans. Microw. Theory Techn.*, vol. 59, no. 11, pp. 2848–2855, Nov. 2011.

[6] C. –M. Chen, S. –J. Chang, C. –F. Yang, and C. –Y. Chen, "A simple and effective method for designing frequency adjustable balun diplexer with high common-mode suppression," *IEEE Microw. Wireless Compon. Lett.*, vol. 25, no. 7, pp. 433–435, Jul. 2015.

[7] L. S. Wu, Y. X. Guo, L. F. Qiu, and J. F. Mao, "A new balanced-to-single-ended (BTSE) power divider," in *Proc. IEEE Int. Wireless Symp.*, 2014, pp. 1–4.

[8] W. Zhang, Y. Wu, Y. Liu, F. M. Ghannouchi, and A. Hasan, "A wideband balanced-to-unbalanced coupled-line power divider," *IEEE Microw. Wireless Compon. Lett.*, vol. 26, no. 6, pp. 410–412, Jun. 2016.

[9] A. N. Yadav, and R. Bhattacharjee, "Balanced to unbalanced power divider with arbitrary power ratio," *IEEE Microw. Wireless Compon. Lett.*, vol. 26, no. 11, pp. 885–887, Nov. 2016.

[10] Y. Wu, Z. Zhuang, L. Jiao and Y. Liu, "A novel balanced-to-unbalanced complex impedance-transforming in-phase power divider," *IEEE Access*, vol. 5, pp. 16205–16213, Sep. 2017.

[11] J. Shi, J. Lu, K. Xu, and J. –X. Chen, "A coupled-line balanced-to-single-ended out-of-phase power divider with enhanced bandwidth," *IEEE Trans. Microw. Theory Techn.*, vol. 65, no. 2, pp. 459–466, Feb. 2017.

[12] W. Zhang, X. Shen, Y. Wu, Y. Liu, A. Hasan, F. M. Ghannouchi, and Y. Zhao, "Planar miniaturized balanced-to-single-ended power divider based on composite left- and right-handed transmission lines," *IEEE Microw. Wireless Compon. Lett.*, vol. 27, no. 3, pp. 242–244, Mar. 2017.

[13] X. Ren, and K. D. Xu, "Multilayer balanced-to-unbalanced power divider with wideband transmission characteristic and common-mode suppression," *IEEE Trans. Compon., Pakag., Manuf. Technol.,* vol. 9, no. 1, pp. 72–79, Jan. 2019.

[14] W. Feng, M. Hong, M. Xun, and W. Che, "A novel wideband balanced-to-unbalanced power divider using symmetrical transmission lines," *IEEE Microw. Wireless Compon. Lett.*, vol. 27, no. 4, pp. 338–340, Apr. 2017.

[15] K. Xu, J. Shi, L. and Lin, J. –X. Chen, "A balanced-to-unbalanced microstrip power divider with filtering function," *IEEE Trans. Microw. Theory Techn.*, vol. 63, no. 8, pp. 2561–2569, Aug. 2015.

[16] X. Gao, W. Feng, W. Che, and Q. Xue, "Wideband balanced-to-unbalanced filtering power dividers based on coupled lines," *IEEE Trans. Microw. Theory Techn.*, vol. 65, no. 1, pp. 86–95, Jan. 2017.

[17] Z. Zhuang, Y. Wu, L. Jiao, W. Wang, and Y. Liu, "Wideband balanced-to-unbalanced filtering unequal power divider with wide stopband and isolation," *Electron. Lett.*, vol. 53, no. 13, pp. 892–894, Jun. 2017.

[18] M. Luo, X. –H. Tang, D. Lu, Y. –H. Zhang, and X. –M. Yu, "Balanced-to-unbalanced filtering power divider with compact size and high common-mode suppression," *Electron. Lett.*, vol. 54, no. 8, pp. 509–511, Apr. 2018.

[19] L. Li, W. Cheng, L. –S. Wu, J. –F. Mao, M. Tang and X. –W. Gu, "A wideband filtering balanced-to-unbalanced out-of-phase power divider," *IEEE Microw. Wireless Compon. Lett.*, vol. 28, no. 10, pp. 870–873, Oct. 2018.

[20] L. Jiao, Y. Wu, Z. Zhuang, Y. Liu, and A. A. Kishk, "Planar balanced-to-unbalanced In-phase power divider with wideband filtering response and ultra-wideband common-mode rejection," *IEEE Trans. Circuits Syst. I, Reg. Papers,* vol. 65, no. 6, pp. 1875–1886, Jun. 2018.

[21] F. Huang, J. Wang, J. Hong, and W. Wu, "A new balanced-to-unbalanced filtering power divider with dual controllable passbands and enhanced in-band common-mode suppression," *IEEE Trans. Microw. Theory Techn.*, vol. 67, no. 2, pp. 695–703, Feb. 2019.

[22] W. R. Eisenstadt, B. Stengel, and B. M. Thompson, *Microwave Differential Circuit Design Using Mixed-Mode S-Parameters*. Boston, MA, USA: Artech House, 2006

[23] M. Roberg and C. Campbell, "A novel even & odd-mode symmetric circuit decomposition method," in *Proc. IEEE Compound Semicond. Integer. Circuit Symp.*, pp. 1–4, Oct. 2013.

[24] D. M. Pozar, *Microwave Engineering*, 4th Ed. New York, NY, USA: Wiley, 2011.

Chapter 6

Conclusion and Future Work

6.1 Conclusions

In the development of multi-band and multi-function RF/microwave devices, there are still many challenging issues. As described in Chapter 1, the circuit size, insertion loss, and the controllability of the frequencies and bandwidths are difficult to overcome in multi-band BPF design. Moreover, high integration and multi-function microwave device is the development tendency of the future RF/microwave communication systems.

The basic design theory of the bandpass filters, power dividers, and differential circuits have been introduced in Chapter 2. Those topics are summarized from open literatures to guide the design of subsequent chapters. The general definitions of filters and the lowpass prototype filters have been introduced to guide the multiband BPFs. And then, the microwave network analysis method has been exhibited. With the impedance, scattering, and ABCD matrices of the microwave network, most of the microwave devices can be represented as two-port or n-port network to analysis. Lastly, the differential circuit mixed-mode S-parameters have been introduced to design and analysis the balanced-to-unbalanced filter power divider circuits.

In Chapter 3, two types of MMRs are proposed and used to design a number of multiband BPFs. One is the stub-loaded stepped impedance resonator (SL-SIR), which has flexible resonant modes and controllable resonance frequencies. The other one is a dual-resonance resonator (also called H-shaped resonator), which have two resonance modes and two potential transmission zeros. With the two multi-mode resonators, the following designs are implemented:

■ An open-circuited stub-loaded quarter-wavelength steeped impedance resonator is adopted to design a compact bandpass filter with high selectivity performance. Moreover, mixed electric and magnetic coupling is introduced between two SLSIRs to produce multiple transmission zeros located at the two side of each passband, resulting in high passband selectivity and large isolation in-between the two passbands.

■ Dual-feed line structure is proposed and adopted to design dual-band BPF to realize independent controllable bandwidths of the two passbands

. A compact dual-band BPF is developed by using a new stub-loaded shorted SIR. The obtained results and related discussions reveal that with appropriate design of the geometrical parameters of the proposed structure, a dual-band BPF with individually controllable mid-band frequencies, passband bandwidths, and transmission zeros, can be designed with great flexibility.

■ A compact second-order DB-BPF with individually controllable passbands and wide stopband is proposed and fabricated using two OSL-SSIRs. The resonance mechanism and frequency variation of the resonator were analyzed in detail. By taking advantages of the OSL-SSIR and multiple mixed electric and magnetic coupling paths, flexible control of the center frequencies and bandwidths of the DB-BPF is achieved, and high selectivity of the passbands and wide stopband are realized.

■ Separate geometrical parameters are devised to implement independent control of the centre frequencies and FBWs of the three passbands. Two source-loaded couplings are employed to produce a significantly increased number of TZs and achieve thereby high selectivity and stopband suppression of filter.

■ A miniaturized dual-band bandpass filter using composite resonators with flexible frequency ratio is developed. Three transmission zeros are produced by introduced a mixed electric and magnetic coupling, which improves significantly the selectivity and out-band rejection performance. With the features of compactness, flexible design, and high performance, the proposed dual-band filter is attractive for dual-band wireless communication applications, such as the GPS and the TD-LTE system.

A novel dual-band filtering power divider with ultrawide stopband and good isolation is proposed in Chapter 4. The measured responses exhibits a stopband up to 13.8 GHz ($6f_0$) with 20-dB rejection level. This is the widest stopband of DB-FPDs reported thus far, with the following contributions:

■ The modified dual-resonance resonator (DRR) with stepped-impedance are adopted to realize the dual-band frequencies selectivity. Moreover, the proposed modified DRR have compact circuit size.

■ A pair of unequal length spurlines have been inserted into the U-shaped feedline

to suppression the harmonic frequencies, which are produced by the U-shaped feedline structure. Moreover, the spurious frequencies of the DRR are adjusted to the stopband of the Wilkinson power divider to further enhance the stopband performance.

■ The coexistence of the mixed electric and magnetic couplings has been used to build up a pair of opposite coupling paths, which can produce a transmission zero, which is enhanced the isolation between the two passbands.

In Chapter 5, the stub-loaded dual-mode resonator (SL-DMR) with controllable resonant frequency and an intrinsic transmission zero is adopted to design BTU FPDs for the first time. The designs of this chapter not only achieved controllable operating frequency and high selectivity, but also have a big variable range of the bandwidth from narrowband to wideband, which can be summarized as below:

■ The mixed-mode scattering matrix is analyzed, and the final conditions of better DM matching, high isolation, and deeper CM suppression are obtained.

■ Based on even-mode and odd-mode analysis method, the closed-form analytical equations, detail design procedure and key parameters study is synthetically analyzed.

■ Two cases of the bandwidth controllable BTU FPDs are proposed and analyzed. The first case is adjusting the even-mode frequency to realize the bandwidth control at the minimum range. In the second case, the bandwidth can be varied in a relatively large range by controlling the coupling coefficient of the parallel-coupled lines.

■ To realize high selectivity of the proposed balanced-to-unbalanced filter power divider, a coupling branch line is used to replace the traditional one to generate extra two transmission zeros.

6.2 Future Work

As indicted in Fig. 1-2, the transceiver systems include phase shifter, power divider, circulator, bandpass filter and other active devices, which are complicated and large size. Although numbers of multi-band bandpass filters, dual-band filtering power dividers, and balanced-to-unbalanced filtering power divider have been proposed and designed, novel components with compact size, lower cost, higher integration, and more functions are still strongly demanded for future wireless communication systems.

The short-term future work for the multi-band, multi-function, and compact

microwave components can be carried out in the following areas:

■ The bandwidth of the two passbands of the proposed filtering power divider is still not controllable. It is probable to design multiple signal paths to improve the controllability of the bandwidths as we have done in Chapter 3 when designing the multi-band BPFs.

■ Based on the multi-mode concept, we can design compact multi-band balanced-to-unbalanced filtering power dividers to replace conventional systems with separate baluns, bandpass filters, and power dividers to save the circuit size and cost.

■ As shown in Chapter 5, the insertion loss of the multi-function component is still large, because the structure of circuit is too complex. Therefore, we can use the extremely low-loss material, such as high temperature superconductors, to design the multifunction components.

■ Research an active filtering antenna array as a single component to realize the function of RF-front of the current receiver or transmitter. If it is accomplished, the RF-front system will become smaller, cheaper, and more flexible.

Author's Publications

Journal Papers:

[1] **Pin Wen**, Zhewang Ma, Haiwen Liu, Shuangshuang Zhu, Baoping Ren, Xiaolong Wang, and Masataka Ohira, "A miniaturized dual-band bandpass filter using composite resonators with flexible frequency ratio," *IEICE Electronics Express*, vol. 15, no. 5, pp. 1-6, Feb. 2018.

[2] **Pin Wen**, Zhewang Ma, Haiwen Liu, Shuangshuang Zhu, Yi Song, Baoping Ren, Xiaolong Wang, and Masataka Ohira, "Dual-band filtering power divider using dual-resonance resonators (DRRs) with ultrawide stopband and good isolation," *IEEE Microwave and Wireless Components Letters*, vol. 29, no. 2, pp. 101-103, Feb. 2019.

[3] **Pin Wen**, Zhewang Ma, Haiwen Liu, Shuangshuang Zhu, Baoping Ren, Xuehui Guan, and Masataka Ohira, "Individually controllable dual-band bandpass filter with wide stopband and multiple transmission zeros," *IEICE Electronics Express*, vol. 6, no. 7, pp. 1-5, Mar. 2019.

[4] **Pin Wen**, Zhewang Ma, Haiwen Liu, Shuangshuang Zhu, Baoping Ren, Xuehui Guan, and Masataka Ohira, "Design of compact tri-band bandpass filter using stub-loaded quarter-wavelength SIRs," *IEICE Electronics Express*, 2019. (Under Review)

[5] **Pin Wen**, Zhewang Ma, Haiwen Liu, Shuangshuang Zhu, and Masataka Ohira, "Balanced-to-unbalanced filtering power dividers (BTU FPD) using parallel coupled-line with variable bandwidth and high-selectivity," *IEEE Access*, 2019. (Submitted)

Conference Papers:

[6] **Pin Wen**, Zhewang Ma, Haiwen Liu, Masataka Ohira, Baoping Ren, and Xiaolong Wang, "Compact dual-band bandpass filter using stub-loaded stepped impedance resonators with mixed electric and magnetic couplings," *2017 Asia Pacific Microwave Conference (APMC)*, Kuala Lumpur, Malaysia, pp. 803-805, Nov. 2017.

[7] **Pin Wen**, Zhewang Ma, Masataka Ohira, Xiaolong Wang, Haiwen Liu, Baoping Ren, and Xuehui Guan, "Differential dual-band filter with flexible frequency ratio using H-shaped composite resonator for SCDMA and LTE applications," *2017 IEEE Electrical Design of Advanced Packaging and Systems Symposium (EDAPS)*,

Haining, Hangzhou, China, pp. 1-3, Dec. 2017.

[8] **Pin Wen**, Zhewang Ma, Haiwen Liu, Shuangshuang Zhu, Masataka Ohira, Chuanyun Wang, Xuehui Guan, and Baoping Ren, "Novel compact dual-band BPF using stub-loaded shorted stepped-impedance resonators," *2018 Asia Pacific Microwave Conference (APMC)*, Kyoto, Japan, pp. 22-24, Nov. 2018.

[9] **Pin Wen**, Zhewang Ma, Shuangshuang Zhu, Haiwen Liu, Baoping Ren, and Masataka Ohira, "Balanced-to-unbalanced filtering power divider with stub-loaded dual-mode resonators," *2019 International Symposium on Antennas and Propagation (ISAP)*, Xi'an, China, Oct. 2019. (Accepted)